Experimental and Numerical Studies for Synchrotron-based X-ray Fluorescence Imaging in Medium Sized Objects

Dissertation
zur Erlangung des Doktorgrades
an der Fakultät für Mathematik, Informatik und Naturwissenschaften
Fachbereich Physik
der Universität Hamburg

vorgelegt von

Oliver Schmutzler

Hamburg

2020

Gutachter der Dissertation:	Prof. Dr. Florian Grüner Prof. Dr. Wolfgang Hillert
Zusammensetzung der Prüfungskommission:	Prof. Dr. Günter Hans Walter Sigl Prof. Dr. Florian Grüner Prof. Dr. Wolfgang Hillert Prof. Dr. Wolfgang Parak Dr. Elisabetta Gargioni
Vorsitzender der Prüfungskommission:	Prof. Dr. Günter Hans Walter Sigl
Datum der Disputation:	23.11.2020
Vorsitzender Fach-Promotionsausschusses PHYSIK:	Prof. Dr. Günter Hans Walter Sigl
Leiter des Fachbereichs PHYSIK:	Prof. Dr. Wolfgang Hansen
Dekan der Fakultät MIN:	Prof. Dr. Heinrich Graener

Contents

Abstract

The increasing interest in nano materials, nano medicine and general applications of nano particles in biological systems demands imaging and analysis methods which meet the requirements of small concentrations and smallest scales without applying destructive force. Synchrotron-based X-ray fluorescence imaging (XFI) is a promising modality for such applications. This work describes hurdles and opportunities of mono energetic pencil beam synchrotron-radiation-based XFI in theory and experiment, probing various tracers in medium sized targets. With numerical studies the parameter space of incident beam energy, tracer element and phantom size was explored for best fluorescence yield. $K_{\alpha 1}$, $K_{\beta 1}$ and $L_{\alpha 1}$ fluorescence yield calculations of 1µg tracers in spherical water phantoms with radii of 1 mm and 10 mm irradiated with mono energetic photons from 10 to 100 keV are shown for all stable elements, relevant background phenomena are also displayed. Potential background by scattered polarized photons is studied spatially and spectrally with GEANT4 simulations for water phantoms with radii of 1 mm to 50 mm covering energies from 5 to 110 keV. Experimental studies on medically an biologically relevant probes were performed at the PETRAIII synchrotron. Low energy gold L-shell fluorescence was used experimentally to determine sub pg cellular uptake of PSMAi+ and MUA functionalized gold nano particles in PC3 cells with smallest irradiated sample sizes of 622 and 311 cells. Medium energy gadolinium K-shell fluorescence was applied to image gadolinium based MRI contrast agent Gadovist residuals in a rat bone. Here the XFI quality of beam size dependent spacial resolution was demonstrated with pixel size of 1x1 mm^2, 0.2x0.2 mm^2 and 0.1x0.1 mm^2, allowing for area scans with locally increased spatial resolution. Highly localized gadolinium concentrations of over 500µg/g(bone) thereby were found. A multi modal approach of heavy element K-shell fluorescence, using platinum, iridium, gold and bismuth, imaging of all four elements simultaneously was demonstrated and compared to sensitivities of single element imaging. Only high concentrations yielded significant sensitivity losses compared to single element usage, therefore multi mode XFI is as viable as single element tracer usage if moderate concentrations are expected.

Zusammenfassung

Mit steigender Bedeutung von Nanomaterialien, vermehrtem Interesse an Nanoteilchen für medizinische Anwendungen und der generellen Interaktion vom Nanoteilchen und biologischen Systemen, sind Analyse- und Bildgebungsmodalitäten notewendig, die kleinste Konzentrationen auf kleinsten Skalen auflösen können ohne das fragliche Objekt zu zerstören. Die Röntgenfluoreszenzanalyse ist ein vielversprechender Kandidat für diese Anforderungen. In dieser Arbeit wurden Herausforderungen und Chancen von synchrotron gestützer Röntgenfluoreszenzbildgebung an Objekten mittlerer Größe dargelegt. Analysen zur Fluoreszenzausbeute in Abhgängigkeit von Bestrahlungsenergie, verwendetem Markierungselement und Phantomgrößen von 1 und 10 mm Radius mit Berücksichtigung von Signaluntergrund durch Compton Streuung oder detektor Effekten wurden angestellt um optimale Parameter für Röntgenfluoreszenzbildgebung zu eruieren. Zu erwartender Untergrund, durch Streung primärer polarisierter Röntgenstrahlung im Phantom, wurde mit GEANT4 Simulationen von sphärischen Wasserphantomen mit Radien von 1 bis 50 mm sowohl räumlich als auch spektral für Energien von 5 bis 110 keV untersucht. Experimentelle Studien von biologisch und medizinisch relevanten Proben wurden an dem PETRA III synchrotron durchgeführt. Mit niederenergetische Gold L Schalen Fluoreszenz wurde die Aufnahmemenge von PSAMi+ und MUA funktionalisierten Goldnanoteilchen in PC3 Zellen, Prostata Tumor Zellen, untersucht. In Proben von 622 und 311 bestrahlten Zellen konnten Aufnahmemengen von weniger als 1 pg bestimmt werden.
Räumliche Verteilungen des, im MRT Kontrastmittel Gadovist enthaltenen, Gadoliniums konnten mit mittlerer Fluoreszenzenergie von 42 keV in einem Rattenknochen aufgelößt werden. Die durch Strahlgröße skalierbare räumliche Auflösung wurde hier mit Pixelgrößen von 1x1 mm^2, 0.2x0.2 mm^2 and 0.1x0.1 mm^2 demonstriert und ermöglichte trotz großflächigem Scan die Detektion von kleinsten lokalen Einschlüssen mit konzentratioen von über 500µg/g(Knochen). Simultane multimodale hochenergetische K Schalen Röntgenfluoreszenz mit den Elementen Iridium, Platin, Gold und Bismuth wurde demonstiert und zeigte im Vergleich mit Einzelelementbildgebung nur wenig Sensitivitätsverlust. Simultane

multimodale Anwendungen von Röntgenfluoreszenzbildgebung erscheinen daher sinnvoll, sofern betrachtete Spurrenelemente in geringer Konzentration in der Probe vorliegen. Experimentelle Arbeiten am Synchrotron mit einem Schwerpunkt auf biologischen und medizinischen Fragestellungen dienten zur Demonstartion der vielseitigen Anwendbarkeit von Röntgenflureszenz Bildgebung im Kontext mit zellulärer Nanoteilchenaufnahme und der Bildgebung von Residuen schwerer Elemente in Organismen.

Zusammenfassung

In dieser Arbeit wurden die Herausforderungen und die Chancen von Röntgen Fluoreszenz Bildgebung an kleinen Objekten in mm und cm Dimensionen mit Synchrotronnadelstrahlen dargelegt. Abschätzungen zur Fluoreszenzausbeute in Abhgängigkeit von Bestrahlungsenergie, verwendetem Markierungselement und Phantomgröße von 1 und 10 mm mit Berücksichtigung von möglichem Signaluntergrund durch Compton Streuung oder detektorintrinsischen Effkten wurden angestellt um optimale Parameter für Röntgen Fluoreszenz Bildgebung zu eruieren.
Zu erwartender Untergrund, durch Streung primärer polarisierter Röntgenstrahlen im Phantom, wurde mit GEANT4 Simulationen von sphärischen Wasserphantomen mit Radien von 1 bis 50 mm sowohl räumlich als auch spektral für Energien von 5 bis 110 keV untersucht.
Experimentelle Arbeiten am Synchrotron mit einem Schwerpunkt auf biologischen und medizinischen Fragestellungen dienen zur Demonstartion der vielseitigen Anwendbarkeit von Röntgenflureszenz Bildgebung im Kontext mit zellulärer Nanoteilchenaufnahme und Residuen schwerer Elemente in Organismen.
Mit niederenergetische Gold L Schalen Fluoreszenz, angeregt mit 15 keV an der P11 beamline, PETRA III, wurde die Aufnahmemenge von Goldnanoteilchen in Prostata Tumor Zellen untersucht. Hierbei wurden unterschiedliche Funktionalisierungsgrade betrachtet, PSAMi+ und PEG, MUA.
Räumliche Verteilungen des im MRT Kontrastmittel Gadovist enthaltenen Gadoliniums konnten mit mittlerer Fluoreszenzenergie von 42 keV in einem Rattenknochen aufgelößt werden. Hierzu wurde eine Anregungsenergie von 52 keV an der P07 beamline, PETRA III, benutzt. Die durch Strahlgröße skalierbare Auflösung wurde hier mit Pixelgrößen von 1 x 1 mm, 0.25 x 0.25 mm and 0.125 x 0.125 mm demonstriert.
Multimodale simultane hochernergetische K schalen Röntgenfluoreszenz mit den Elementen Iridium, Platin, Gold und Bismuth wurde an der P21 beamline, PETRA III, untersucht.

1 Introduction

The discovery of cathode rays and their applications in the late 19th century gave birth to scientific techniques which grew into essential tools in the following century. One to probe materials on an elementary and quantifiable level, the other to increase the human live span significantly [1]. J.J.Thomson [2] in 1897 first calculated the mass-to-charge ratio (m/q) of free electrons, which then were known as cathode rays, using Crookes tubes [3], electric fields for acceleration and magnetic fields for deflection, thereby founding the area of mass spectroscopy (MS) which is widely used today with the same basic principles to determine m/q ratios of atoms, isotopes and molecules.
The other groundbreaking invention was by Conrad Roentgen in 1895. The first Nobel price in 1901 marked its significance, he discovered the X-rays [4], a new kind of radiation penetrating tissue and opening vistas to the hidden reality of human anatomy. Development of X-ray tubes became a fast growing business, as applications of such high energy rays became numerous. The impact on the health care sector was noticed early, with the theoretical foundations of tomography laid between 1914 and 1940 [5], but for practical applications necessary computational power was lacking.
In 1973, Godfrey Houndsfield published his paper describing a first commercially feasible computed tomography (CT) scan [6], today this technique experiences wide spread use. Applications are diagnostic purposes, planning and monitoring of radiation therapy [7] or even dental cosmetics [8]. CT is mostly limited to structural imaging as X-rays are more likely to be absorbed by high Z materials, e.g. bones compared to soft tissue, although contrast agents enable a certain degree of functional imaging [9][10]. CT today is a mayor pillar of modern medicine, with 100 (Poland) to 271 (USA) CT scans per 1000 inhabitants per year [11].
Other medical imaging modalities emerged in the second half of the 20th century. Nuclear magnetic resonances for distinguishing cancerous from healthy tissue was first proposed in 1971 [12]. First magnetic resonance imaging (MRI) image followed in 1973 [13]. Rapid

growth in interest after 1980 [14] established this modality in modern medicine. Without ionizing radiation but usage of strong magnetic fields, nuclear spins and radio waves, MRI predominantly images distribution of Hydrogen and such offering high contrast in soft tissues, differing in water composition, e.g. adipose and muscular tissue. With contrast agents, proposed as paramagnetic catalysts [15] and demonstrated [16], further distinction between similar tissues became possible. In certain cases functional imaging with MRI, called fMRI, is possible [17] [10]. Here gadolinium based complexes play a major role as contrasts agents [18] which have recently shown harmful effects in long term use [19][20]. MRI scans reach a level of 25(Chile) to 143(Germany) applications per 1000 inhabitants per year [21]. Insights in biological processes e.g. metabolic rates, brain activity or blood flow are not easily accessible with structural imaging. Functional nuclear modalities like positron emission tomography (PET) and single photon emission computed tomography (SPECT) complete the mainly structural modalities mentioned above. Early functional *in vivo* measurements of radionuclides with Geiger counters reach back to the 1930 [22], first automated scanner for radionuclides using scintillators was build in 1950 for thyroid imaging [23]. Ring shaped detectors were developed after 1985 and first hybrids, PET-MRI and PET-CT were presented in the late 1990s [24]. PET utilizes short-lived positron emitters, bound to highly bio-compatible molecules, e.g. 18F-FDG, similar to glucose [25]. Standard nuclides are ^{18}F, ^{11}C, ^{13}N,^{15}O [26][27] with corresponding half lives of 110 min, 20 min, 10 min , 2 min [28] although multiple other are suspect of investigation [29]. Regions of high metabolic rates accumulate these tracers. Via the β^+ decay positrons are emitted, which lose energy due to scattering in a range of a few mm, then annihilate with an electron of surrounding tissue and radiate two 511 keV photons back to back. Simultaneous detection of two 180 ° photons is an almost background free method. Time of flight PETs and PET-CT help to increase spatial resolution. PET is limited spatially by the fundamental initial positron range. Emerging from nuclear decays, initial MeV electrons show mean free paths to first interaction from 0.54 mm, full width half maximum (FWHM), for ^{18}F to 6.14 mm FWHM for ^{82}R [30]. SPECT uses direct gamma emitters. Therefore the desired photon energy can be tuned with the correct choice of tracers. Spacial resolution is worse than PET, as no back to back information is given and only single photons are detected, usually larger than 8 mm, although small animal devices were developed with 1 mm resolution [31]. Today these scanners and scan techniques are widely established [21][11]. Development in these fields today is not touching underlying physics but data acquisition and interpretation [32] with a strong trend towards deep learning with automated pattern recognition in large data sets and block chain [33]. These improvements in medical techniques, increased

hygiene and medicine generally helped to increase human life expectancy to the level of up to 84.2 years today [34][1]. The causes of death shifts as life gets safer and healthier. While cardiovascular diseases still are the main causes of death [35], cancer rises to become a major issue to health industry in aging societies [36][37]. Now 120(Mexico) to 275 (Hungary) per 100.000 people die from cancer every year[38]. The above mentioned medical techniques are the main tools for diagnosing and localizing cancerous tissues today. Therapies involve mostly chemo- or radiation therapy which inevitably damages healthy tissue [39][40]. Targeted, focused and individualized medicine which deal with malignant cells with higher specificity are aiming for cancer treatment without high collateral damage [41][42][43]. This field of nano technology and nano medicine is advancing [44][45], the food and drug administration (FDA) approved 51 nano medicines by 2016 [46]. Still in an early phase, nano medicine and similar techniques to tweak biological processes on smallest scales are on the rise [47]. Herein experiments are conducted in small animals or on an even smaller cellular scale, *in vitro* [48][49][50]. Standardized medical imaging modalities often are overstrained by scales of 1 mm or even fewer. As such methods of chemistry, inductively coupled plasma mass spectrometry (ICP-MS), or similar, are usually used to determine the fate of metabolized drugs or nano particles [51][49][50]. The successors of Thomson provide the adequate methods to examine such probes and have a wide range of applications across multiple disciplines. Elementary compositions of probes often are unique, such that analysis on this level is useful to determine its origin. As such, during the last century innovations from chemistry and physics provided methods to break down matter, organic and inorganic, split it apart and sort the constituents. A sensitive method of such analysis is the MS. Herein with electric and magnetic fields ionized particles are separated spatially by charge per mass ratio. Effective and homogeneous ionization is therefore necessary, which is achievable by various methods. One of the most sensitive modalities is ICP-MS, its principle limits reach down to parts per trillion [52], for gold this is equivalent to 0.001 ng per mL water. Limits are element specific, and depend on the probe preparation as well as on possible instrumental contaminations. Such low resolutions were shown by [53] and surpassed with 0.43 pg per mL (Bi) [54]. Such methods are qualitative and quantitative, but difficulties might arise since the sample needs to be itemized previous to the process. Therefore in vivo imaging or the analysis of high value samples are excluded. Further more does ICP-MS require a minimum sample size, which is in the range of 5 mL[55].

An in principle non-destructive, *in situ*, method is the widely used X-ray fluorescence spec-

troscopy (XRF), although most standardized XRF setups use grained thin layer probes [56][57], as they are less demanding to the data analysis and are nondestructive techniques. Here, limits of detection are in the range of $\mu g g^{-1}$, or ppm [58][59], even though smaller limits of ppb have been demonstrated [60]. X-ray fluorescence was first used for quantitative element analysis in 1928 [61]. Exciting heavy element inner shell electrons, K or L-shell, results in electron relaxation and highly element specific X-ray emission. High Z elements produce hard photons with high transmission capabilities [62]. Up to 100 keV are obtained from heavy element K-shell fluorescence, with the energy of the emitted photon proportional to Z^2. This method is limited to heavier elements, since the X-ray emission of light elements lack transmission capabilities and therefore are only detectable in thin probes. Even air might become a problem below a certain threshold. The fluorescence process is induced by exposing the samples to radiation, mostly photons. If particles, ions or protons, are used, this method is refereed to as particle-induced X-ray fluorescence (PIXE) [63]. Modalities for excitation are X-ray tubes [64], radioactive nuclides [65], polarizing devices for background reduction are sometimes applied[66] [67], and synchrotron radiation (here in plants) [68]. XRF is none destructive, provides an in principle unlimited spacial resolution and, with sufficient active detector area, also *in vivo* measurements might be achievable [69]. The natural abundance of heavy elements in the human body is low, mostly μg per body [70], therefore this method has not been considered for medical use in the last century. Even though there were *in vivo* experimental studies to determine heavy element uptake of workers with XRF using X-ray tubes [71] [72] [73][74] or more recently, *in vivo* in tibia detection of gadolinium based MRI tracer residuals with XRF exited by an radioactive source [75][76]. These approaches yielded low, if any, spacial resolution. Highest spatial resolution on the other hand is obtained by synchrotron based XRF experiments used to image metal distribution in thin layered biological tissues with spatial resolution of a few hundred nm, multi modal applications, quantitative and qualitative measurements and *in situ* imaging [77][78][79]. Nano particles enable injection of artificial high Z elements to organisms which then can be subject of XRF imaging. Particular cancer related research with gold nano particles is here prominent e.g. *ex vivo* imaging of tumor bearing mice[80][81].
With similar setups *in vivo* XFI-CT were performed on mice with gold and gadolinium nano particles by a group which also used iodine and barium previously [82][83]. Such XFI-CT scans usually do not display high spatial resolution.

First scientific description of gold nano particle (NP) synthesis was by Michel Faraday in

1857, where he described a "beautiful ruby fluid" [84]. With the upcoming of nano chemistry in the second half of the 20th century and its rising popularity in the early 2000s [85] and the wide range of possible applications of nano particles, the production of such particles has become a standard procedure. Gold nano particles can be manufactured in different sizes and shapes [86]. Not only are nano particles additives for enhanced material performance [87], but they also can be coated with a multitude of different compounds, including organic molecules [88]. This opened the door to nano medicine, particles small enough to enter cells in high numbers with the capability to carry drugs, proteins or almost any molecule, and interact with the fundamental building blocks of life.
Nano particles therefore have a wide possible range of medical applications. From pharmacokinetics, drug and gene delivery [89] in tumor therapy, and diagnostics, dose enhancement or imaging, the potential medical applications are numerous [90][91][92].
Some studies use the enhanced permeability and retention (EPR) effect to load tumors with nano particles. This effect relies on the tumors leaky vasculature to Enhance the Permeability and Retention of nano particles in malignant tissue [93] [94] [95]. It is questionable how universally the effect can be transfered from rodents to humans and various tumor types [96] [97]. Relying on passive targeting to enhance tumor uptake of nano particles is missing an essential feature of NPs. Functionalization enables direct targeted delivery to the desired tissue and also a possibly enhanced cellular uptake compared to the pure EPR effect [98]. Anyhow, the question of cellular uptake still is depending on many parameters, targeted cell type, surrounding tissue, particle functionalization, coating, size [99] [100]. Quantitative uptake measurements, especially *in vivo*, pose non negligible impediment. ICP-MS, and other destructive methods for material analysis offer highest resolution down to low concentrations.
In vivo chemical analysis can not be applied and standardized medical imaging modalities fail if small scales are of interest. XRF offers an, in principle, unlimited spacial resolution for tracing nano particles on smallest scales to investigate pure NPs or NP-bound drug kinetics and dynamics with high resolution. Compared to PET tracers, NPs can achieve longer blood-half live, e.g. iodine nano particles with a in mouse blood-half live of 40 h [101]. And a wide range of different elements might be used as nano particles, while no short lived radioactive nuclides need to be handled. Therefore XFI is a promising imaging candidate to boost methods of modern medicine.
In which cases XFI might be applied, which techniques are usable and which pitfalls are to be avoided will be examined in this thesis. Therefore geaometry and tracking 4 (GEANT4) [102][103][104] Monte-Carlo simulations and synchrotron based pencil beam experiments

were performed and evaluated. While work coping with human sized applications was done in our group [69], here the focus is dedicated to the smaller objects, ranging from cells to small animal bones.

This work can generally be divided into three parts. The first part includes chapter 2 describing underlying physics which will be encountered in later chapters, and chapter 3 where experimental devices and analysis methods are explained.
The second part describes theoretical and numerical studies on general behavior of medium sized targets irradiated with polarized synchrotron radiation. Chapter 4 gives calculation on best tracer element choice for various incident energies irradiating medium sized phantoms. Here cadmium telluride and silicon detectors are considered. The background which is to be expected during an synchrotron-based experiment is analyzed with GEANT4 simulations in chapter 5.
The third part is the experimental part including chapter 6, a cellular gold nano particle uptake study, chapter 7, which explores the possibilities of high energy multi mode XFI, and chapter 8, where the adaptable spatial resolution was demonstrated in finding heavy metal residuals in a biological object.

2 Theory

2.1 Pencil Beam XFI in a Nutshell

X-ray fluorescence imaging (XFI) is a non destructive method to map and quantify elemental distributions in probes. Samples are scanned, here with an X-ray pencil beam. X-rays then induce fluorescence in the irradiated material. Fluorescence is the isotropic emission of element characteristic light. For X-ray fluorescence heavy elements are chosen such that emitted fluorescence photons are highly energetic hard X-rays. The emitted light from the probe is detected with X-ray detectors. Via statistical analysis it can be estimated whether specific elements are contained in the probe or not. If the incident pencil beam flux and target object is sufficiently known, the elemental abundance can also be quantified. The details and theoretic background is laid out in the following.

2.2 Photon Matter Interaction

XFI uses photons to probe matter. In the first place to induce X-ray fluorescence with photons by target irradiation, and second, in the detection of fluorescence photons. How photons travel through matter, which processes occur and which need to be payed attention to in respect to XFI is discussed in this chapter.

Photons

Whether described as electromagnetic waves [105] or quantized particles [106], main photon properties are energy E, momentum $\boldsymbol{k}$ and polarization $\boldsymbol{\epsilon}$. In vacuum photons move with constant velocity $c_0 \approx 299.79\text{e}6\,\text{m/s}$ and oscillate in the plane of polarization with energy

dependent frequency $f = E/h$ with Planck constant $h = 4.14^{-15}$ eVs. The corresponding wavelength $\lambda = c/f$ is defined by the speed of light. Wavelengths and energies of visible light, 700 to 400 nm and $1.8 - 3.1$ eV, do barely penetrate dense matter [107]. Photons used in this work in general are referred to as X-rays and have energies of 1 to a few 100 keV. Corresponding wavelength here are 1.2^{-9} m for 100 keV X-rays.

Matter

All particles with a rest mass larger 0 are here considered as matter. Relevant properties are mass m and charge q. In standard energy ranges, matter consists of negatively charged electrons, neutral neutrons and positively charged protons. Those particles organize themselves by principles of atomic and nuclear physics to atoms with a core of protons and neutrons with electrons spread around that core [108][109][110]. In total the atom is electrically neutral if not ionized. Around 1860 Mayer and Mendelejew first ordered the elements in periodic structures [111]. Its successor today is known as the periodic table which sorts the elements according to shell structure and nuclear charge number Z. Starting with the lightest element, hydrogen, consisting of one proton, followed by helium, with two protons and two neutrons up to the heavy elements like gold, with Z=79 and further. Stable heavy elements possess more neutrons than protons, while elements with neutron numbers strongly diverging from Z tend to be radioactive and decay to elements in more stable regimes [110]. The electrons are sorted in shells, which are dictated by the Pauli exclusion principle [112] prohibiting two electrons in the same state in one atom [108].

Interaction and Cross Sections

XFI is based on the interaction of photons and matter. Interaction probabilities are key to first: select tracer highly likely to produce desired fluorescence if irradiated and second: to estimate tracer quantity in scanned regions. Interactions of any kind can be quantified by a cross section σ. For I particles hitting the area A with N_T target particles, the number of expected interactions N is approximated by

$$N = I\sigma N_T/A, \tag{2.1}$$

under the assumption of small non intersecting targets. Usually the unit of cross sections is cm^2, but for the purpose of photon matter interaction a more common figure, the mass

attenuation coefficient $(\mu/\rho)[cm^2/g]$ will be used. With the Avogardo number N_a and the mass per mole m_a [g/mol] the cross section can be expressed by

$$\sigma = (\mu/\rho)m_a/N_a. \tag{2.2}$$

The number of events

$$N = I(\mu/\rho)m/A \tag{2.3}$$

is then simply related to the mass m [g] included in the irradiated area A[cm^2] [113]. For the case of high target concentrations or thick targets the approach of non intersection becomes inaccurate. In case of targets with length l a differential approach needs to be followed with an attenuated incident beam N(x) according to the Lambert Beer law 2.10. The number of events then can be estimated by:

$$N = I\ (1 - \exp(-(\mu/\rho)l\rho)\ ) \tag{2.4}$$

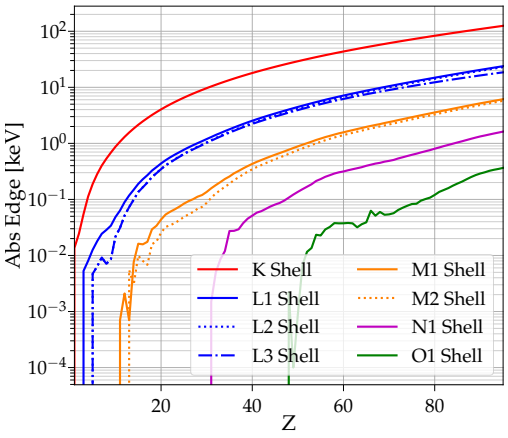

Figure 2.1 – Shell absorption edge energies [keV] for elements from Z=1 to Z=90. Data taken from [114]

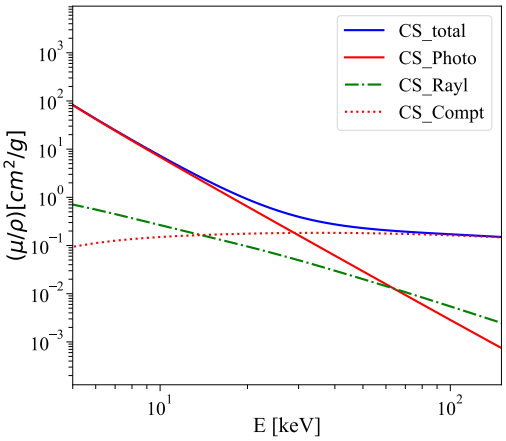

Figure 2.2 – Water interaction cross sections from 5 to 100 keV. Photo absorption dominates lower energies, but decreases similar to Rayleigh cross section at higher energies. Above 30 keV Compton scattering is the main occurring process in water. Data taken from [115].

2.2.1 Photo Absorption

It was found in the late 19th century, that light can be absorbed by metallic materials, inducing electric sparks[116]. It only was absorbed if it exceeded a certain energy and even highest intensity could not excite a spark if this threshold was not met. This phenomenon is caused by the quantized nature of light and discrete electron binding energies. The threshold, the minimum necessary photon energy, for it to be absorbed and a photo electron to be ejected, is named absorption edge and equal to the binding energy of that electron.

As electrons are bound in different shells with differing binding energies, many equivalent corresponding absorption edges exist. The absorption probability and thus the cross section σ_{phot} generally scales with $Z^5 E_\gamma^{-3.5}$ [117]. Additional structure is added to the absorption cross section by the quantized nature of bound electron states. If photon energy E_γ passes a stronger bound electron shell threshold, the photo absorption cross section jumps since now a larger phase space is viable, imposing a saw like shape on σ_{phot}. The process of photo absorption is dominant in water for photon energies up to 30 keV, above that Compton scattering is dominating, as shown in figure 2.2. Water is relevant here as it is the main constituent of soft tissue, photon interaction processes in phantoms or biological targets are therefore expected to be dominated by water cross sections. Element dependent absorption edges in keV are displayed in figure 2.1 on a logarithmic scale. Above Z=10 K-shell ionization requires at least 1 keV increasing to more than 100 keV at Z=90. L-shell edge energies rise similarly but are roughly one magnitude smaller. M- N- and O-shells with decreasing binding potential require less and less energy to be ionized.

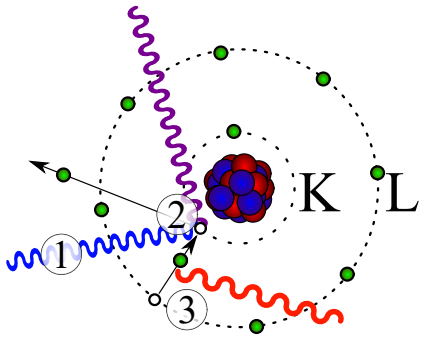

Figure 2.3 – Schematic Sketch of ionizing process via K-shell scattering and subsequent K-shell fluorescence. A high energy incident photon (1) scatters on a K-shell electron (2), thereby ejecting it and leaving a vacancy. Here scattered light is of less energy than primary light. The vacancy is filled by an L-shell electron (3), emitting fluorescence light.

2.2.2 Ionized States

Electron number per atom is equal to the atomic number Z in neutral states. While outer shell electrons are bound with only a few eV energy as they are shielded from the whole nuclear charge. With decreasing mean distance r to the nucleus, Coulomb potential Φ_C increases and shielding effects decrease [107]. Innermost electrons experience the full Coulomb potential of the whole nuclear charge Z with the Vacuum permittivity ϵ_0

$$\Phi_C = Z_{eff}/(4\pi\epsilon_0|r|). \tag{2.5}$$

The effective Z_{eff} per electron configuration differs per element, such that each electron is bound by different energies. If sufficient energy is transferred to a bound electron, the binding potential can be overcome and the electron is ejected from the atom, leaving a vacancy in its former shell. The atom now is ionized, this process is illustrated in figure 2.3.

Empty states of high binding potential are filled by electrons from less strongly bound states. During this transition, the energy differences between final and initial state, $\Delta E = E_i - E_f$, of the jumping electron is released. E_i and E_f are element specific, as described above, individual binding energies can be found in the X-ray Data Booklet [113][118]. An electron transitioning from i to f leaves a secondary hole in its former state. Ionizing an inner shell therefore is not a singular event, but triggers long cascades of radiative and non radiative electron transitions through all shells of an atom. Most of these events show low ΔE rendering them irrelevant for X-ray modalities. Different processes are defined, depending on the way how ΔE is released. Radiating processes are called Fluorescence.

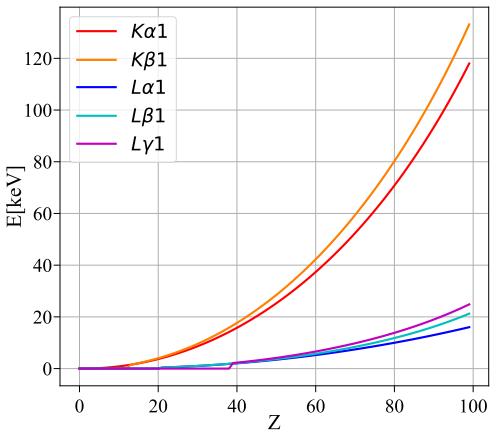

Figure 2.4 – Fluorescence line energy of most intense lines and highest energies depending on Z. Data from [114].

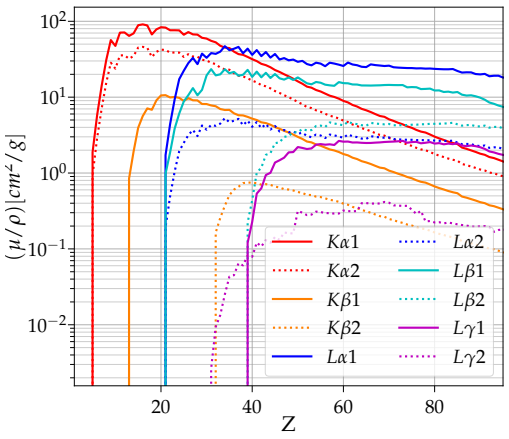

Figure 2.5 – Maximal cross sections, at the edge, of the major fluorescence lines for different elements. Data from [114].

2.2.3 Fluorescence

Energy release by photon emission is called fluorescence. Outer shell fluorescence events, with binding energies of eV emit visible light, with wavelength of a few 100 nm, X-rays are produces if $\Delta E > 0.1\,\text{keV}$ with wavelength of a few nm. The multitude of different electron states in heavy elements imply the existence of many different fluorescence lines, although only a few remain dominant. Either because the cross sections of most transitions are vanishingly small, as depicted in figure 2.5, or the fluorescence energies are low and experience major attenuation and scattering in surrounding media. Transitions of highest energies are displayed in figure 2.4. Common notation for labeling fluorescence lines was introduced by Siegbahn [119], this will be used in the following.
As shown in figure 2.4 the photon energy scales with $(Z-1)^2$ as described by Moseley [120]. This is true for all shells, but the innermost K-shell produces highest energies up to 80 keV if radioactive elements are excluded. However K-shell transition cross sections dominate only in the light element regime with maximum values of up to 90 $[\text{cm}^2/\text{g}]$ (Z=16), followed by an exponential decay with increasing Z, down to 3 $[\text{cm}^2/\text{g}]$ for Z=80. Here the L-shell is a factor of 7-8 more efficient, see figure 2.5 and 2.6. With increasing energy and further distance to the absorption edge, cross sections for all shells decline, shown in figure 2.6 for gold. Figure 2.7 displays the cross sections of $L_{\alpha 1}$ and $K_{\alpha 1}$ lines normalized to

its maximum values against the energy above the relevant absorption edge. High energy fluorescence cross sections are more robust to changes in incident energy.

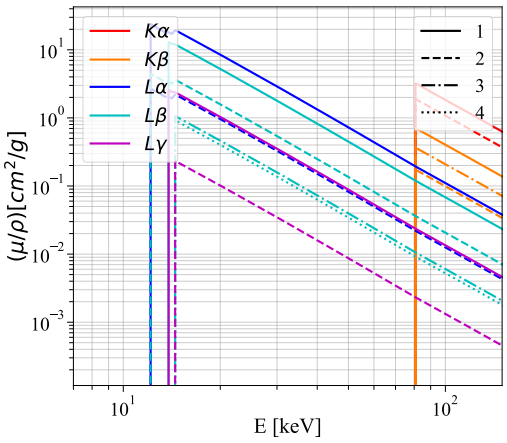

Figure 2.6 – Cross sections of the major fluorescence lines for the case of gold, Z=79. Data taken from [114].

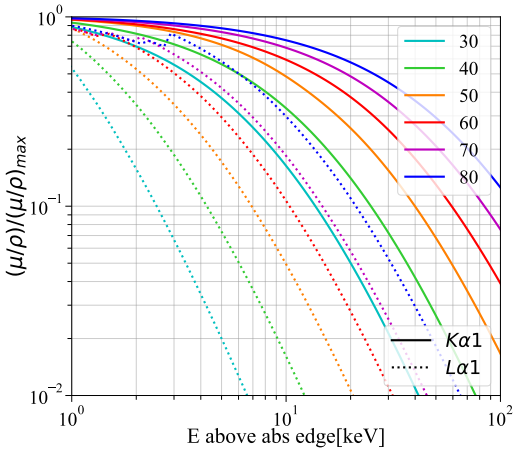

Figure 2.7 – Relative fluorescence cross section decay to its maximum for elements of Z=30, 40, 50, 60, 70 and 80. Data taken from [114].

2.2.4 Auger Effect

Non radiative transitions occur with intra hull energy transition, this is called the Auger effect. The otherwise as photon released energy is transitioned to another electron, leading to its emission from the atom [121]. Auger cascades release therefore many free electrons in irradiated material. The Auger process is dominating for lower Z elements generally. K-shell auger and fluorescence yield is compared in figure 2.8. Above Z=30 fluorescence yield increases and converges to one for high Z elements.

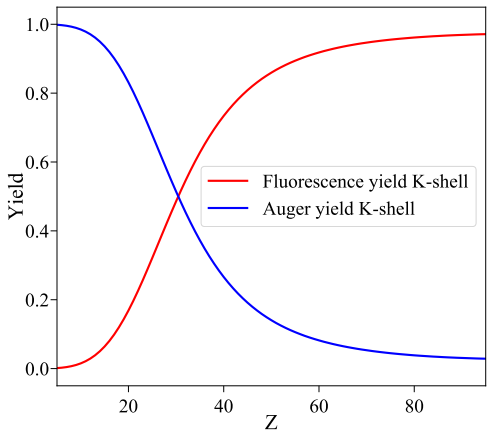

Figure 2.8 – K-shells Auger and fluorescence yield. Data taken from [114].

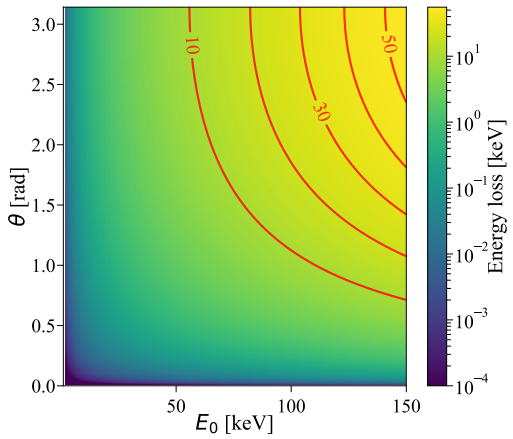

Figure 2.9 – Photon energy loss per scatter angle. Data taken from [114].

2.2.5 Photon Scattering

Besides absorption processes photons also can be scattered. Such scattering of photons can be divided into two categories, elastic scatter events with preservation of photon energy but change in momentum and events with change in energy and momentum, here refereed to as inelastic scattering. The latter process is also called Compton scattering [122], elastic scattering here is Rayleigh scattering [123]. Elastic scattering is of minor importance for this work, but is mentioned here as Rayleigh peaks will be visible in many spectra.

Compton Scattering

Events which cause photons to lose energy and change direction are a major challenge to the XFI method for two reasons. First: former fluorescence photons which underwent Compton scattering can not easily be associated with the fluorescence process and therefore are lost as signal photons. Second: initial photons above the fluorescence region, and therefore intrinsically not considered as background, scatter in air or surrounding material and such contribute to background in the signal region significantly. This is strongly depending on object size, material and photon energy used. Collimation techniques might reduce such Compton background to a valuable extent, although even the best collimation includes a signal reduction [69]. The scattering process for unpolarized photons is characterized by

the primary photon energy E_0 and the polar scatter angle θ. The change in photon energy is described by

$$E = \frac{E_0}{1 + E_0/(m_e c^2)(1 - \cos\theta)}. \tag{2.6}$$

This can be derived via momentum and energy conservation under the premise of an resting initial electron. The energy loss of scattered photons is shown for relevant energies in figure 2.9 for single scattering. Maximum loss occurs under 180° scattering. For calculating maximum energy loss under N scatter events, 2.6 can be reformulated to:

$$E_N = \left[\frac{1}{E_0} + N\frac{2}{m_e c^2}\right]^{-1} \tag{2.7}$$

Angular scatter probabilities are approximated by the Klein-Nishina formula which ignores electron momentum [124],

$$\frac{d\sigma}{d\Omega} = 0.5 r_e^2 \frac{E^2}{E_0^2}\left(\frac{E}{E_0} + \frac{E_0}{E} - \sin^2(\theta)\right) \tag{2.8}$$

here the scale of the process is determined by the classical electron radius $r_e \approx 2.82\,\text{fm}$ [125]. For small photon energies Compton scattering diverges from the Klein-Nishina formula since initial electron momentum and thus Doppler broadening is not taken into account here [126].

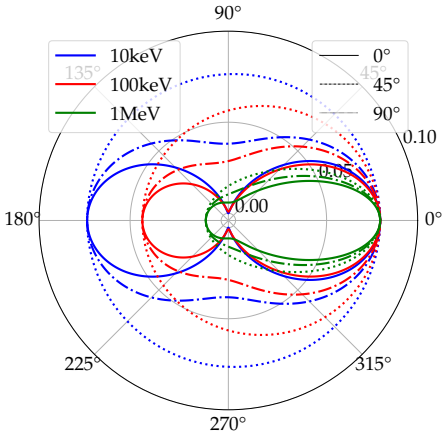

Figure 2.10 – Klein Nishina cross sections for 10, 100 and 1000 keV polarized photons. While for 0° the plain of scattering lies in the polarization plane, 90° scattering occurs perpendicular to the polarization. The case of 45° equals unpolarized light. Data from [114].

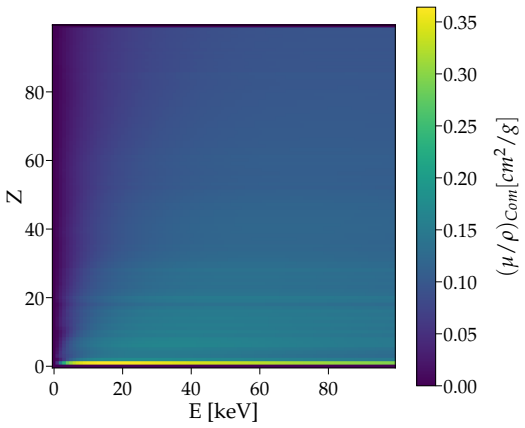

Figure 2.11 – Element dependent Compton scatter cross sections. Low energies and high Z provide smallest, hydrogen generally the highest Compton cross section. Data from [114].

Polarization does not change the absolute probability of scattering, but weights the spacial orientation since the event now has a preferred direction. The azimuth angle ϕ described by the plane of polarization and the scatter plane is included as a weighting factor:

$$\frac{d\sigma}{d\Omega} = 0.5 r_e^2 \frac{E^2}{E_0^2} \left(\frac{E}{E_0} + \frac{E_0}{E} - 2\sin^2(\theta)\cos(\phi)^2 \right), \tag{2.9}$$

which now favors scattering perpendicular to the polarization plane of the photon [127].

Rayleigh Scattering

Scatter events without energy loss are called Rayleigh scattering [123]. Since no energy loss occurs the process is generally not strictly relevant for XFI as it does not contribute to background in the signal region. Nevertheless will it be a prominent feature in simulations and experiments. The high Z depending nature of Rayleigh cross sections should be emphasized here, which Compton scattering does not display. This might cause Rayleigh peaks in simulations to deviate from experimental results when examined probe composition is not known precisely. Rayleigh scattering cross sections exceeds Compton cross sections at

low energies, e.g. in water as shown in figure 2.2, but decreases at energies above 20 keV with λ^{-4}.

2.2.6 Lambert beer

Photons traversing matter experience attenuation due scatter and absorption processes as stated above. The probability of interaction for a single photon is described by the energy dependent attenuation coefficient (μ/ρ) given in [cm^2/g], tabulated in the NIST database [115]. With the material density ρ and the length l to be traversed, the attenuated photon intensity I after traversing is calculated by the Lambert Beer law

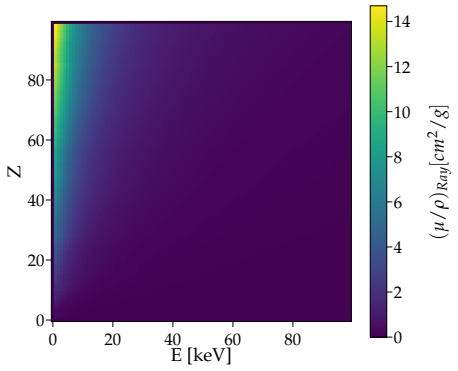

Figure 2.12 – Element dependent Rayleigh scatter cross sections. Low energies display strong gradients from high to low Z elements. Data from [114].

$$I = I_0 exp(-(\mu/\rho)\rho l), \tag{2.10}$$

with the incident photon intensity I_0 [128]. Usually total attenuation coefficients (μ_{tot}/ρ) are of interest, which includes scattering and absorption processes of all kinds, but they also can be chosen for distinct processes. These values show a strong dependency of the photon energy E, and the traversed material, as shown in 2.13. The transmission factors of 1 mm elemental material which are often used for filter or collimation purposes are displayed in 2.14. While light elements mostly do not effect the photo transmission, heavier elements show severe attenuation on medium energies of $20 - 50$ keV and still 1% transmission at 60 to 70 keV. The importance of the sawtooth-shaped photo effect cross section can be seen here easily.

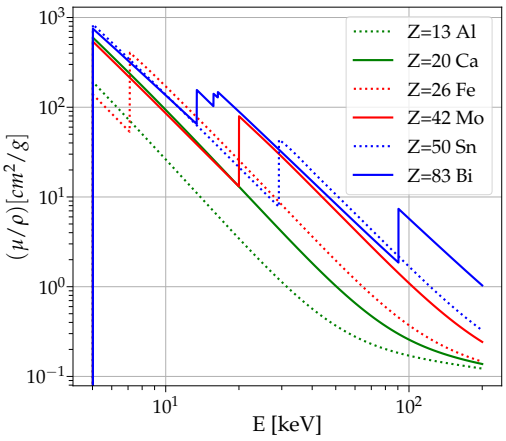

Figure 2.13 – Total attenuation coefficients (μ/ρ) in cm^2/g of metals common for X-ray absorbers or collimators. Data taken from [114].

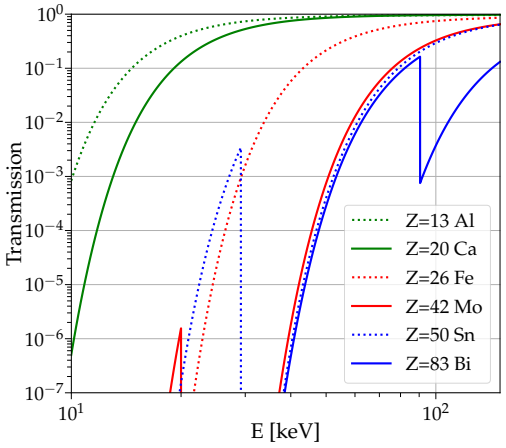

Figure 2.14 – Energy dependent transmission of photons through 1 mm material usually used for filter or collimator applications. Data taken from [114].

2.3 X-ray Sources for XFI

Small, cheap and already in clinical use for decades, X-ray tubes drawbacks for XFI will be laid out below, but special cases and examples are given, why they should not be abandoned too hastily for XFI purposes.

General demands on the X-ray source are first: a high photon flux, as this strongly limits measurement time. Second: a relative small bandwidth $\Delta\Omega$. Relative, because a mono energetic beam is not necessary, still it is demanded that most of the spectrum is above tracers shell edges which should be excited. But not to far, since the absorption cross section declines exponentially. Third: even though some XFI studies use fan[129] or cone beams[130], they do so because a lack of pencil beams. If pencil beam scans are applied to achieve high spacial resolution, as in this thesis, beams with low divergence, at least across the object of interest, are required. And the beam diameter should be scalable from few mm to tens of µm. This of course needs to be adjusted to the object of interest. Fourth: a linear polarized beam helps to reduce Compton background by angular selection. This is optional as target sizes increase since preferred scatter direction is lost after few scatter events. Fifth: the main energy emitted should be tunable to allow for various different Z tracers and target geometries. The energy range in question ranges from 10 keV for small

object to 100 keV or might exceed 100 keV if object size increases [69].
Ideally sources should be small and affordable, easy to maintain and to operate. The author is aware of the fact that these criteria are hardly met all at once. Therefore two common sources, mostly found in the XFI literature, and their characteristics are shortly described here. A common figure of merit for light source comparison is brilliance, photons per 0.1 % bandwidth per second per area per angular divergence $[\mathrm{s\,mrad^2\,0.1\%bw\,mm^2}]^{-1}$. This can also be applied to the XFI sources, even though the bandwidth argument is not key here. If a high brilliance sources is considered, it is important to examine which parameters boost this value.

2.3.1 X-ray Tubes

Basic principle of X-ray tubes is the production of bremsstrahlung by acceleration of charge [107]. Therefore electrons are emitted by a cathode, mostly a tungsten filament, accelerated in a potential and then dumped in a corresponding anode. The kinetic potential gained in acceleration is relieved during deceleration as radiation, the X-rays. The deceleration in the anode is of stochastic nature, the vicinity of nuclei and incident electron determine the degree of deflection and thus the energy of produced radiation. Thereby a broad X-ray spectrum is obtained. If applied potential is surpassing anode absorption edges, characteristic anode material fluorescence lines appear in emitted spectra [131]. The highest X-ray energy here is limited by the applied potential used for acceleration. Many photons are irradiated at lower energy, while high energy photons are comparatively sparse. Low energy attenuation in anode material creates the shape of X-ray tubes spectra[132]. Uncollimated radiation originating from the anode has a wide divergence depending mostly on the anode geometry. This and the broad spectrum make X-ray tubes an unfortunate source for XFI applications. X-ray tubes show brilliances of 10^5 to 10^{10} ph/$(\mathrm{s\,mrad^2\,0.1\%bw\,mm^2})$.
Anyhow still remarkable results were published with benchtop sources [81]. Here tracer elements are matched to anode fluorescence lines, as demonstrated in [133], with a multilayer mirror and liquid-metal-jet micro focus source [134] using indium-alloy (24.2 keV K_α) molybdenum nano particles were exited.

2.3.2 Synchrotrons

Synchrotron radiation is light emitted by accelerated charged particles. This phenomenon was first noticed at a synchrotron facility, hence the name. Synchrotrons store high energy particles, usually electrons, circulating with nearly the speed of light, bent by magnets to the designed orbit. The emitted light, first a residual effect, was discovered in 1947 [135]. With progressing time and increasing interest in X-rays, accelerators were designed mainly with the goal to produce synchrotron radiation. First generation sources included facilities SURF at the national institute of standards and technology (NIST),Frascatti Laboratory (Rome), INS-SOR (Tokyo) and deutsche elektronen-synchrotron (DESY) (Hamburg) and many more [136]. In the 1980s the second generation synchrotrons founded tasks still of interest today as protein crystallography, and shifted the viable light from infrared to X-rays. The third generation around 1990 started to introduce undulators and wigglers to the storage rings [137]. These are straight sections of periodically alternating magnetic fields by arrays of magnets forcing passing electrons on a sinusoidal path. These straight insertion devices produce radiation magnitudes more intense compared to radiation emerging from bending magnets. Those are the high intense hard X-ray sources today at modern synchrotrons [138]. Synchrotron radiation from bending magnets has a continuous spectrum with critical energy $E_c = (3\gamma^2 eB\hbar)/(2m_e)$ peaking at $3\,E_c$ with the electron Lorentz factor $\gamma = \sqrt{1-(v/c)}^{-1}$, reduced Planck constant $\hbar$, electron charge and mass e and m_e and the magnetic field B. The radiation opening angle is $\theta \approx \gamma^{-1}$. The Lorentz factor crucially determines synchrotron radiation characteristics. Today electrons in such light sources gain γ values of a few 1000. PETRA III accelerates electrons to 6 GeV, corresponding to roughly γ=12000. Undulators allow for interference of produced synchrotron radiation and therefore offers higher intensities and spectra with multiple distinct peaks, the harmonics. The emitted on axis wavelength of the nth harmonic can be estimated with $\lambda = \lambda_u/(2n\gamma^2)(1 + K^2/2)$ [139]. With the undulator period λ_u, the smallest distance in the undulator between two places of same polarity and the undulator parameter $K = eB\lambda_u/2\pi m_e c$ which usually exceeds 1 for wigglers and is below 1 in the undulator case.

Monochromators are used at beamlines to select single harmonics and thus offer quasi monochromatic high intensity tunable beams. Attenuators and collimators than shape beam profile and total flux to the desired values.

PETRA III exceeds brilliances of 10^{21} ph/(s mrad^2 0.1%bw mm^2) at 5 to 10 keV photon energy then decays to 10^{18} to 10^{19} at 100 keV [140][141]. A spectral resolution below 0.01%

can be obtained, e.g. the P07 beamline reaches 7e-5 with channel cut[142].

2.4 Detectors

Spectral detection of X-rays from 1 to 150 keV is here performed with semiconductor detectors. Standard materials are silicon for lower energies and Ge, cadmium telluride (CdTe), cadmium zinc telluride (CdZnTe), gallium arsenide (GaAs) for higher energies, chips of a few 100 µm are widely used [143].
If energy E is deposited in the chip, electrons, negatively charged, and holes, positively charged, are created in number proportional to E. Materials with larger band gaps require more energy to lift electrons from the valence band to the conduction band and such create less free charge carriers per energy deposition than materials with small band gaps. Free charges are driven by the electric field in the depletion zone to opposing electrodes and thereby are detected as current. Some phenomena limit the efficiency of detection or add features to recorded spectra which namely are: whole tailing and escape peaks in CdTe chips [144][145][146] and incomplete charge deposition, limited quantum efficiency and limited resolution generally [143]. For light element detectors or high energy radiation quantum efficiency is an issue. Chips turn transparent if photon energies are comparable high, see figure 2.14. The other features will be discussed below in more detail. In total theses features dictate the detector response function and thus the peak shape, but also impose a non negligible background in wide ranges below prominent peaks. Sharp monoenergetic peaks create step like features, while broad spectra superpose lower energies with a smooth diffuse background with no distinct features.
This is important for two reasons: first, to access the true number of fluorescence photons in peak structures. Second to estimate background level in energy regions which should not be reached by sheer Compton scattering in the phantom object.

Resolution

Assuming underlying Gaussian broadening processes, monoenergetic peaks are detected as Gaussian with mean μ, width σ which is equivalent to the root mean square (RMS). Full width half maximum values can be calculated with FWHM $\approx 2.3548\,\sigma$. Principal limits to RMS are set by the Fano factor, a material dependent ratio of the electron hole pair

production variance over the electron hole pair yield [147]. This RMS limit F_{lim} can be estimated by the energy required to create an electron hole pair in the semi conductor E_h and the Fano factor F.

$$F_{lim} = \sqrt{F E_h E[keV]}. \tag{2.11}$$

Fano factors F are slightly energy dependent, as shown in [148] for Si. None the less, the change is minor therefore a constant factor can be assumed for the simulations without loss of predictability. Fano factors used are: F= 0.115 for silicon and 0.1 for CdTe [148][149]. The energy required to create one electron hole pair E_h is not equal to the corresponding band gap for indirect semi conductors, where additional phonon excitation is required, is 3.6 eV in Si and 4.43 eV in CdTe. Usually energy resolution is dominated by other factors, depending on gain and chip quality and electrical noise. As such additionally to the Fano factor a simple fitted constant is added to the noise such that RMS = $F_{lim} + C_{fit}$, as in [69].

Partial Events - Electron Escape

Interaction close to chip surface might lead to partial escapes of the induced electron charge cloud. Also Auger electrons might leave the chip. These events occur especially for low energy X-ray detection as they only show low chip penetration capabilities. Close to surface interaction then is more probable. Such electron escape events manifest in a low energy plateau reaching from the peak to zero [150][151].

Photon Escape

Photons leaving the detector chip partly or totally undetected can be distinguished in primary and secondary photons. Partial incomplete detection might occur if primary photons scatter in the chip and leave without further interaction, the remaining Compton electron then will be detected. Such events create plateaus in the detected spectrum from 0 keV to a maximum energy equal to the maximum energy loss in a single Compton scatter event, compare figure 2.9. This is dependent on the initial photon energy and scatter angle, therefore no sharp cut offs are expected as mostly no singular lines are detected, but wide spectra. As shown in figure 2.9, photons of 80 keV create a plateau by such scatter events up to 20 keV, while 60 keV the plateau reaches 11.41 keV.

Secondary photons are chip material fluorescence induced by primary radiation which escapes the chip. Such features are known as escape peaks located below the primary energy $E - E_{DF}$, with the detector fluorescence energy E_{DF}. Especially heavy element chips display this behavior since they are more prone to fluorescence, as shown in figure 2.8.

Hole Tailing

This effect is prominent in compound semiconductor detectors and caused by low in chip charge mobility causing reduced charge collection efficiency [146][152]. If planar detectors with uniform electric filed are regarded, the chips charge collection efficiency can be described by the Hecht equation:

$$CCE = \frac{Q}{Q_0} = \left[\frac{\lambda_h}{L}\left(1 - e^{-x/\lambda_h}\right) + \frac{\lambda_e}{L}\left(1 - e^{-\frac{L-x}{\lambda_e}}\right)\right], \tag{2.12}$$

with the distance x into the chip where energy deposition occurs, the total chip thickness L and mean charge drift length $\lambda_c = \mu_c \tau_c E$. Which is a product of charge mobility μ_c, lifetime τ_c and electric field E. In CdTe $\tau_h \mu_h$ is typically a magnitude smaller than the electron equivalent $\tau_e \mu_e$ [144][152]. Values for the XR-100-CdTe detector are: $\lambda_h = 0.8\,\text{cm}$ and $\lambda_e = 13.2\,\text{cm}$ [153]. If energy depositions occur close to the surface located cathode, holds only travel small distances. Higher incident photon energies lead to further chip penetration which causes the hole path to increase in length. Therefore charge loss due to loss in hole current becomes significant if the incident photon penetrates large parts of the chip prior to absorption. Hole tailing manifests itself in CdTe detectors therefore when irradiated with photons above 50 keV. Peaks then shape a tail towards lower energies with a cutoff at a certain percentage of mean peak energy. This percentage is described by Amptek to be 95 %, but practical applications [69] and this work showed it to be less at 90 %.

2.5 Data Processing and Statistics

Detectors sort detected photons in bins, usually 4096, according to their energy. The bin width Δ_E varies, depending on how the gain is set in the detector configuration files.

Detected signals with an amplitude S ideally follow a Gaussian distribution

$$f(x) = S \exp\left(-\frac{(x-\mu)^2}{2\sigma^2}\right) \tag{2.13}$$

at the mean μ with its RMS σ mainly determined by detector effects. Sorted in bins, the counts per Gaussian is $G_C = S\sqrt{(2\pi)}\sigma/\Delta_E$.
The processes described above usually contribute to a certain background which needs to be distinguished from the signal. Detectability of a signal with height S can be quantified by how much it raises above the noise of background fluctuations. With Poissonian statistics

$$P_\mu s(k) = \frac{\mu^k}{k!} e^{-k}\,, \tag{2.14}$$

the variance σ^2 is given by μ, therefore the probability values fluctuate with $\sqrt{\mu}$ around the expectation value μ. To estimate whether a peak with height S on a homogeneous background, with the background height $B = \mu$, is a signal or background fluctuation, the signal to noise ratio

$$SNR = S/\sqrt{B} \tag{2.15}$$

can be accessed. A signal to noise ratio (SNR) of three or higher usually is regarded as a detectable signal [154], although this is disputable [155]. As the background often is not a flat plateau but consists of a slope with additional background peaks, the background height B over the signal range is difficult to estimate. Further more does the SNR value scale with the chosen bin width Δ_E and is incoherent for different kinds of data presentation (Δ_E). Furthermore, the SNR level of 3 is debatable and not easily quantifiable. As such a similar method to estimate the probability of signals raising by chance uses p-values and significances σ. Here not the height of background and signal is relevant, but the counts in the signal S_C peak and the counts in the according background B_C region.

2.5.1 Hypothesis Testing and Statistical Significances

A single sided hypothesis test is performed for each signal which states a probability that a signal like feature rises by chance out of a background (null hypothesis) H_0. Which always should be: there is no signal present and the spectrum consist only of photons driven by background processes. Key now is the calculation of signal counts S_C and background counts B_C in the range where a signal is expected. For a highly sensitive analysis only detailed fitting, accounting for various background processes and using reasonable fit

functions, will produce correct results. Misinterpreting the spectrum and assuming a false background function, is similar to supposing the wrong null hypothesis H_0.
For the case, S_C and B_C were determined correctly and H_0 is true, the assumption is that C_S is merely a statistical fluctuation of the background. The p-value quantifies the probability of such an event or even stronger fluctuations with

$$p = \sum_{n \geq C_S + C_B}^{\infty} \frac{(C_B)^n}{n!} \mathrm{e}^{-C_B}, \tag{2.16}$$

if the underlying distribution is of Poissonian nature. P values tend to become small fast. For easier handling, such values are transformed to significance Z in standard deviations σ of the normal distribution, which is 1.

$$Z = \Phi^{-1}(1 - p) \tag{2.17}$$

With the integrated standard distribution

$$\Phi(x) = \int_{-\infty}^{x} \frac{\exp(-z^2/2)dz}{\sqrt{(2\pi)}}. \tag{2.18}$$

If enough counts are acquired, 2.16 can be calculated using Gaussian distributions without loss of accuracy. Z then is equal to $C_S/\sqrt{C_B}$. The here relevant hypothesis test are single sided, in this case a significance of 5 corresponds to a p value of $2.867e^{-5}$ %, this is the applied significance level in particle physics marking a discovery. Here a less strict level of $Z = 3$ is used to mark a detectable signal, with $p = 0.135$ % and such allow a false positive for 1 in a thousand.

3 Methods

During experiments methods and practices are often recurring as well as later data analysis techniques, experimental setups, detectors in use and frequented PETRA III beamlines. Therefore a short overview concerning these methods is given here. Conducted experiments generally can be described as synchrotron based pencil beam X-ray fluorescence imaging. As synchrotron beams are fixed, targets are moved through the beam to enable 2D scanning.

3.1 Beamlines at PETRA III Synchrotron

The positron-elektron-tandem-ring-anlage III (PETRA III) synchrotron at DESY(Hamburg, Germany) offers 22 experimental end stations for wide range of different purposes. At three of these beamlines experiments were conducted, these are the P11 beamline, P07 and the P21 beamline.

P11 - Bio - Imaging and Diffraction Beamline

The P11-bio-imaging and diffraction beamline at PETRA III [156][157] is generally dedicated to structural resolution of small scale biological samples. For parts of this thesis the crystallography P11 endstation was used. It offers X-rays between 5.5 and 30 keV. Instead of available nano focus, pin beams were applied, shaped to desired profiles with pin holes. Uncollimated flux on target at 12 keV is $1.3\,x\,10^{13}$ph/s [157]. Photons are polarized horizontally. Targets were mounted an the single axis goniostat with horizontal spindle. The beamline owned Hitachi Vortex-EM [158], see 3.3.1 for further description, was used during the P11 experiment. This beamline is not suited for heavy element K-shell analysis. Nevertheless heavy element L-shell or light element K-shell still is a viable option for smaller targets.

P07 High Energy Materials Science Beamline - Experimental Hutch 2

The P07 [142] experimental hutch 2 is the DESY administrated part of the HEMS beamline. It is dedicated to general high energy applications and offers tunable energies from 50 to 200 keV of horizontally polarized photons with a maximum flux on probe of 7×10^{11}ph/s at 100 keV. Spot sizes can be varied between 1×1 mm^2 and 2×30 µm^2.
A HUBER diffractometer designed for a load of up to 200 kg, as in [159], can be used to set up highly individualized end stations. For example the one described in 3.2. Flux reduction can be achieved by inserting iron absorber into the beam with units of 3 mm thickness.

P21.1 Beamline

Similar to the P07 this beamline provides high energy linear horizontally polarized photons. Available energies are 52, 85 and 100 keV with a maximum flux on probe of $2\,x\,10^{11}$ph/s with a 1×1 mm^2 spot size which can be decreased with slits. As the P07 a heavy load HUBER diffractometer is available to mount experimental setups [160].

3.2 Experimental Stage

Experiments require well known setups otherwise they suffer from lack of reproducibility and results will deviate from simulations. Therefore an alignment of the whole experiment to the X-ray source as well as good aligned components of the experiment towards each other are key. The components usually are the target itself, one or multiple detectors and eventually collimators. To ensure this and enable quickly installed experimental setups on HUBER diffractometers present at P07 and P21.1 experimental hutches.

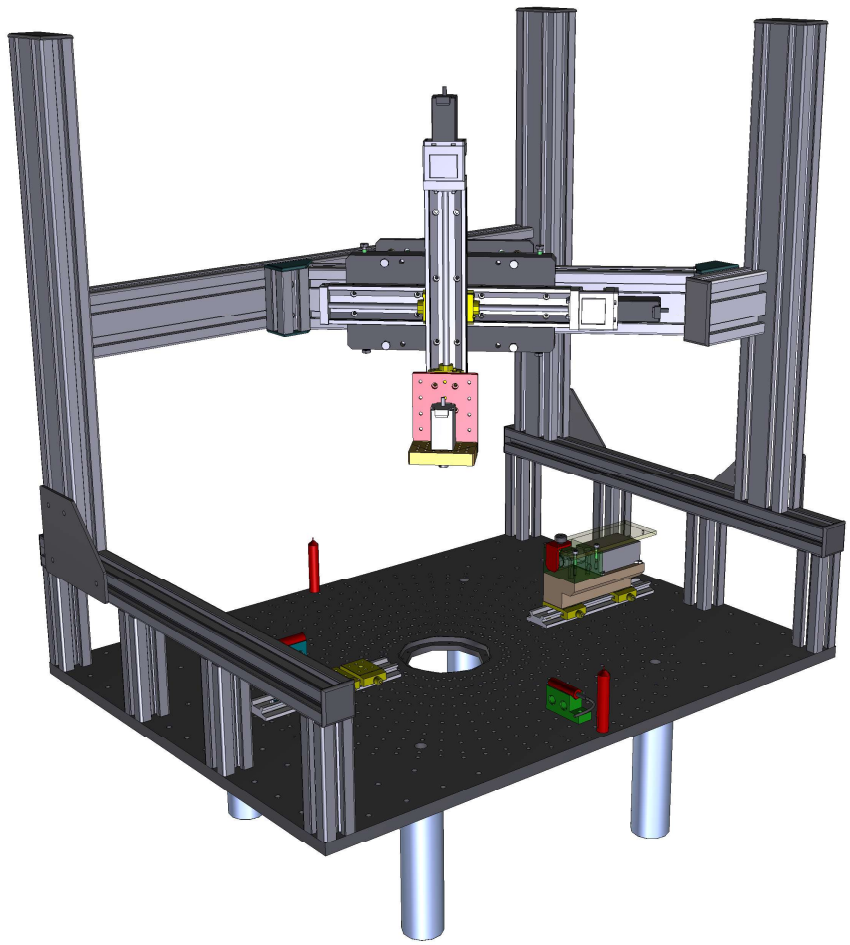

Figure 3.1 – Experimental stage designed for synchrotron based XFI experiments with two axis probe translation ability. Radially extending threaded holes allow for detector placement under various angles in 5° steps. Here shown is an Amptek detector with housing. Detectors are mounted on rails to allow for precise radial movement.

The stage build for this purpose consists of an aluminum base plate, 1.5 cm thick with a $80 \times 90\,cm^2$ area, a 10 cm diameter hole in its center ensures vertical mobility for probes needing a long traverse path in this direction. With a stainless steel inlet the center hole can be closed. Radially from the center extend multiple M6 threaded drill holes in 5 ° steps. Here detectors and collimators can be mounted with high precision. If distance between parts need flexibility, rails can be used to preserve angular orientations during radial movement. Such movement could in principle be motorized and now is. With four aluminum pillars the plate is mounted on the HUBER stage.
The X-ray pin beam should cross 8 cm above the aluminum plate and split it in halve such that scattering on target occurs symmetrically into both sides. Detector windows are horizontally aligned to the beam. For target scanning purposes, movement through the beam needs to be provided while detectors and stage stay fixed. Two 30 cm Misumi linear axes, cross mounted on Rose-Krieger-Profiles, enables such scanning. Usually this plane is chosen perpendicular to the beam, covering the y (vertical) and x (horizontal) axis. With adjustments of the Rose-Krieger-Profiles the plane of motion can be moved to achieve an angle of 45 ° to the incident photon beam. Such a setup can be utilized if long probes need to be scanned horizontally and detectors need to be placed in 90°.

3.2.1 Stage Adjustment

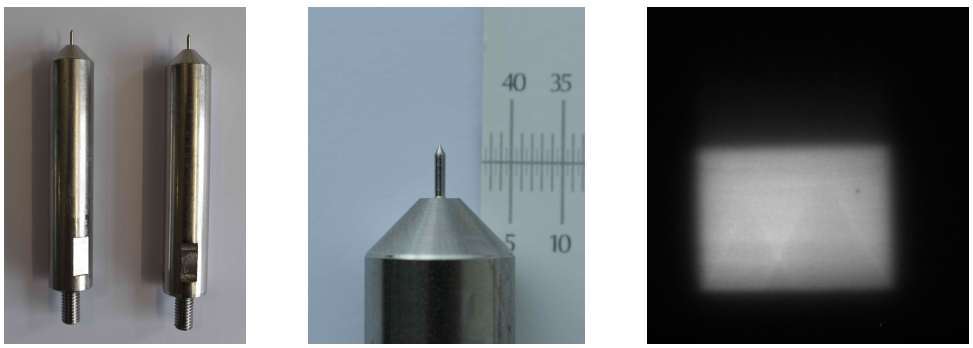

Figure 3.2 – Beam needles for stage alignment. Left: the two needles. Center: Conical tip of one needle. Right: Forward X-ray camera, tip shadows should overlap completely indicating correct aligned stage. Here two distinct shapes are visible.

The HUBER Diffractometer, present at the beamlines P07 and P21.1 allows for x,y and z translation and phi (± 180 °) and theta (± 5 °) rotation. After mounting the stage on it, it is adjusted such that the X-ray beam is parallel to the main experimental plate and

8 cm above it. To ensure an angular offset close to zero, two beam needles, positioned at center front and center back of the stage, can be used as means of setting the stage in correct position. Their tip height is 8 cm above the aluminum plate. These needles are shown in figure 3.2. A forward X-ray camera is necessary to monitor their shadows, here in use is the X-ray eye [161]. The stage is positioned such that both needles interject the beam path at same height. If misaligned the forward camera displays two distinct needle tips. A horizontal offset needs to be corrected by rotation, a vertical one by tilting. Two completely overlapping shadows indicate good alignment, compare figure 3.2 (right).

3.3 Detectors

Three different detectors were used of which the Amptek XR-100T-CdTe and the 70 mm^2 FAST SDD are owned by our group, while the Hitachi Vortex-EM was available at the P11 beamline.

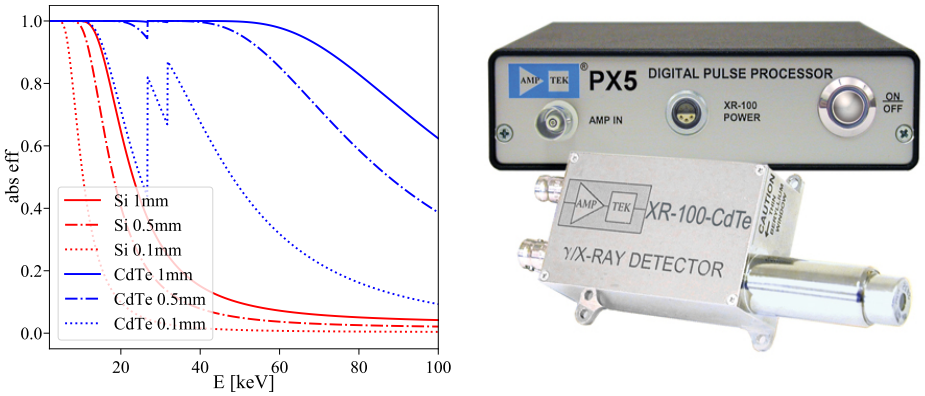

Figure 3.3 – Left: Quantum efficiencies of different detector chips thicknesses. Silicon and Cadmium telluride are compared for chip thicknesses of 1, 0.5 and 0.1 mm. Right: Image of the Amptek CR-100T-CdTe detector with external digital pulse processor unit, picture taken from [153].

3.3.1 Hitachi Vortex-EM

The Hitachi Vortex-EM [158], 50 mm^2, 0.5 mm thickness detector was used only during experiments at the P11 beamline. The Si chip reaches energy resolutions of 138 to 180 eV

(FWHM) at 5.9 keV. Since the absorption curve of Si decreases drastically above 20 keV, its use is limited to light element K-Shell analysis or heavy element L-Shell XFI.

3.3.2 Amptek XR-100T-CdTe

The Amptek XR-100T-CdTe [153] is an high energy X-ray detector providing an rectangular $5x5x1\,mm^3$ CdTe chip shielded with 100 µm Be window. This model is shown in figure 3.3 with the external digital pulse processing unit. The 1 mm thickness offers highest quantum efficiencies for heavy element fluorescence imaging. During operation the chip is cooled by a thermo electrical cooling element. The detector is powered by the external PX5-box which also performs pulse processing. Amptek claims RMS values of 225.1 eV at 14.4 keV and 361 eV at 122 keV, determined with a ^{57}Co source. These values might deviate depending on specific detector settings. Cadmium telluride is more prone to escape peaks due to its high Z values, 48 (Cd) and 53 (Te), compared to 14 (Si). Photo effect is more likely to occur, as described in section 2.2.1 which reliefs its energy with higher probability to fluorescence, compare Auger and fluorescence yields in fig 2.8. As such photo escapes events, as described in section 2.4 need to be taken into account. Relevant fluorescence lines are listed in the tables below.

Cd Line	eV	rel Int
$K_{\alpha 1}$	23173.6	100
$K_{\alpha 2}$	22984.1	53
$K_{\beta 1}$	26095.5	17

Figure 3.4 – Cd fluorescence lines and relative intensities. Data taken from X-ray Data Booklet [113]

Te Line	eV	rel Int
$K_{\alpha 1}$	27472.3	100
$K_{\alpha 2}$	27201.7	54
$K_{\beta 1}$	30995.7	18

Figure 3.5 – Te fluorescence lines and relative intensities. Data taken from X-ray Data Booklet [113]

3.4 Histograms, Fits and Data Analysis

Histograms are the main method of presenting measured and simulated spectral data. Herein background needs to be separated from XFI signals via fits.

3.4.1 Fit Functions and Background

Statistical analysis and fits are generally performed using the ROOT framework. For fitting the minimum χ^2 method from this framework is applied.

Peak Signals

Peaks need to be fitted differently as different behaviors emerge depending on photon energy and detector in use. Simplest shape approach is the Gaussian function:

$$P_0(x) = \mathrm{A}\exp\left(-\frac{(x-E_p)^2}{2(\sigma)^2}\right) \tag{3.1}$$

with the peak height A, its RMS σ and mean energy E_p. This peak shape is generally visible if Si detectors are used, energies are relatively low, up to 35 keV, or peak intensities are minor such that small features vanish in noise. Then this function can be used.
If medium energies and a CdTe detector is used, small hole tailing effects are noticeable leading to an asymmetric peak with tailing towards lower energies. This can be modeled with an additional exponential function which terminates at the peak energy E_p due to an error function:

$$P_1(x) = A\left[exp\left(-\frac{(x-E_p)^2}{2\sigma^2}\right) + erfc\left(\frac{x-E_p}{\sqrt{2}\sigma} + \frac{\sigma}{\sqrt{2}\beta}\right)exp\left(\frac{x-E_p}{\beta}\right)\right]. \tag{3.2}$$

Here one additional parameter β is needed, which is found by fitting experimental data. High energy peaks can only sensibly be detected with a CdTe chip. All hole tailing features need to be taken into account here. The Hypermet function can be applied to fit such peaks, they show a shoulder additional to the low energy tail. Hypermet functions are not consistently defined but the function as defined in [69] can be applied for the case of high energy intense peaks detected with CdTe. The noise term which can be found in [69] is neglected here.

$$P_2(x) = G(x) + D(x) + H(x) \tag{3.3}$$

$$G(x) = A\exp\left(-\frac{(x-E_p)^2}{2(\sigma)^2}\right) \tag{3.4}$$

$$D(x) = A_B\exp\left(\frac{x-E_p}{\beta}\right)\frac{1}{2}\mathrm{erfc}\left(\frac{x-E_p}{\sqrt{2}\sigma} + \frac{\sigma}{\sqrt{2}\beta}\right) \tag{3.5}$$

$$H(x) = A_H\left[1+\mathrm{erf}\left(\frac{x-k_pE_p}{k_w}\right)\right]\frac{1}{2}\mathrm{erfc}\left(\frac{x-E_p}{\sqrt{2}\sigma}\right) \tag{3.6}$$

With the underlying Gauss peak G(x), an exponential tail D(x), and an additional box shaped plateau H(x) with height A_H. Parameters k_w and k_p should be determined by fitting experimental data.
A fluorescence spectrum consists of multiple peaks per element. The relative peak intensity a_p is well known and can be found in the X-ray Data Booklet [113]. Therefore a probe with k_{max} elements and p_{max} lines is described by

$$F(x) = \sum_{k=0}^{k_{max}} I_k \left(\sum_{p=1}^{p_{max}} a_p P_i(x) \right), \tag{3.7}$$

with the absolute elemental intensities I_k and i, determining which kind of peak function is used.

Background Fit

The background fits do highly depend on the scenario. Generally polynomials of 4th to 6th degree can be used for background modeling. If the relevant energy range is on the slope of a peak or higher Compton scatter orders, an exponential added to the polynomial yields good results. Of course, special effects as background fluorescence peaks of surrounding materials, escape peaks or similar detector intrinsic behavior needs to be taken into account. Since this approach is more specific, background functions will be shown in the experimental discussion.

3.4.2 Histogram Preparation

Scaling Experimental Data

Depending on its purpose, experimental data should be corrected differently. First: significance determination should be performed with raw data. Or if scaled data are used, the significance should be calculated with $Z = Z_S/\sqrt{a}$ with the scaling factor a and Z_S the significance determined with scaled data. If fits are applied to calculate the number of photons, the integrated area needs to be divided by the bin width ΔE. It is generally useful to scale data per bin width. Second: for comparative reasons: experimental setups need to be compared even though they differ in substantial setup properties like the number of incident photons, detectors in use, time of measurement, different absorber numbers or materials.

To compare setups mostly independent from the detectors and beamline properties, the essential question is: how many fluorescence photons and background photons per incident photon under a certain angle can be expected. This can be approximated by correcting the histograms by most experimental setup properties. Which are: measurement time t, incident flux F_0, absorber transmission T_a, detector dead time τ, detector chip efficiency e_D, detector solid angle Ω_D (for larger asymmetric phantoms or large area detectors, this parameter might cause categorical problems) and bin width ΔE. Solid angle corrections are more easily applied, if active detector chip area A_A and chip distance to beam D_C is accounted for. The scaling factor then is calculated:

$$a = \frac{D_C^2}{tF_0A_AT_ae_D\Delta_E(1-\tau)}. \tag{3.8}$$

Solid angle corrections should not be used for extrapolations from small solid angles to 4π, as background is not isotropic especially not for polarized photons. As such the correction for Ω_D always needs to be considered as a local variable which loses predictive value the farther the deviation from an experimental setup is.

3.5 Photon Flux Estimation and Mass Reconstruction

The photon flux on target is a key factor in XFI. Not only limits it detectable tracer amount but also renders detectors unusable if exposed to a flux too high. A well known flux is necessary as reconstructed tracer masses are direct proportional to it and uncertainties in flux will directly translate in tracer mass uncertainty.

3.5.1 Photon Flux I_0

Synchrotron beamlines operate unattenuated at a photon flux in the order of 1e10 to 1e13 ph/s. Flux measurements usually are performed with a highly attenuated beam, 3 to 5 magnitudes, then corrected for applied absorbers [162]. This becomes problematic if attenuation coefficients of absorber materials are not as expected, e.g. if absorbers do

not consist of pure iron, as assumed or absorber thickness is not as precise as expected. Even small misalignments of absorber units can have strong impact on flux measurements performed this way.
The flux therefore should be measured how it is used, attenuated if needed, not if the unattenuated beam is used. Devices for measuring photon fluxes at 1e8 to 1e13 ph/s in an energy range from 10 to 120 keV are calorimeters, ionization chambers or pin diodes as listed in [162]. The power of the X-ray beam is mostly to small to be measured with high accuracy via calorimetry, ionization chambers usually require much space and pin diodes good calibration.

A reverse application of fluorescence can be applied to estimate the flux, equations from section 2.2 are used. This method is simple and similar to other experiments performed during this thesis. A defined sputtered layer of elemental gold or similar materials in thickness of a few nm, here 20 ± 2 nm Au on a 1 mm thick Si substrate was used. The flux I_0 then can be estimated to the sputter target precision:

$$I_0 = \frac{N_F 4\pi A_b}{\Omega m t T (1-\tau) D_{eff}} (\mu/\rho)_F^{-1}, \tag{3.9}$$

with the number N_F of detected fluorescence photons of line F, the detector covered solid angle Ω, detector efficiency D_{eff}, the beam area A_b the tracer mass m contained in target emitting fluorescence line F, and the cross section $(\mu/\rho)_F$ for this line at beam energy. Dead time τ, measurement time t, and absorber transmission T, correction need to be applied here to estimate the true count rate.
The attenuation factor T is calculated for the attenuation of the primary beam and the excited fluorescence photons, shown in figure 3.6, as follows:

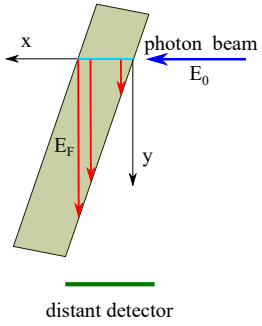

Figure 3.6 – Incident photon beam with energy E_0 excites fluorescence with E_F along the beam path through the target (x-direction cyan color). Fluorescence in detector direction experiences different attenuation in the target as different path lengths in y-direction need to be overcome (red arrows).

$$T = \left(\frac{\mu}{\rho}\right)_F \rho \int_0^L \exp\left(-\left(\frac{\mu}{\rho}\right)_{tot}(E_0)\,\rho x\right) \exp\left(-\left(\frac{\mu}{\rho}\right)_{tot}(E_F)\,\rho\, y(x)\right) dx. \tag{3.10}$$

The intersection of target and beam is of length L, the total absorption coefficients for the incident energy E_0 and the fluorescence energy E_F are used to calculate the transmission

factors in material with density ρ. The path length in the target material which needs to be traversed by a fluorescence photon is $y(x)$, with place of fluorescence origin x, compare figure 3.6.
Equation 3.10 follows from the differential approach of production and transmission of fluorescence and incident beam in a thicker target.

3.5.2 Tracer Mass Reconstruction

The on target photon flux is necessary to estimate the applied dose, which might be medically relevant. If this is not an issue, since dead or otherwise dose irrelevant targets are examined, the hassle of determining experiment setup parameters in equation 3.9 can be skipped. This also excludes potential sources of errors. Detector target distance and thereby Ω and A_b often are kept constant during an experiment. In this case the tracer mass m can be deduced from a reference measurement with equation 3.9:

$$m = m_{REF}\frac{\mathrm{F}}{\mathrm{F_{REF}}}\frac{(1-\tau_{REF})}{(1-\tau)}\frac{T_{REF}}{T_{in}}.\frac{t_{REF}}{t}, \tag{3.11}$$

for detected fluorescence counts F, transmission factors T concerning incident beam attenuation, measurement time t and dead time τ. "REF" variables are referring to the reference measurement. Uncertainties for t and T_{in} are assumed to be negligible and incident photon flux to be constant. This leaves the reconstructed mass uncertainty Δ_m mainly dominated by reference target precision and fit accuracy.

$$\Delta_m = \left[(\Delta_{m_{REF}}\frac{m}{m_{REF}})^2 + (\Delta_F\frac{m}{F_{Au}})^2 + (\Delta_{F_{REF}}\frac{-m}{F_{REF}})^2\right]^{1/2} \tag{3.12}$$

Without a reference measurement, the flux needs to be known. Then formula 3.9 can be applied to tracer mass m and tracer cross section (μ/ρ) with known I_0 to determine the tracer mass irradiated by I_0.

3.5.3 Limits and Extrapolations

Assuming the significance scales linearly with signal photons T_S and with the inverse square root of the background photons T_B, to account for parameter variability in measurement

time t and phantom depending transmission T, the significance Z can be corrected with the following relation:

$$Z = m\sqrt{f_0\, t\, T_{rans}(1-\tau)}\frac{\sigma_{Sig}\, T_S}{\sqrt{\sigma_B T_B}}E_{Det} = m\sqrt{f_0\, t\, T_{rans}(1-\tau)}A. \tag{3.13}$$

If experimental conditions are constant over measurement time t, significance only depends on the tracer mass m. Otherwise changes in the incident photon flux f_0, transmission filters, T_{rans}, dead time τ and detector other effects E_{Det} as well as changes in target shape or cross sections for signal and background photon creation, σ_{Sig} and σ_B, which are summed up in A, influence Z. A fundamentally describes how sensitive an experimental setup is. Therefore to compare XFI experiments, plots of Z/m over $\sqrt{t_{eff}} = \sqrt{f_0 t T_{rams}(1-\tau)}$ are useful.

$$\frac{Z}{m} = A\sqrt{t_{eff}} \tag{3.14}$$

The general detection limit for experiments with a similar setup can be estimated with 3.14.

3.6 Geant4 Simulation

Experiments are the fundamental basis on which physics is performed. But today enough knowledge of fundamental processes in the realm of particle physics is collected over wide range of energies and for all kinds of particles and interaction forces. With a combination of analytical calculations and tabulated values, the GEANT4 toolkit [102][103][104] enables its user to simulate particle matter interaction from few eV to TeV energies based on Monte Carlo methods. It is used for simulating medical applications, neutrino experiments or the design of the latest large scale particle experiment. Similar to the nature of underlying processes, GEANT4 uses random values to calculate interaction probabilities, hence the name "Monte Carlo tool".
Simulations of XFI use photon energies from a few keV to 500 keV, the physics model "low energy electromagnetic physics - Polarized Livermore" was used for photon matter interaction which covers physics from 250 eV to 100 GeV. Line broadening due to charge transport losses are not considered in the GEANT4 simulations. Therefore detected photon energies are distributed according to a Gaussian with experimental determined RMS values and simulated mean energy.

Estimated Detector Resolution in GEANT4

RMS values always depend on detector settings as well as chip condition. Radiation damage for example might worsen the detector resolution significantly. As such only rough estimates of the RMS values for the detectors in use are sensible. To estimate RMS values for the CdTe detector described in 3.3.2, this formula derived from the information given by Amptek and 2.4 will be used: $\sigma(E[eV]) = \sqrt{0.443\,eV\,E[eV]} + 132.1\,eV$. The Si detectors RMS values in **??** are estimated with $\sigma(E[eV]) = \sqrt{0.414\,eV\,E[eV]} + 10\,eV$.

4 Fluorescence Yield Estimations with Consideration of Background Effects

Planing experiments, knowledge of ideal or best possible parameters is required for succeeding. In XFI the question of accessible fluorescence yield is key. Therefore this figure is explored in the following taking all stable elements into account, allowing for cadmium telluride or silicon detectors and for incident beam energies of up to 100 keV.

Estimating the in object fluorescence yield F, simple approaches are promising to calculate correct magnitudes of fluorescence photons expected in an experiment. Despite the following harsh simplifications, these calculations are useful. Simplifications are: the phantom object is a water sphere ($\rho_{H2O} = 1\,\mathrm{g/cm^3}$) with radius r, irradiated with a mono energetic photon pencil beam with radius $r_b = 0.5\,\mathrm{mm}$. Centered in the phantom, tracer material is assumed to be spread in a sphere with beam radius. To obtain comparable numbers between different elements the amount of fluorescence tracer is set to 1 µg, maintaining constant density but varying particle numbers across the elements. The incident X-ray beam with energy E_0 irradiating the whole tracer sphere triggers fluorescence events. Per incident photon, F fluorescence photons of the addressed shell with the energy E_F can be detected outside the water ball in 4π. Transmission in and out is assumed to be dictated only by the water spheres radius and not affected by the tracer itself. Transmission factors are calculated with the Lambert Beers law, and fluorescence production is estimated with cross sections (μ_F/ρ), as described in 2.3:

$$F(E_0, Z) = \mathrm{e}^{(-r\mu_{tot}(E_0))}\,\frac{(\mu_F/\rho)1[\mu g]}{\pi r_b^2}\,\mathrm{e}^{(-r\mu_{tot}(E_F))}\,D_{eff}. \tag{4.1}$$

The yield is corrected with D_{eff} for Si and CdTe detector quantum efficiency, each with a chip thickness of 1 mm. The xraylib was used as a tool to obtain cross sections of these processes [114]. Not only the total fluorescence yield of such a setup is of interest, also a

hurdle need to be avoided. Which is the background, shaped mainly by Compton scattering and detector response. In the following, areas in which the particular fluorescence peak is expected to be in Compton regions, are marked. If fluorescence line energy E_F lies below unscattered incident photon energy and above 180° scattered photon incident energy, this condition is marked as Compton one, C1, background. Similar for Compton order two, C2, with the lower boundary being not single 180° scattering but twofold 180° scattering. Here it is disregarded that Compton scattering, more so for polarized beams, is not isotropic. Thus here marked regions are problematic, if the total solid angle is used.

In practice detector placement and angular selection always makes it possible to avoid a sharp C1 peak in the fluorescence region. Whereas higher Compton scatter orders increasingly become diffuse and thereby can not simply be evaded by angular selection. Anyhow, since C1 events can occur along the hole intersection between phantom and beam, angular selection becomes less effective to avoid C1 as the range for Compton angles grows with phantom size. Such effects are neither simply estimated nor easily graphically presented. Therefore these effects are ignored here for reasons of simplicity. The approach of using minimum and maximum energy loss per scatter event without additional information was taken. Further in depth background analysis will be shown in later chapters using GEANT4 simulations. Additional to Compton scattering detector escape events can not be neglected. This is especially true for CdTe detectors. The major fluorescence transitions were evaluated. $L_{\alpha 1}$, $K_{\alpha 1}$ and $K_{\beta 1}$ were chosen covering a wide energy range, while $K_{\alpha 2}$ and $L_{\alpha 2}$ can be estimated with the corresponding $K_{\alpha 1}$ or $L_{\alpha 1}$ line.

4.1 L-shell - $L_{\alpha 1}$ Line

The $L_{\alpha 1}$ lines are minor in energy, limiting their use to very small objects. Even for Z = 100, the $L_{\alpha 1}$ line energy does not reach 20 keV as shown in figure 2.4. An advantage over other shells lies in the comparable high cross sections, see figure 2.5 and favorable background behavior. Compton scattering at low energies is not effective enough to bridge the gap between necessary incident energy at the L edge and the $L_{\alpha 1}$ fluorescence energy which would be required to contribute significantly to Compton background in the fluorescence region. Energy loss per scatter event is shown 2.9.

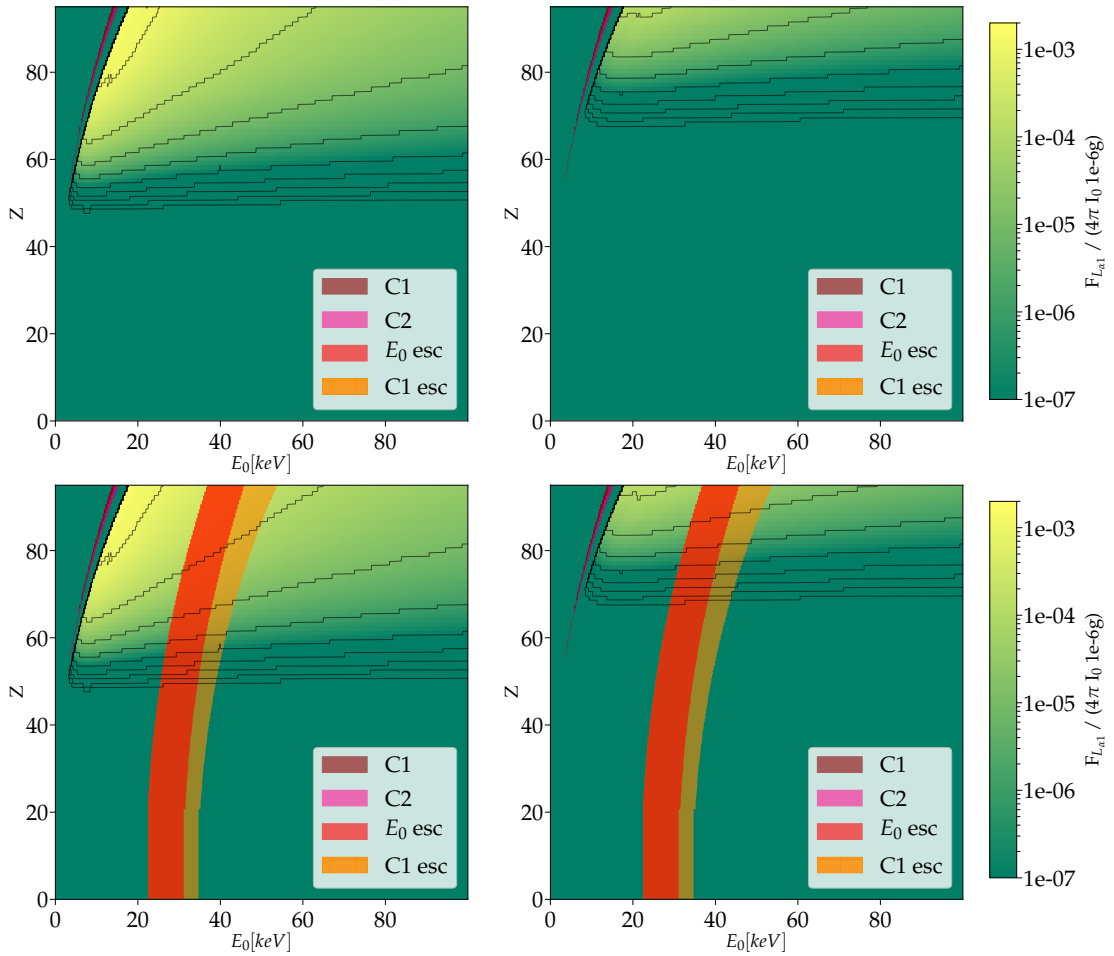

Figure 4.1 – Effective $L_{\alpha 1}$ 4π fluorescence yield in a 0.1 cm (left) and 1 cm (right) radius water sphere depending on the incident energy E_0 and the $1e-6$ g tracer chosen with elementary number Z. Upper calculations assume a silicon detector, lower a CdTe detector. For each a 1 mm chip was assumed. Silicon shows no relevant escape effects, while in CdTe some I_0 - Z combinations are prone to background due to escape events in the fluorescence region. Highest yield are generally obtained closest to the absorbtion edge. In 0.1 cm phantom 1e-3 fluorescence photons per incident photon are detectable, while Z=80 yields three magnitudes less for the 1 cm phantom.

As such in the L regime, Compton scattering is no source of direct background. A further advantage of L regime is the possible use of a silicon detector with mostly full efficiency, compare figure 3.3. With 1e-6 g tracer, yields are shown in figure 4.1. Maximum fluorescence obtained in the smallest phantom, 1 mm radius, is above 1e-3 per incident photon. But only for tracer elements with Z≥78. Optimal incident energy E_0 is found close to the corresponding edge. With decreasing Z the total yield is reduced to 1e-4 for Z=65 and further to 1e-5 at Z=60. Then it drops drastically over 6 magnitudes from Z=60 to Z=50.

While it is most important to chose E_0 close to the absorption edge, to obtain the highest yields, lower Zs are less punishing in the choice of E_0. But already at phantom size of 1 cm radius, yields at Z=80 are roughly 1e-6 fluorescence photons, rendering this shell mostly useless for objects of this size or larger. If instead of a silicon detector CdTe is used for $L_{\alpha 1}$ shells, additional escape regions have to be obeyed. However, they exclude a region where operation should be rejected because of low yield anyway.

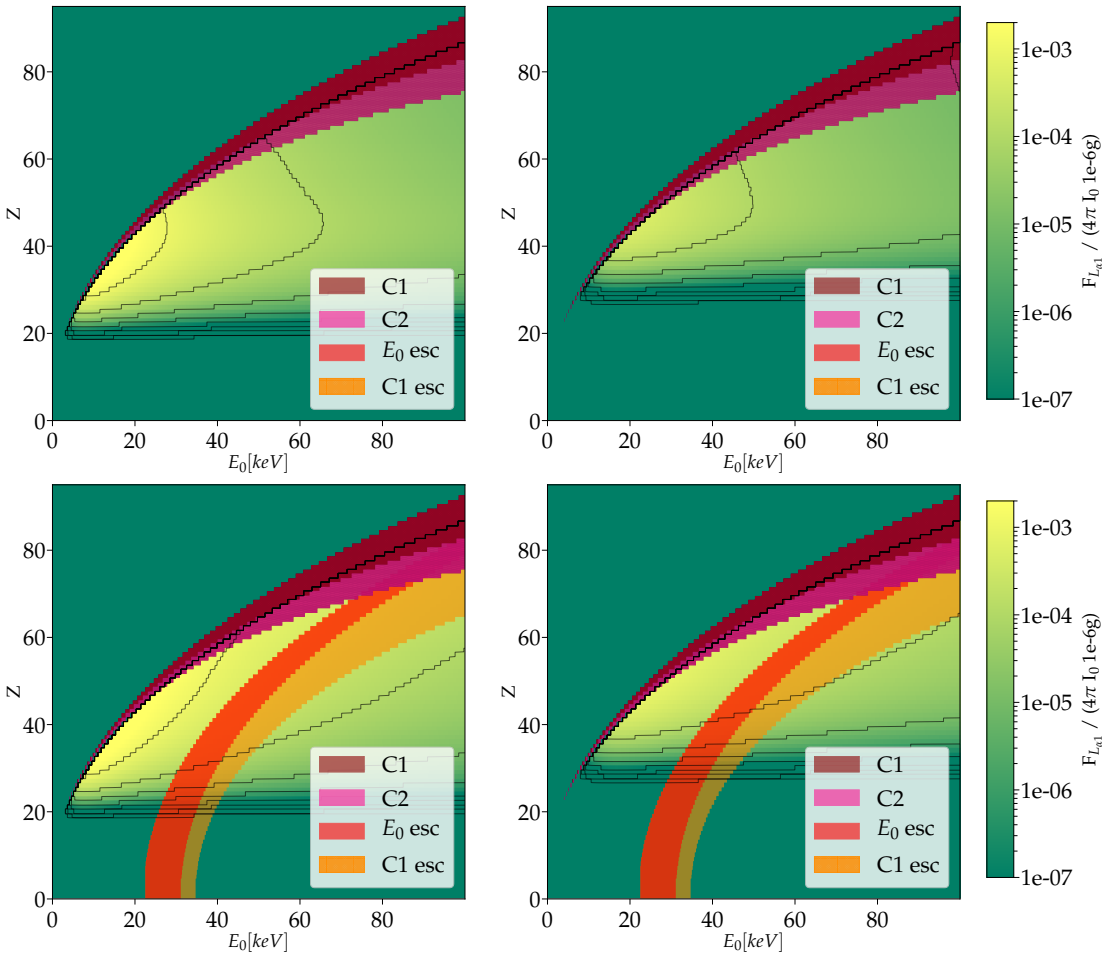

Figure 4.2 – Effective $K_{\alpha 1}$ 4π fluorescence yield in a 0.1 cm (left) and 1 cm (right) radius water sphere depending on the incident energy E_0 and the 1e-6 g tracer chosen with elementary number Z. Upper calculations assume a silicon detector, lower a CdTe detector, for each a 1 mm chip was assumed. Silicon shows no relevant escape effects, while CdTe some I_0 Z combinations are prone to background due to escape events in the fluorescence region. Highest yields are generally obtained closest to the absorbtion edge. In 0.1 cm phantom 1e-3 fluorescence photons per incident photon are detectable, while Z=40 yields one magnitudes less for the 1 cm phantom.

4.2 K-shell - $K_{\alpha 1}$ Line

Larger objects require K shell use, implying radius $> 1\,\text{cm}$. Now while L shell yields limit the choice of elements to the most heavy ones, K shell fluorescence is far less selective in the choice of Z. Therefore a wide range of possible elements can be chosen without severe yield losses. Comparing again yields in 0.1 cm and 1 cm phantom radii, more than $1e-3$ fluorescence photons can be expected for the smallest phantom, similar to the best case of L shell yields, but at lower Z. Here elements between $Z = 30$ and 50 display the highest yield. The 1 cm phantom reduces the yield by a magnitude and shifts the best suited elements to higher Z of 40 to 60. With the silicon detector again escape effects do not affect background sufficiently and at the here prioritized incident energies E_0 of 15 to 30 keV for the smallest phantom and 20 to 40 keV for the 1 cm phantom, Compton scattering mostly can be neglected. Only high Z elements with energies chosen close to the absorption edge show an overlap of fluorescence energy and Compton background. With the background consisting mainly of C2. Silicon as detector material limits the elements to mid range Z as its quantum efficiency drops drastically with increased fluorescence line energy.

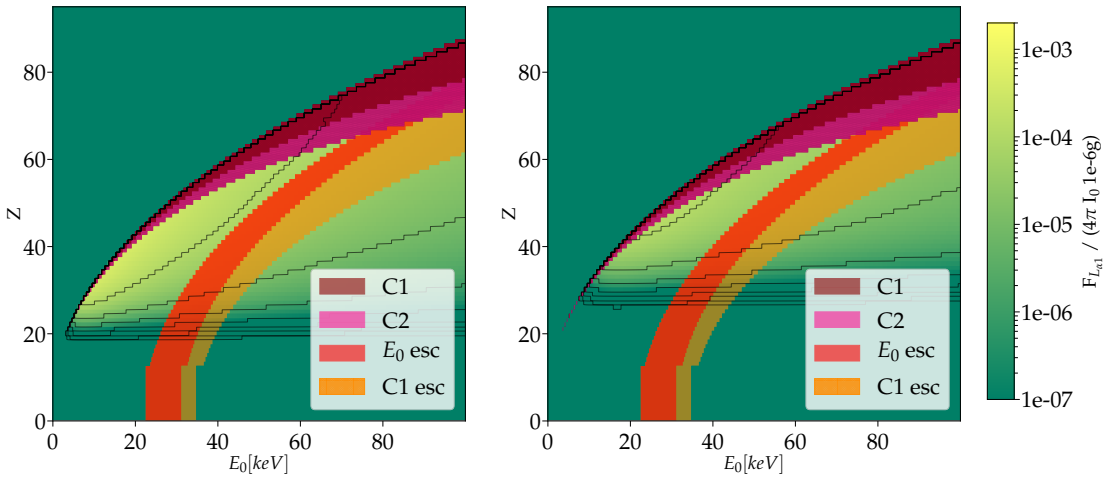

Figure 4.3 – Effective $K_{\beta 1}$ 4π fluorescence yield in a 0.1 cm (left) and 1 cm (right) radius water sphere depending on the incident energy E_0 and the $1e-6$ g tracer chosen with elementary number Z. A 1 mm CdTe detector chip was assumed. Highest yield are generally obtained closest to the absorbtion edge. In 0.1 cm phantom more than 1e-4 fluorescence photons per incident photon are detectable with an optimum at Z=40 with according incident energy of 20 keV. For the 1 cm phantom, generally one magnitude less is expected, but at Z=50 and $E_0 = 40$ keV also 1e-4 photon can be obtained.

Cadmium telluride detectors on the other hand maintain highest efficiency at high photon energies, as shown in 3.3. Thereby making this material best suited for high energy fluorescence. Compared to silicon the yield efficiency is vastly extended to higher incident energies E_0 and also higher Z. Anyhow these gained possibilities are limited by regions of escape events or Compton scattering. $K_{\alpha 1}$ fluorescence with Z>65 either is superposed by Compton background or, if higher incident energies are chosen, with escape events. Thus in experiments in this range a substantial background has to be expected. Better parameters can be chosen without large losses in yield. Z values between 40 and 65 still show a yield of more than 1e-4 photons. Possible background free incident energies range from 20 to 40 keV. Increasing Z put stronger limitations on the incident energy and requires larger deviation from the absorption edge to avoid Compton background. The situation for $K_{\beta 1}$ is worse as it is one of the fluorescence lines of highest energy.

4.3 Parameter Choice for Small Object XFI

For small objects with radii of roughly 1 mm, the largest range of possibilities is offered by the $K_{\alpha 1}$ shell using a CdTe detector, even though $L_{\alpha 1}$ reaches similar highest yields but is strongly limited to heaviest elements such as gold. More than 1e-3 fluorescence photons per incident photon can be expected in 4π. K-shell use allows elements from Z=30 up to 60, depending on the detector choice. Silicon prefers smaller Z as its efficiency shrinks drastically above a certain energy, see figure 3.3. CdTe use offers a slightly higher range of element choice but demands incident energy close to the absorption edge since otherwise detector escape peaks might create background in the fluorescence region. Further high Z, high incident energy K shell XFI is prone to Compton background of first or second degree which limits sensitivity. This is why Z<60 is recommended for small object XFI. $K_{\beta 1}$ generally is comparable to $K_{\alpha 1}$ with slightly less yield and more influence of the Compton regions due to the high energy of the K_β line. In objects with r=1 cm the $L_{\alpha 1}$ yield, 5e-5 photons in 4π, is drastically reduced compared to the r=0.1 cm case,yielding 1e-3 in 4π at Z=80. The K-shell lines are less strongly influenced by the phantom size due to less high energy fluorescence absorption. Absorption differences between r=0.1 cm and r=1 cm phantoms are minor compared to the L-shell case. Generally the here regarded Compton influence regions are corresponding to 4π. Using small detectors, Compton scattering of first order can always be avoided choosing the right detector placement angle.

5 Small Object Background Simulations Studies

Studies of XFI efficiency stretches over multiple variables which are: phantom shape, phantom size, detector type, detector position, incident photon energy or spectrum, XFI tracer, in phantom tracer position, tracer concentration and use of collimation devices [69]. Fully covering these dimensions poses strong demands on the limits of available computing power. Therefore general simulations were performed with spherical phantoms similar to assumptions made in 4, to study angle depending scattering of polarized radiation. First global background emerging from a spherical phantom to 4π is examined in spectral shape, quantity and angular orientation. This is relevant for large detectors or to find best suited angles for small detector placement. Detector positions and their expected spectra will be shown in detail after the 4π analysis.

5.1 4π Phantom - Radius - Energy - Variation

The parameters chosen to be varied are. First: phantom radius, from 1 mm to 50 mm [1,2,5,10,20,30,40,50]. Second: the incident energy was chosen to range from 5 to 110 keV [5,10,20,30,40,50,60,70,80,90,100,110]. Above 110 keV cross section losses are too large compared to higher transmission probabilities or not sensible due to detector effects as shown earlier in chapter 4. While Compton scattering leaves certain low energy spectral regions untouched, even with Doppler broadening [126], other are prone to Compton scattering. GEANT4 simulations are best suited to show such background distributions. Here angular distribution as well as Compton order, indicating how many Compton processes occurred for individual photons before detection, can be retrieved. Simulated geometry is a water

sphere with radius r enclosed by a spherical ideal detector, inner radius 1 m. Internal detector effects are ignored as they differ by detector choice. The forward beam direction is excluded since here primary incident beam would be detected. Excluded area is spherical with a diameter of 1 mm, in following plots this is at $\cos(\theta)$=1. Simulation parameters were: 1e8 horizontally polarized mono energetic incident photons in pencil beam profile with 1 mm radius.

5.1.1 Global Compton Background - Shape and Order

An important question of fluorescence imaging is: do Compton scattered photons reach the energy range of chosen fluorescence lines and in what quantity? Background influences the significance of expected fluorescence signals and more generally limits detector operation. Especially dead time needs to be kept low. Therefore detectors need to be placed where low background is expected or detector chip efficiency is negligible in the relevant background region. Silicon detectors therefore can tolerate high background count rate in high energy regions while CdTe detectors would be highly inefficient due to high count rate in such scenarios. Parameters dominating Compton scattering are the incident photon energy, as shown in 2.2.5 and phantom size by increasing possibilities for scatter events. Compton spectra from different phantom sizes, r=1, 10 and 50 mm, and incident energies E_0 of 10, 50 and 100 keV are shown in figure 5.1. Different scatter processes are color coded, Rayleigh scattering brown, C1 cyan, C2 yellow, C3 to C5 in different greens, further Compton scattering and other processes, e.g. bremsstrahlung, are filled with white enclosed by a blue line. Rayleigh scattering is recoded only if no other events occurred. If a photon is Rayleigh scattered and after words experiences Compton scattering, it is displayed as belonging to first order Compton scattered photons. Other processes are handled similarly.
Y axis is kept the same for all cases and shows the detected background photons per incident photon and per bin width ΔE.

Quality: Smallest phantoms with radii of 1 mm only provide marginal opportunities to scatter from. Here mostly coherent scattering, C1 and C2 can be expected for all energies up to 100 keV. The maximum energy loss per scatter event as in 2.6 yields 71.9 keV for 100 keV incident energy, 41.8 keV for 50 keV E_0 and 18.55 keV for 20 keV.

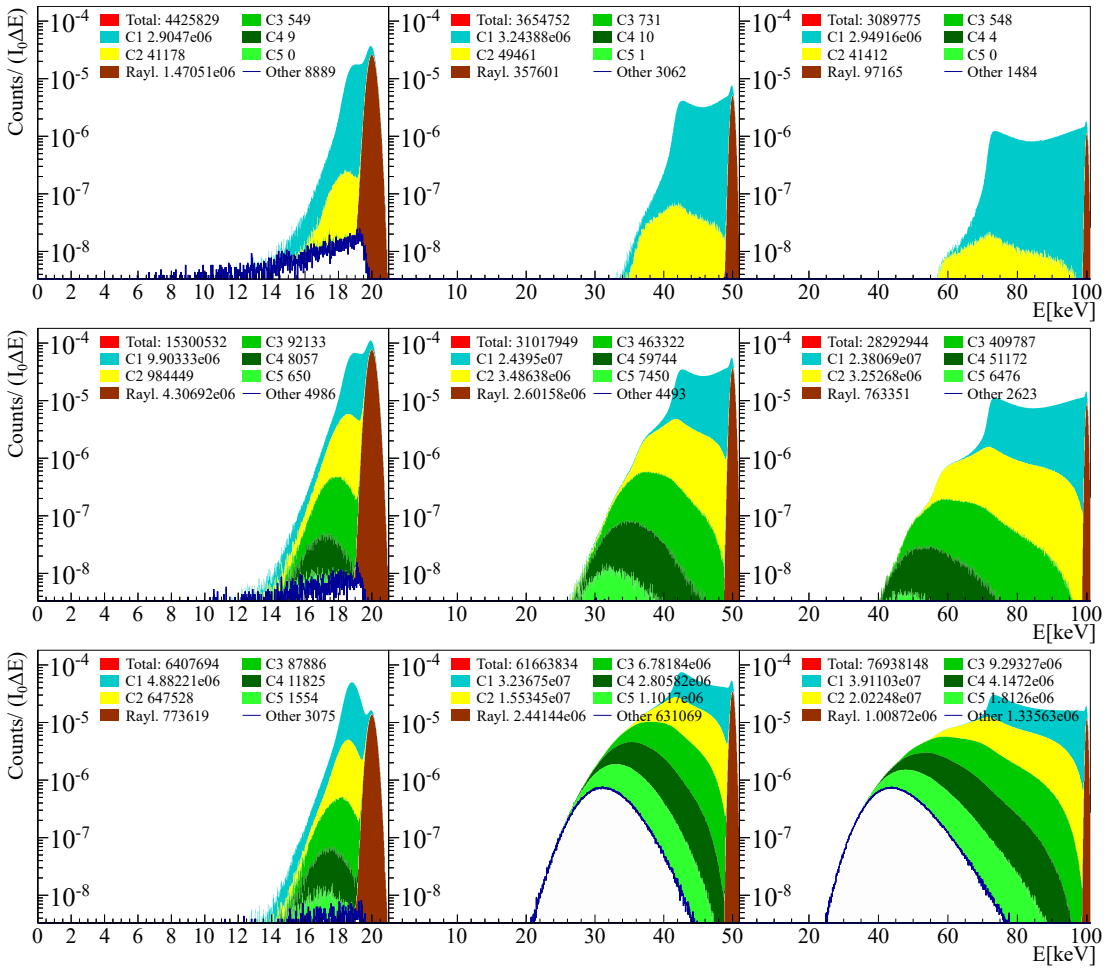

Figure 5.1 – Compton scatter spectra simulated with GEANT4 for a water sphere with radius 1 mm (upper row), 10 mm (middle row) and 50 mm (lower row) , incident energy is 20 kev (left), 50 keV (middle) and 100 keV (right). Displayed are scattered photon spectra originating from the phantom. By color process and multitude of scatter processes before detection are shown. Rayleigh scattering brown, single Compton scattering (C1) cyan, double Compton (C2) yellow, and further Compton scattering up to C5 different greens. Other processes and higher Compton orders are displayed in white. Forward beam direction ($\cos(\theta)$=1) is excluded.

These can be seen in the spectra as low energy peaks of C1. Further C1 to lower energies can be explained with the applied detector resolution and Doppler broadening [126] which is simulated in GEANT4 but not taken into account in 2.6. Therefore simulations show additional tails to lower energies. The scatter events under highest angle (180 °) are favored as shown in formula 2.9 as well as small angle scattering. The 90 ° suppression explains the valley between small angle and 180 ° scattered photon in C1 which is present for all cases

in figure 5.1. Higher Compton orders increasingly lose this feature and become isotropic. Minimum energies of higher Compton orders without Doppler broadening simply can be calculated with equation 2.7.

Quantity: Figure 5.2 displays the over all quantity of detected Compton orders per incident photon. Low energies show generally little amount of scattering for all phantom sizes. This effect is caused by the low Compton cross section at 5 and 10 keV, compare figure 2.11, and low transmission probabilities of scattered photons through the water phantom. After the rise on Compton counts at low energies, the individual Compton orders plateau, eventually declining minimally.

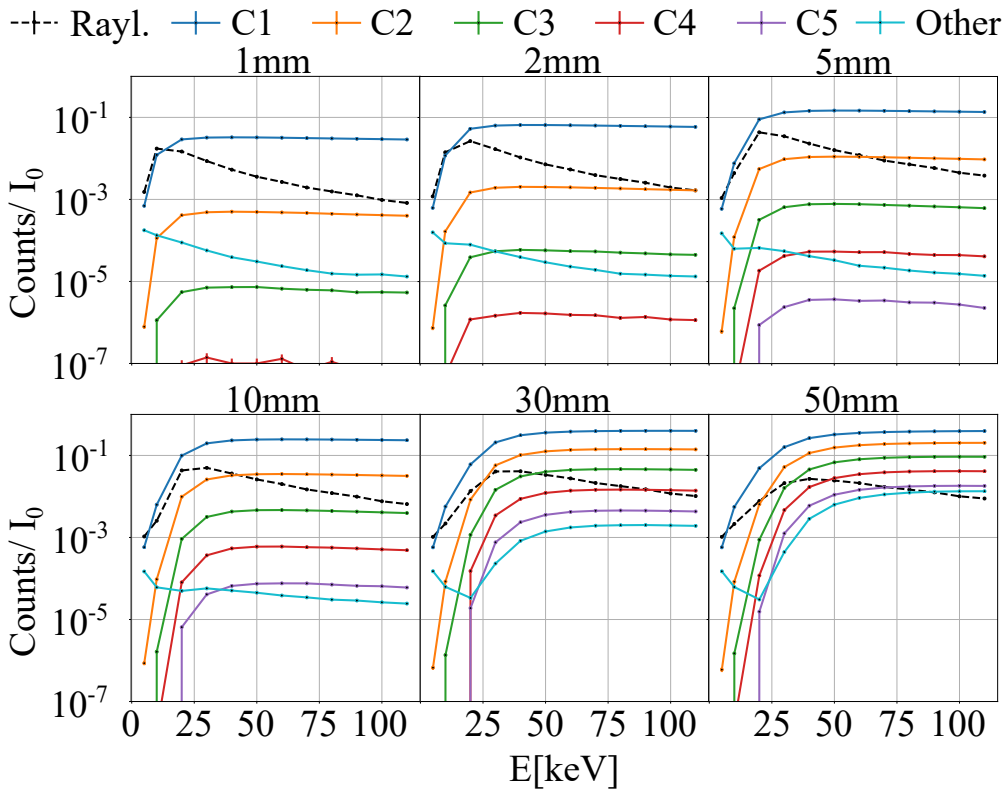

Figure 5.2 – Background counts per incident photon expected in 4π depending on the phantom radius, upper left 1 mm to bottom right: 50 mm. Energy was varied from 5 to 110 keV, photons were polarized horizontally. Data were obtained with GEANT4 simulations using a mono energetic pencil beam with radius 0.5 mm. Uncertainties are mostly smaller than marker size. Forward beam direction ($\cos(\theta)$=1) is excluded.

Rayleigh scattering is peaking at low energies, higher for larger phantoms, then declines exponentially as probability for secondary Compton interaction rises with energy or phantom size. For small phantoms and lower energies it is comparable in magnitude to C1. In large phantoms at high energies pure Rayleigh scattering becomes increasingly unimportant.
Category other is dominated in small phantoms by bremsstrahlung while larger phantoms higher Compton orders determine its shape.

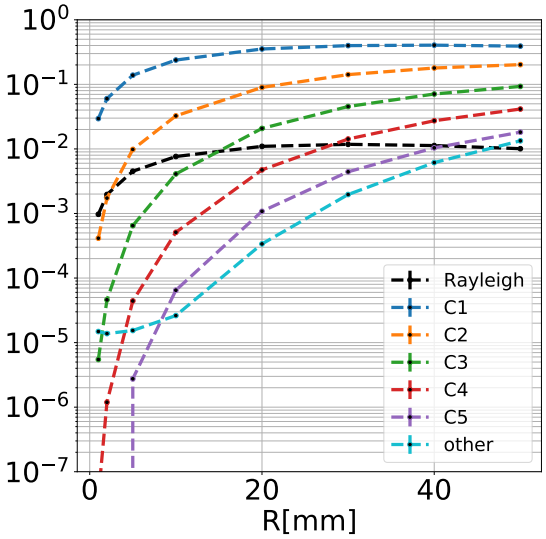

Figure 5.3 – Final plateau hight at 100 keV as shown in figure 5.2.

5.1.2 Global Compton Background - Angular Distribution

Good detector placement reduces Compton background influence significantly. The following maps of the whole solid angle show spatially background distribution for different phantom sizes. One pixel corresponds to 1e-4 Ω. Black lines mark levels of 1e-3, 1e-4, 1e-5 (continuous) and 5e-4, 5e-3 (dashed). Forward beam direction is $\cos(\theta)$=1 while back scattering will be detected at $\cos(\theta)$=-1. ϕ=0,π, $-\pi$ lies in the plane of polarization while ϕ=$\pi/2$, $-\pi/2$ is perpendicular to it.
As expected from the Klein Nishina cross section 2.9, in polarization plane 90 ° scattering shows the lowest total count rate as soon as incident energy reaches a level to penetrate the phantom sufficiently. Below that threshold the Compton background mainly occurs in the backward oriented hemisphere, $\cos(\theta)$=-1,0. With increasing energy the background distribution becomes symmetrical due to the symmetric target.

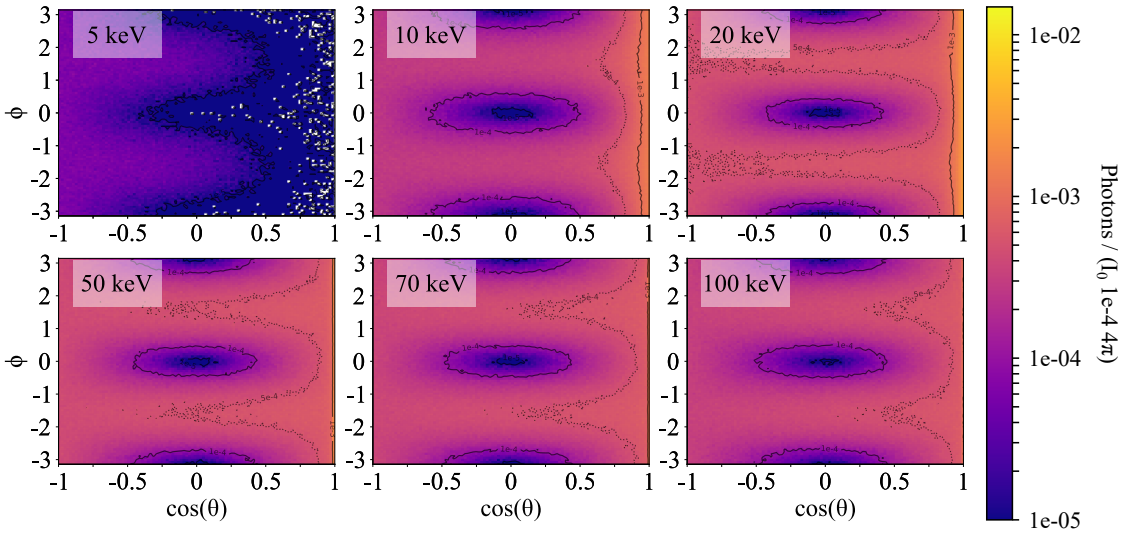

Figure 5.4 – The maps display the background distribution, simulated with GEANT4, for a water sphere with radius 1 mm. Forward beam direction ($\cos(\theta)$=1) is excluded. Each pixel represents 1e-4 of 4π.

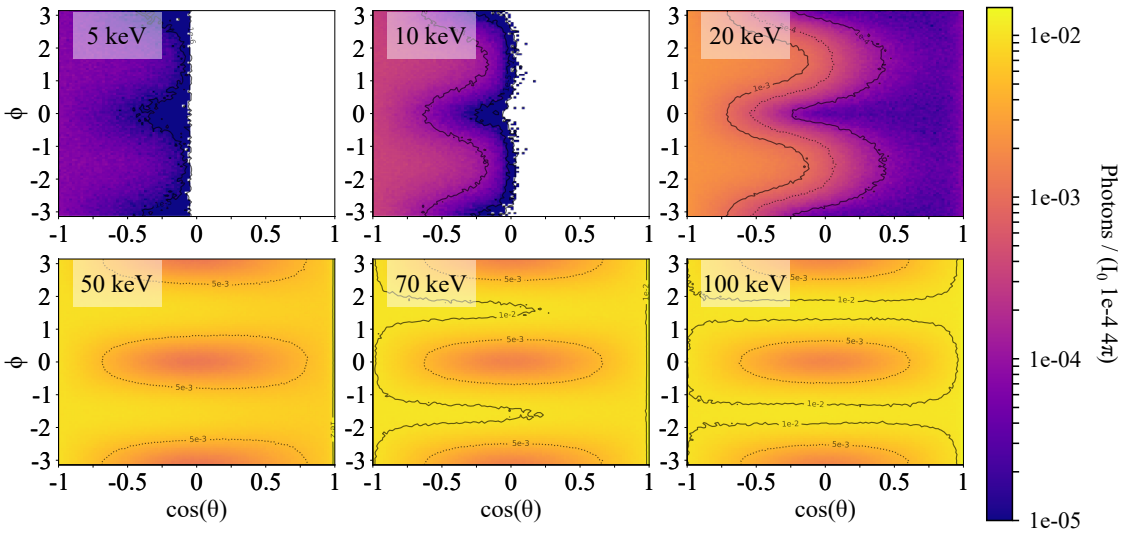

Figure 5.5 – The maps display the background distribution, simulated with GEANT4, for a water sphere with radius 50 mm. Forward beam direction ($\cos(\theta)$=1) is excluded. Each pixel represents 1e-4 of 4π.

In the case of 1 mm radius minimum background count rate per 1e-4Ω is below 1e-5 Counts/I_0 for symmetric scenario. This value rises in larger phantoms. In r=20 mm slightly below 1e-3 Counts/I_0 can be expected, while r=50 mm yields slightly less than 5e-3 counts/I_0. With increasing phantom size minimum count rates increase, but are more

wide spread concerning the θ angle. Thus detector placements differing from $\theta = 90\,^\circ$ are less punishing in the total count rate in larger phantoms. Small probes on the other hand should be imaged under $\theta = 90\,^\circ$ to enable low background and low detector dead time.

5.1.3 Local Compton Background - Selected Angles Spectral Shape

Even if the total count rate does not fluctuate strongly in the cases of θ variation, the spectral background shape will. This is essential for the use of small detectors as by choosing its place, in θ and ϕ, the background shape might change significantly. In the following a 1 sr of the whole detector sphere is chosen, and detected spectra are shown. 1 sr compares to a 1 cm^2 detector area in 10 cm distance to the beam - phantom intersection center, typical dimensions for a synchrotron based XFI experiment.

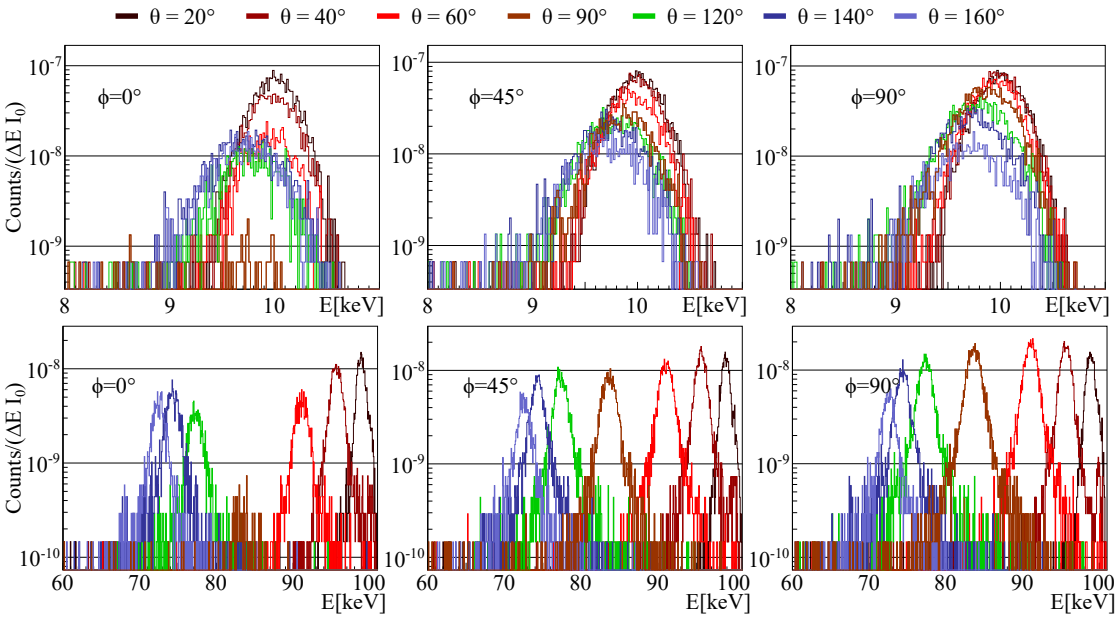

Figure 5.6 – Compton spectra emerging from a 1 mm radius water sphere irradiated with linearly polarized light, detected in 1 sr at various θ angles. Left column shows detector position parallel to the light polarization, middle column 45 ° and right column orthogonal detector placement to light polarization. The initial photon energy is 10 keV, upper row, and 100 keV lower row.

In small phantoms the spectral background is dominated by Compton 1, as shown in figure 5.1, especially so for high energies. Therefore the angular spectral dependencies are expected to be sharp and significant, here shown for E_0=10 and 100 keV with r=1 mm

in figure 5.6. In the plane of polarization ($\phi = 0\,°$), 90 ° scattering is highly suppressed with 1e-9 counts/($\Delta E\, I_0$) peak count rate. Orthogonal to polarization ($\phi = 90\,°$) this suppression is not visible. At 10 keV high angle scattering yields a peak count rate of 1e-8 Counts/($\Delta E\, I_0$) and low angle scattering slightly less than 1e-7 counts/($\Delta E\, I_0$). In low energy realms θ choice has minor influence on mean Compton peak energy. 100 keV photons yield a higher suppression at 90 ° in the $\phi = 0$ case and on the other hand favors 90 ° scattering in orthogonal polarization plane ($\phi = 0\,°$). Peak count rates here are generally lower compared to the 10 keV case. This effect is caused by lower interaction probability of high energy photons and also by worse detector resolution at high energies. To compare total count rates, see figure 5.8.

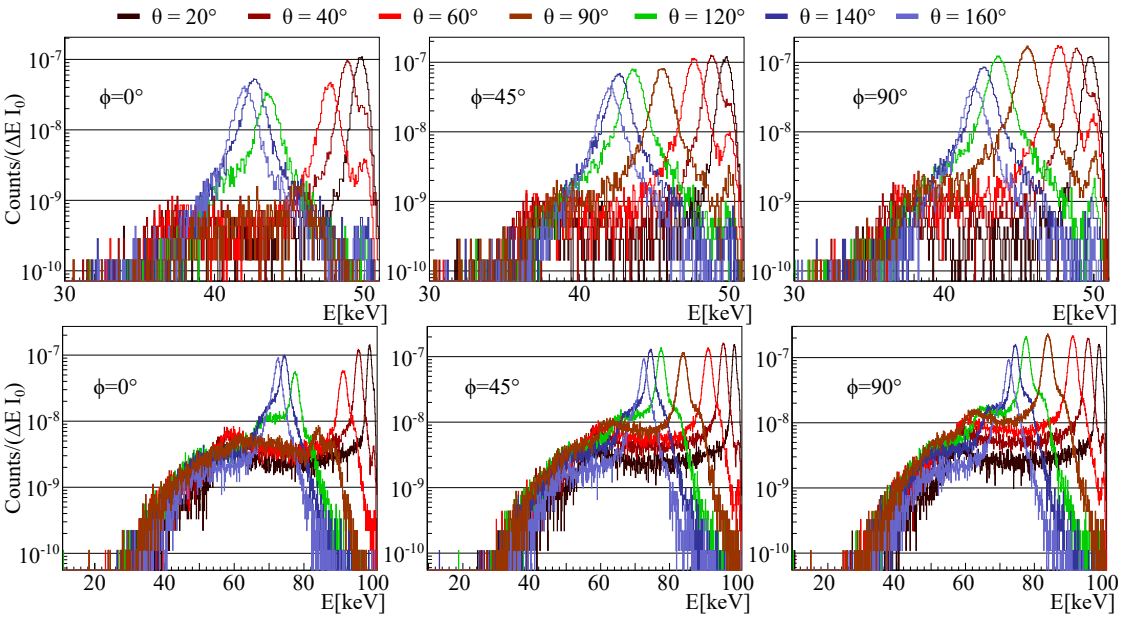

Figure 5.7 – Compton spectra emerging from 5 mm radius (upper row) and 50 mm radius (lower row) water sphere irradiated with linearly polarized light, 50 keV (upper row) and 100 keV (lower row), detected in 1 sr at various θ angles. Left column shows detector position parallel to the light polarization, middle column 45 ° and right column orthogonal detector placement to light polarization.

Within larger phantoms multiple Compton scattering reduces this high specificity, peaks broaden and a bulge of higher Compton orders reaches down to lower energies. This is shown in figure 5.7 for r=5 mm, E_0=50 keV (upper row) and r=50 mm and 100 keV (lower row). Even though prominent C1 peak energy is highly sensitive to θ choice, final low energy tails behave similarly for all angles. Plateau heights in the 50 keV and r=5 mm case

are not clearly distinguishable but range from 1e-10 to 1e-9 Counts/($\Delta E\, I_0$). Maximum peak heights of 1e-7 Counts/($\Delta E\, I_0$) are to be expected in $\phi = 90\,°$ and $\phi = 45\,°$. For $\phi = 0\,°$, under $90\,°$ scattering only 1e-9 Counts/($\Delta E\, I_0$) are detected. Again, deviations from this angle rapidly increase the count rate by a magnitude.
Peak count rates in the 50 mm radius phantom irradiated with 100 keV photons exceed 1e-7 Counts/($\Delta E\, I_0$). The plateau heights are roughly of similar height in the $\phi = 0$ case with 3 to 5e-9 Counts/($\Delta E\, I_0$). With increasing deviation from $\phi = 0$ the plateaus separate with count rates of up to 2e-8 Counts/($\Delta E\, I_0$). The low energy tails terminate between 30 and 40 keV.
Integrated count rates, relevant for dead time considerations are shown in figure 5.8 (1 mm phantom) and 5.9 (50 mm phantom). The polarization effect is best visible in the small phantoms.

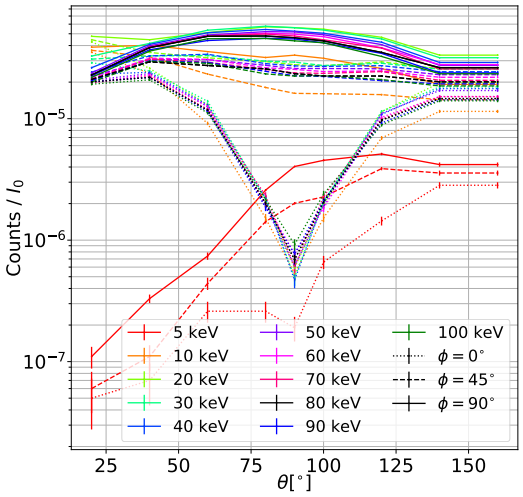

Figure 5.8 – Expected photon count rates per on target photon on a 1 mm radius water sphere for a detector covering 1 sr at different θ placements and orientation to light polarization, parallel (ϕ=0°) to orthogonal ϕ=90°. Incident energies were varied and are color coded from 5 to 100 keV.

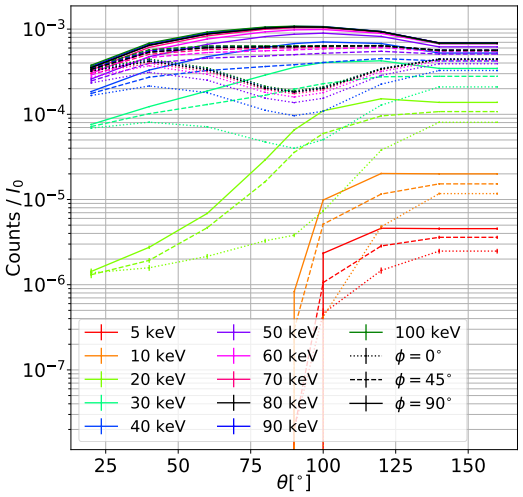

Figure 5.9 – Expected photon count rates per on target photon on a 50 mm radius water sphere for a detector covering 1 sr at different θ placements and orientation to light polarization, parallel (ϕ=0°) to orthogonal ϕ=90°. Incident energies were varied and are color coded from 5 to 100 keV.

6 L-shell Cellular Gold Nano Particle Uptake Study

Heavy element L-shell fluorescence is most sensitive in small objects. Therefore gold nano particle uptakes can be studies with smallest cell samples of only a few hundred irradiated cells. This sensitive analysis is demonstrated in the following.

6.1 Setup and Targets

6.1.1 PC3 Cell Targets and Nano Particles

In vitro gold nano particle loaded PC3 cells (prostate cancer cells line 3) were analyzed non destructively via XFI. A small sample of less than 1000 cells was used to determine the cellular gold uptake quantitatively. Cells were exposed for 24 h to a nano particle solution with 12.5 nmol/L, corresponding to 0.13 mg/mL. The nano particles were spherical and 12 nm in diameter.

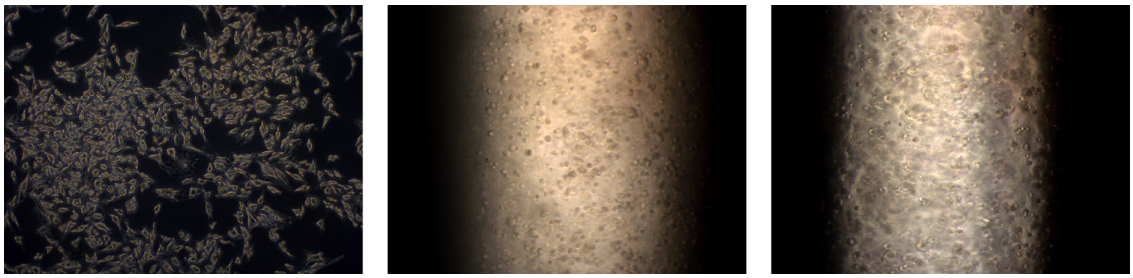

Figure 6.1 – Prepared PC3 cells. Left: mono layer attached to a surface. Middle: In capillary PC3 cell agarose mixture with 5e3 cells/µL. Right: PC3 agarose cell mixture with 2.5e5 cells/µL in capillary. Photos taken by N.Behm.

Even though *in vitro*, particles were treated with polyethyleneglycolmercaptoundecanoic (PEGMUA) [163] which reduces toxicity and enhances blood circulation time. To increase the cellular specific uptake the nano particles were functionalized with prostate specific membrane antigen inhibitor (PSMAi). PSMA is highly expressed in prostate tumor cell membranes and is investigated as biomarker for prostate cancer imaging and therapy [164][165]. Nano particle preparation was performed by F.Schulz and S.Graf (Institut für Physikalische Chemie Hamburg), cells were cultivated by N. Behm (Universitätsklinikum-Hamburg-Eppendorf). Cell agarose mixtures were filled in bore silicate glass capillaries with an diameter of 2 mm and wall thickness 0.05 mm. Concentrations were 5e3 and 2.5e3 cells/µL. Surface attached, cells display elongated shape in agarose they are mostly spherical, as shown by microscopy images in figure 6.1. The spherical diameter ranges from 15 to 20 µm.

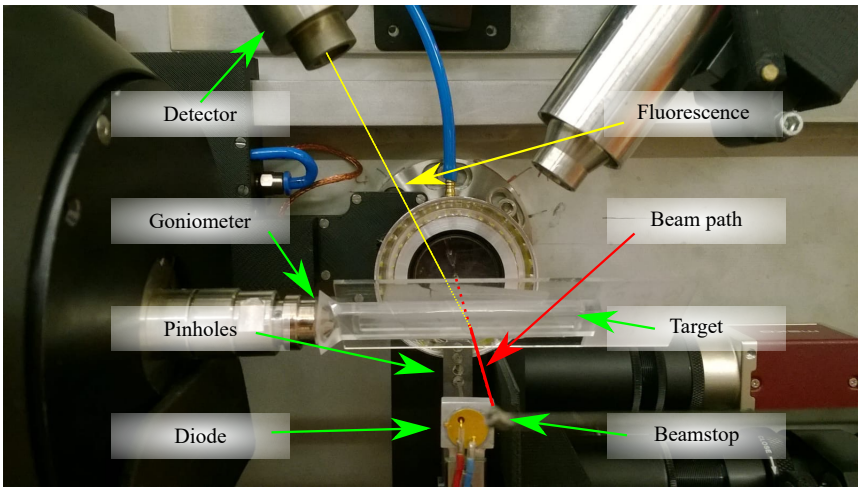

Figure 6.2 – Experimental setup at the P11 beamline experimental endstation. To shape the beam, tantalum pinholes can be inserted into the beam path, the beam then permeates the target (here cell monolayer) and is dumped in the platinum beamstop. The flux can be measured with a diode.

6.1.2 Setup

Experimental space was sparse at the P11 beamline, available setup is shown in figure 6.2. It extended roughly over 10 cm from beam pinhole to beam stop. In between the probes were mounted on the goniometer, allowing for small translations in x, y and z and for rotation along its axis. Beam diameter was chosen 200 µm via pinhole shaping. Thereby 622 cells should be irradiated in the high concentration sample and 311 in the lower one, still

enough to eliminate statistical uncertainties in cell size. Photons are horizontally polarized, detector is mounted 60 ° to the horizontal plane. The beamline owned collimator was used and detector probe distance was extended to the maximum, 6 cm. Still the detector showed a continuous dead time of 90% or higher. It was found later that a spectrometer card had a malfunction which lead to highly increased noise. This does not question later results, since dead time is a question of necessary measurement time, which will be discussed in section 6.3.

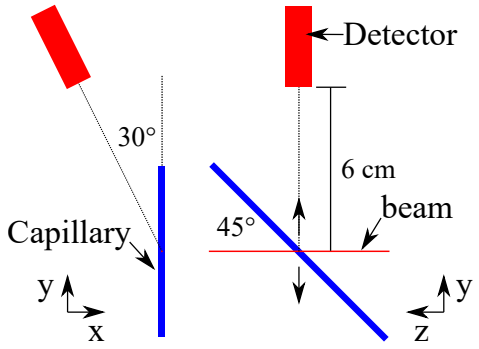

Figure 6.3 – Schematic sketch of the Capillary mount geometry. Left: frontal geometry as in figure 6.2, right, side view.

Probes and Scans

In total four different capillaries were examined. Those contained cells treated with gold nano particles functionalized with: PSMAi+ and MUA (5e5 cells/µL), PSMAi+ (5e5 cells/µL), PSMAi+ (2.5e5 cells/µL) and unfunctionalized cells (5e5 cells/µL). These capillary targets were mounted on the goniometer in 45 ° to the incident beam, a schematic sketch is shown in figure 6.3 from side (right) and front (left). With small steps, 200 µm, the target was moved vertically through the beam to image different cells off the same functionalization type. Small horizontal deviations of the target beam intersection due the 45 ° tilt is neglected in later analysis, as it is small compared to the large target detector distance.

Beamline Intrinsic Background - Zero Measurement

The P11 Beamline setup consists of various materials, each a source of fluorescence, causing a potential background peak.

Heavily irradiated objects are beamstop and pinholes consisting of tantalum, Z=73, (beamstop) and platinum, Z=78, (pinholes). Otherwise the materials in vicinity to target beam intersection are not known. A zero measurement was taken to determine background in

later fits, shown in figure 6.4 with the range of expected gold fluorescence in figure 6.5. Lines in the following are given with their name, energy in keV and their relative intensity, e.g. $L_{\beta 1}(9.34\,keV,67(\text{rel.Int.}))$. Tantalum fluorescence (cyan) is clearly visible in the zero measurement: $L_{\beta 1}(9.34{,}67)$, $L_{\beta 2}(9.65{,}20)$, $L_{\gamma 1}(10.9{,}12)$ were fitted, as is platinum (pink) which was also fitted with the lines $L_{\alpha 1}(9.44{,}100)$, $L_{\alpha 2}(9.36{,}41)$, $L_{\beta 1}(11.07{,}67)$, $L_{\beta 2}(11.25{,}23)$. Further unidentified lines (black) were added to model remaining background. These lines rest on a constant plateau caused by electron escape events, see section 2.4. Compton background and plateau were fitted for this measurement with a third grade polynomial and an exponential function. The polynomial covers the detector plateau, while the exponential function fits the Compton flank. It is assumed that small low Z probes do not alter the background fluorescence function, as modeled in figure 6.5, drastically. Low energy background photons might be subject to more absorption in a present target, compared to high energy background photons. Fits of all subsequent data use this fluorescence background, with two parameters. Which is one: the absolute height H_B, and second: a weight factor $a_B > 0$ to increase the influence of high energies compared to lower ones, to deal with potential fluorescence background absorption in probes:

$$B_{att} = H_B \sum_i \exp\left(a_B(\mu_i - 8000)\right)\ \text{Gaus}(\mu_i, \sigma_i, A_i), \tag{6.1}$$

this function is shown in figure 6.5 as the blue line.

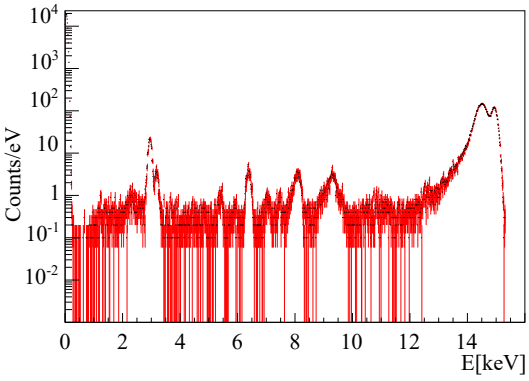

Figure 6.4 – Measurement without probe. Beamline intrinsic fluorescence peaks are clearly visible.

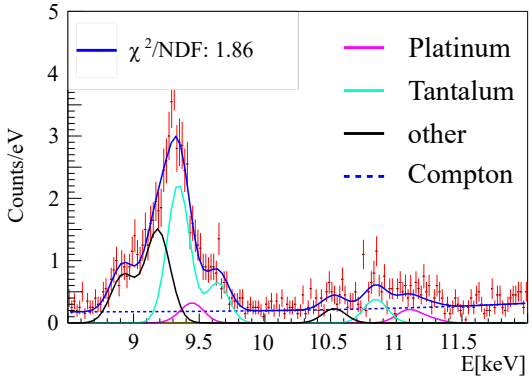

Figure 6.5 – Background determination in the gold signal region, the main Ta (cyan) and Pt (pink) fluorescence lines are implemented accordingly to their intensities. Blue dotted: Compton background, black: Other lines. Blue: Fluorescence background for subsequent fits.

Sputter Targets

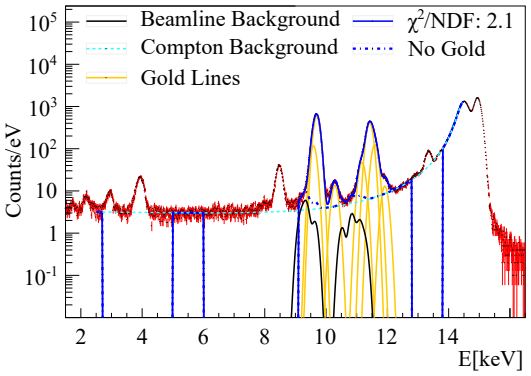

Figure 6.6 – Sputter target spectrum with 15 keV incident energy. Spectrum not corrected.

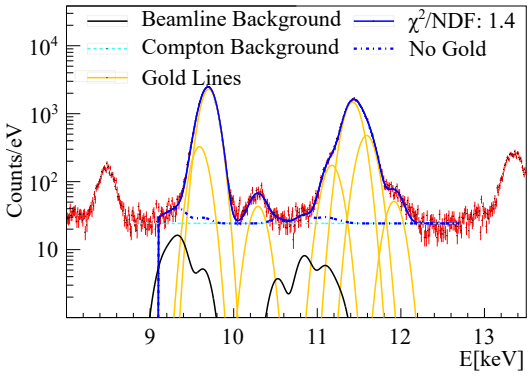

Figure 6.7 – Sputter target spectrum with 20 keV incident energy. Spectrum not corrected.

A sputter target was used for energy calibration and later gold mass reconstruction. This target is a (20.8 ± 0.8) nm gold layer sputtered on 1 mm × 25 mm × 25 mm silicon substrate positioned with a 45° tilt similar to the capillary position shown in figure 6.3. 20 keV and 15 keV were used for irradiation, resulting spectra are shown in figure 6.6 and 6.7. They are not corrected for dead time or incident flux, see section 6.3 for this discussion. Significant here are the differences in Compton background. 15 keV incident energy scatters down to 10 keV, thereby the gold fluorescence lines do rest on an exponential slope. Which is, due to the multitude of lines covering a broad part of the slope, difficult to fit. A fit model for mono energetic tailing behavior in Si detectors [151] was applied. Thin gold layer and low Z silicon do create a mostly mono energetic Compton peak, therefore this model might be applied which is described by

$$C(E) = A\left(\frac{\Gamma}{(E-E_0)^2+\Gamma^2} + p_1[1-\exp(-p_2(E-E_0))\exp(p_3(E-E_0))]\right). \qquad (6.2)$$

The free parameters A, p_1, p_2, p_3 and Γ were derived from fit, E_0 was chosen to be 8 keV. 20 keV incident photons leave the background of the gold fluorescence region constant. The later fitted gold line shape was deduced from theses spectra, their position and relative intensity, the lines $L_{\alpha 1}(9.71\,\text{keV})$, $L_{\alpha 2}(9.63\,\text{keV})$, $L_{\beta 1}(11.44\,\text{keV})$, $L_{\beta 2}(11.58\,\text{keV})$ and three further lines: LE(10.31 keV), $\text{L}_{\beta 10}(12.06\,\text{keV})$ and $\text{L}_{\beta 4}(11.21\,\text{keV})$ were used, minor ones were ignored here. Therefore mean peak values might deviate a little from literature, as only seven Gaussian peaks were modeled to account for all gold fluorescence lines in this energy region. Still the sputter target high gold intensity spectra are well fitted with a $\chi^2/ndf = 1.4$ in the 20 keV case.

Reference Targets, Agarose Gel, Cell Monolayer

Representing the same geometry and material as later targets, glass capillaries filled with agarose and cells with a high amount of gold. An additional transmission factor for line intensities, compared to the sputter target was applied, as gold fluorescence line peak ratios shift due increased absorption in water. Additionally cells or the agarose gel contains arsenic and to a minor extent bromine, of which fluorescence lines overshadows the right flank of the L_β gold peaks.
Even though the capillaries had a minor diameter of 2 mm, this is enough to cause no negligible amounts of Compton scattered photons, as water displays a high Compton cross section. Therefore 6.2 with minor variation can be applied here. The low energy tail still is of importance, but the peak does not describe the Compton tail sufficiently. The formula has been slightly modified to

$$C(E) = p_0\,(1 - \exp(-p_1(E - E_0))\exp(p_3(E - E_0)) + \exp(p_4(E - E_0) + p_5))\,, \qquad (6.3)$$

which can not describe the Compton peak, but it's left flank, which is sufficient for gold fluorescence measurements. The low energy plateau is still described correctly.
For the agarose gel probe fits, see figure 6.8, the main peaks are here due to arsenic, which dominates the relevant spectrum. Peaks at 10.5 keV, K_α lines, are fitted with one single Gaussian, which also applies to K_β lines at 11.72 keV. The ratio, positions and width from this fit will be used in the following analysis.

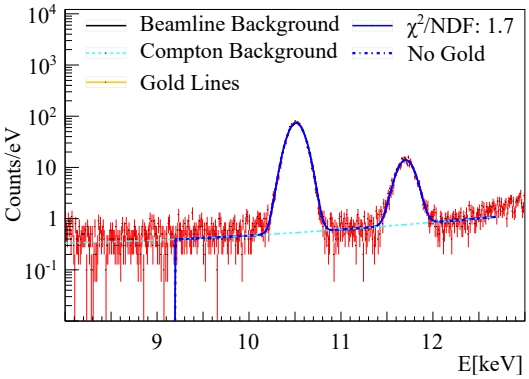

Figure 6.8 – Capillary with agarose only, displaying arsenic, two K_α lines at 10.5 keV and two K_β at 11.72 keV, each fitted with a single Gaussian.

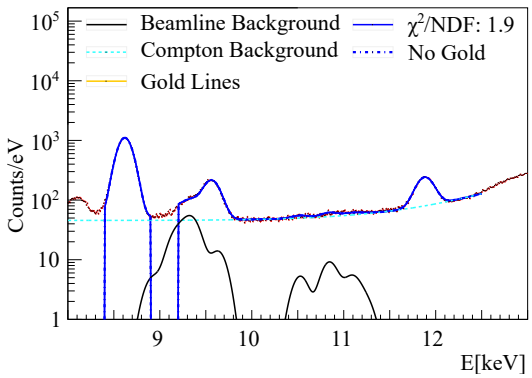

Figure 6.9 – Cell mono layer showing zinc, blow 9 keV and bromine above 12 keV.

The cell mono-layer spectrum displayed in figure 6.9 shows large peaks of zinc fluorescence as well as bromine, but almost no arsenic. Simplified fit shapes were used to address these elements, two Gaussian functions per element, the values of which are shown in table 6.9.

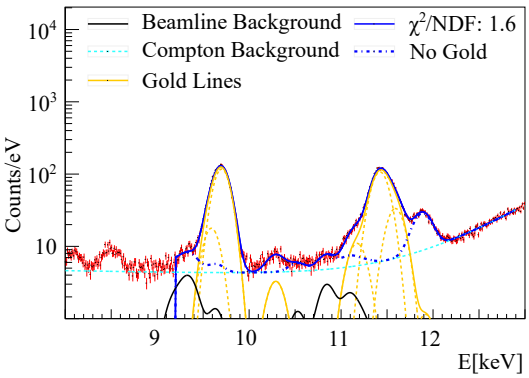

Figure 6.10 – Spectrum of reference target, MUA cells loaded with 12.5 nM gold.

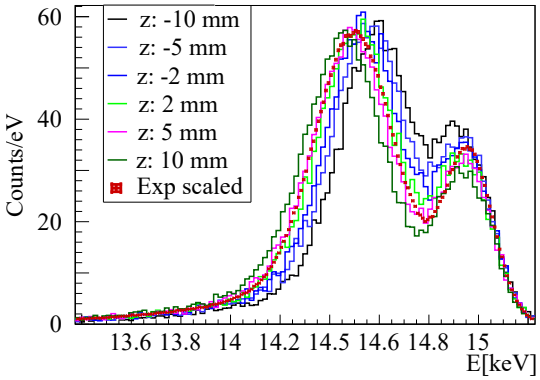

Figure 6.11 – Simulations with capillary at different position along the beam. Experimental data is scaled to fit counts between 13.8 and 15.2 keV and the z=5 mm position. Z=0 mm equals perfectly positioned capillary.

Reference targets are similar to later PC3 capillary targets, but offer a high amount of gold. The application of arsenic, zinc, bromine fluorescence with the inclusion of the beamline fluorescence background and the modified Compton tail formula, equation6.3, is demonstrated to model the X-ray response of a capillary filled with gold loaded cells at the P11 experimental station, shown in figure 6.10. With the information from various target analysis above, free parameters remaining are: the Au-, Zn-, As-, Br-height, six further parameters determining the background due to Compton scattering (in equation 6.3), the beamline background height and the energy attenuation factor for the beamline background in equation 6.1.

As Line[keV]	rel int	Zn Line [keV]	rel int
10512	100	8619.15	100
11703	18.19	9560	14.8

Figure 6.12 – As and Zn line positions and rel Intensities found by dataset No31 and No30, see figure 6.8 and 6.9

6.1.3 Mass Reconstruction and Uncertainty Estimation

The formulas in section 3.5.2 were applied here. As a reference target a silicon wafer with (20.8 ± 0.8) nm Au layer has been chosen. Due to a tilt of 45° along the horizontal axis, the amount of gold in the photon beam with a diameter d of (200 ± 2) µm and $\rho_{Au} = 19.3\,\mathrm{gcm}^{-3}$ is:

$$m = \pi\,(d/2)^2 \frac{\rho_{Au}(20.8 \pm 0.8)\,\mathrm{nm}}{sin(45°)} = (17.84 \pm 0.69)\,\mathrm{ng} \tag{6.4}$$

The cell count uncertainty is estimated by its statistical uncertainty: $\Delta_{N_c} = \sqrt{N_c}$: 622 ± 24.9.

6.2 Simulations

Since experimental setup was far from optimal as it was strongly restricted by the beamline, simulations were performed to estimate optimal conditions. Here mainly the detector position should be varied, especially the angle to light polarization plane. The experimental detector position was 30 ° to the orthogonal case. Simulated were 0, 30, 60 and 90 ° with respect to the vertical. This angle is shown in figure 6.3(left), thus 90 ° correspond to the detector being in the polarization plane, and 0 ° orthogonal to it. Probability for Compton detection is drastically influenced by this parameter as shown in chapter 5 and the polarized Klein-Nishina formula 2.9.
1e10 photons of 14.95 keV were simulated. Only air, capillary, detector and capillary content, consisting of water with a gold concentration of 0, 0.01, 0.05 or 0.1 mg/mL was simulated. Other beamline setup was ignored, therefore simulations lack beamline intrinsic fluorescence peaks. The capillary was found not to be hit exactly perpendicular to the detector, but 5 mm off. Capillary position was varied for a few mm, as small deviations were expected as explained in section 6.1.2. By Compton and Rayleigh peak position comparison shown in figure 6.11 the capillary offset was decided to be simulated with 5 mm to match experimental data.

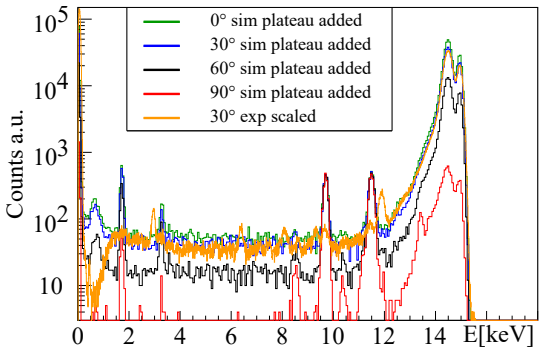

Figure 6.13 – Simulated spectra with different detector angles, 0 (green), 30 (blue), 60 (black) and 90° (red). 90° equals detector in plane of polarization. Au concentration here was 0.01 mg/mL. Experimental case was 30°, example spectrum shown in yellow.

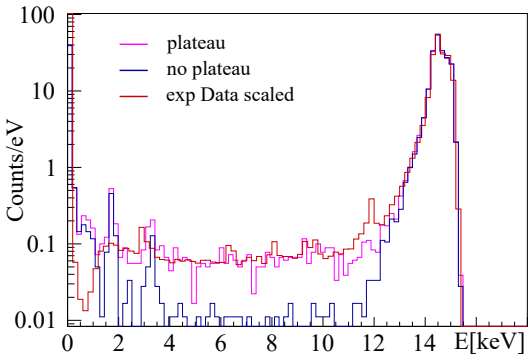

Figure 6.14 – Comparison of simulated spectra with added plateau (magenta), no added plateau (blue) and an experimental spectrum (red).

Experimental measurements displayed a non negligible low energy plateau up to the Compton peak. This is mainly not reproduced by simulations. It is assumed that these counts are partially detected events which experience loss of the charge due to vicinity to chip surface, see section 2.4. Charge dynamics in the chip were not simulated and thus need to be added artificially after simulation. To account for this, for each photon detected with E>14 keV, an additional entry was randomly added between 0.5 keV and the detected primary photon energy with a probability of 2.5 %. This value was found by comparing experimental spectra between 5 and 6 keV and number of entries above 14 keV to exclude fluorescence lines. A simulated spectrum with added plateau and without is shown with experimental Data in figure 6.14. Deviations at 12 keV might be caused by the bromine fluorescence peak in the experimental spectrum and the neglection of curved nature of the plateau, therefore too few counts might be added artificially at 12 keV to model the background correctly.
Simulated spectra of different detector angles with plateau are shown in figure 6.13, each a concentration of 0.01 mg/mL gold was applied. To determine signal significances, no fits were applied. Fluorescence and background photons were counted in the corresponding energy interval with subsequent statistical analysis equal to the experimental case.

6.3 Results

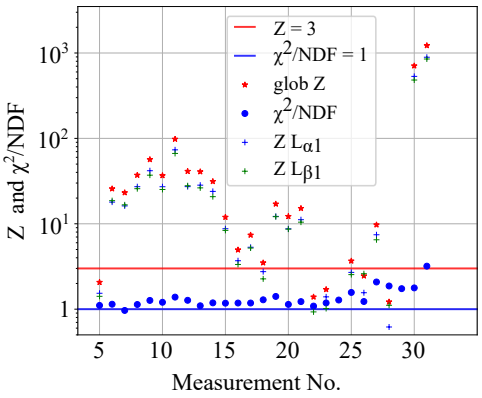

Figure 6.15 – Calculated significances of all performed measurements, for $L_{\alpha 1}$ and $L_{\beta 1}$ peaks and combined significance (in σ, left y-axis) and each χ^2/n value for the fits. Mostly close to 1 demonstrating an over all well performing fit over magnitudes of gold signifcances.

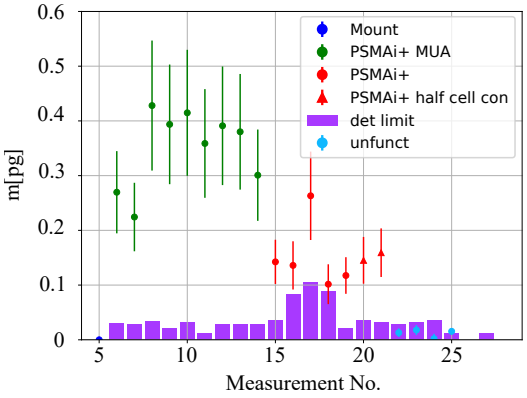

Figure 6.16 – Reconstructed gold mass per cell with corresponding detection limits (magenta) for four different probes, PSMAi+ with MUA (blue), PSMAi+ (red dot), PSMAi+ with half the number of cells in the beam (red triangle) and cells with unfunctionalized nano particles (green cross).

Fitting spectra over a long range from 8 to 15 keV including multiple external fluorescence peaks, Compton scatter background as well as detector plateau is a challenge. Differing targets offer more or less material to scatter from and therefore change background substantially while gold amounts also ranged over magnitudes from sputter targets to cells with no detectable gold inside. Significance and χ^2/ndf of each fit is shown in 6.15 including the relevant limits of Z=3 σ and $\chi^2/ndf = 1$. Most cell targets yielded 10 to 100 σ. Times of measurement ranged from 30 to more than 1000 s. While some of the recorded spectra featured prominent gold peaks, other probes would not. An in-depth background analysis enabled the detection of significant signals even though some spectra appear to be flat or background dominated at first sight. PSMAi+ with MUA functionalization provided a cellular uptake of 0.3 to 0.45 pg, which caused signals with significances of more than 20 σ even with varying measurement periods. The consistently reconstructed mass per cell over different positions ensures to be no singular phenomenon. Without MUA the uptake shrinks to 0.1 to 0.15 pg per cell. Here the Au signals were close to insignificance for shortest times of measurement, being 30 s, noticeable by the raised detection limit for measurements no. 16, 17 and 18 in figure 6.16. Mere AUNPs without functionalization were, even with long exposure times, mostly not verifiable.

Experimental data should follow the relation described in 3.5.3, values for this experiment are shown in figure 6.18. Here each probe is shown by a different marker color. Sputter target and capillary measurements are displayed here. The comparatively high sensitivity of the 20 keV sputter target measurement suggests this incident energy to be preferable to the others, for which 15 keV was used. Anyway a single data point might only be interpreted as a hint. Despite the exponential decrease of fluorescence cross sections with increasing energy the background here is merely present by detector effects and therefore almost flat, compare figure 6.6 and 6.7. For the 15 keV case sputter targets and cell probes both match the linear relation within the error bars.

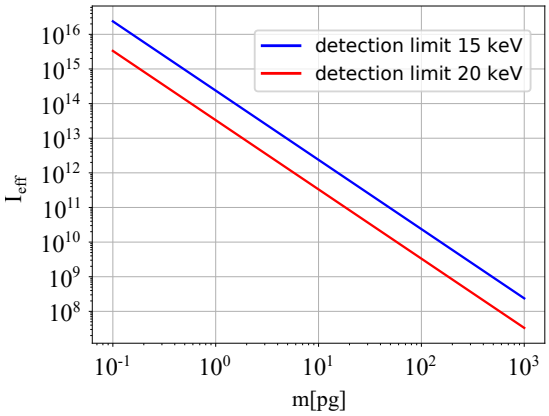

Figure 6.17 – Extrapolated necessary minimum number of effective incident photons for magnitudes of different gold amounts in the irradiated probe.

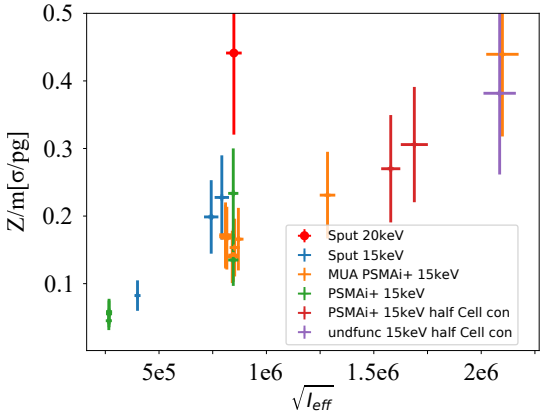

Figure 6.18 – Z/m over $\sqrt{t_{eff}}$for experimental data. Individual target types and incident energies are resolved here.

Simulated and experimental data are shown in figure 6.19 and fitted with equation 3.14. Simulations differed in the detector angle and gold concentration. Only the angle should impact the experimental sensitivity Z/m as it highly influences background count rates. Therefore simulation fits are based on three data points each, corresponding to the concentrations 0.01, 0.05 and 0.1 mg/mL. As expected detector position at 0° shows lowest sensitivity due to the position being orthogonal to light polarization. With increasing angles, 30, 60 to 90° sensitivity improves. The 90° simulations suffer from low statistics as comparatively few scatter counts are detected. This is visible as the data points do not converge. An estimation by counting Compton and Rayleigh events and comparing the 90° and the 0° case lead to an even higher sensitivity for the 90° detector position, shown as the red dot. This data point is not considered in any fit but supports the high 90° sensitivity even though the high uncertainties.

Experimental data is fitted in two categories, 15 keV and 20 keV incident energy. Both used the 30° detector position. The blue fits therefore should overlap ideally. Reasons for deviations here are beamline intrinsic fluorescence, e.g. tantalum or platinum, in target fluorescence as bromine or zinc, and deviations from the artificially added detector plateau. As such an ideal overlap is not expected. The data are presented in figure 6.19 for the L_α-range (right panel) and the global range (left panel), taking into account both, the L_α and the L_β range. Because the L_α peaks rests on a mostly flat plateau which is imitated by the artificially added plateau. Therefore here a good agreement between simulation and experimental data is expected. On the other hand, the L_β line already experiences the flank of the Compton peak. A flat plateau here is not a perfect approximation. Hence the background here is probably underestimated in the simulations which yield a higher sensitivity. These effects explain the differing behavior of simulations in the figures of 6.19.

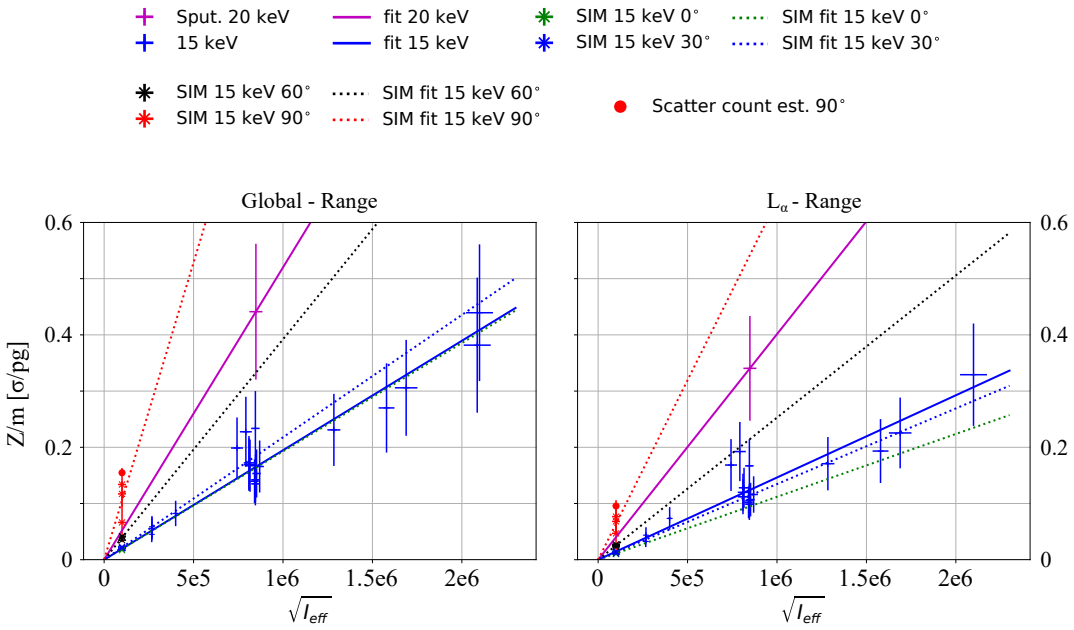

Figure 6.19 – Significance[σ] per gold mass[pg] plotted over the root of effective incident photons for experimental and simulated data. Left: L_α and L_β gold fluorescence regions were considered. Right: only L_α region data is shown.

The slope values of the fits are shown in table 6.20, which can be used for extrapolation of sensitivity limits of similar experiments. The 20 keV case for which only one data point was taken is significantly more sensitive than the 15 keV cases. Simulations were not done as the post simulation plateau addition would require more independent data points to justify a certain plateau height, which is the main cause of background in the fluorescence region.

If the plateau is caused by partial events, as assumed, higher primary energies would reduce the plateau height.

slope	0° sim	30° sim	60° sim	90° sim	20 keV 30°	15 keV 30°
global [σ/pg]	1.92e-7	2.18e-7	3.92e-7	1.06e-6	5.2e-7	1.95e-7
L_α [σ/pg]	1.12e-7	1.35e-7	2.53e-7	6.39e-7	4.01e-7	1.46e-7

Figure 6.20 – Slopes of the fitted data, experimental and simulated as shown in figure 6.19. The upper row takes both fluorescence regions, L_α and L_β, into account. The lower one only L_α. These values can be used in eq. 3.14 to extrapolate detectable gold masses per incident photon number.

Then the first in chip-photon interaction would occur in a higher depth which reduces the probability of partial events. This can explain why the 20 keV measurement is more sensitive than the 15 keV equivalents even with a lower cross section for fluorescence production. Anyway it is difficult to draw conclusions from one single data point. Finally the limit of detection needs to be estimated. Assuming the limit to be $3\,\sigma$, the minimal effective time necessary is calculated from the linear fits above with $t_{eff} = \frac{9}{m^2 A^2}$. As such limits depend on the number of effective incident photons, which takes the detector dead time into account. These limits are shown in figure 6.17. For $1e3$ pg gold, $2e8$ 15 keV photons are required to achieve Z= $3\,\sigma$. 10 pg are detectable with more than 2e12 effective photons and for 0.1 g more than 2e16 are needed, which is equivalent to an duration of exposure of 6666 s, less than 2 h, applying an incident flux of 3e12 ph/s. Under experimental conditions $3\,\sigma$ is difficult to detect if background fit functions are not clear, which mostly is the case.

7 High Energy Multi-mode - Multi chromatic XFI

7.0.1 Introduction

Multi chromatic modalities in medical imaging are of interest to enhance image quality or to use more than one tracer simultaneously [166][167][168]. Likewise a multi chromatic approach was taken here for XFI. While fluorescence intrinsically shows multi chromatic characteristics as many lines are emitted by one element, the term multi modal will be used here for the use of two or more tracer elements. Line ratios of a single element might help to estimate the fluorescence origin since high energy lines are less attenuated, as shown here [169], but no additional functional information can be obtained. Hence the term multi-mode, describing a simultaneous comparison of two or more tracers which could be coupled to different carriers with similar or varying destinations. The efficiency of targeted drug delivery or generally targeted processes thereby might become comparable in the same model *in vivo*. Here the multi modal approach was tested and limits were determined with four heavy elements and high incident energy with synchrotron radiation. Properties of the multi modal approach compared to single element imaging are analyzed in the following. Especially questions of sensitivity loss and false positive detections when using the multi modal approach are of interest.

7.1 Setup

This experiment took place at the P21 beamline which only allows for few discrete energies. An incident energy of 102.7 keV and a beam with 1x1 mm^2 cross section was chosen. Flux measurements were not feasible at that time since the beamline was newly set up and few

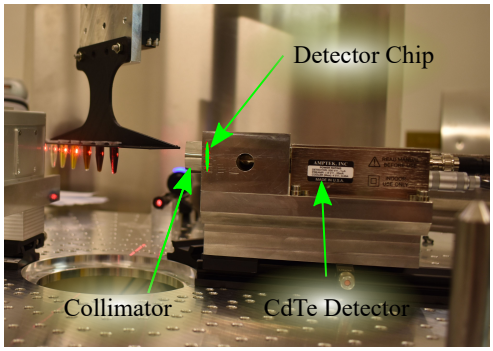

Figure 7.1 – Experimental setup, horizontal laser marking synchrotron beam height

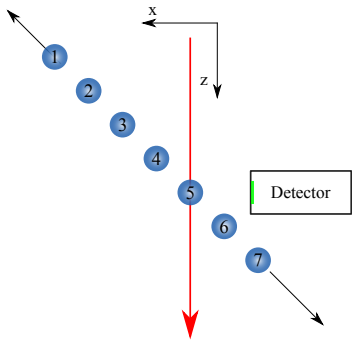

Figure 7.2 – Experimental sketch

El(Z)	$K_{\alpha 1}$ [eV]	$K_{\alpha 2}$ [eV]	$K_{\beta 1}$ [eV]	$K_{\beta 2}$ [eV]	$K_{\beta 3}$ [eV]
Pt(78)	66832 (100)	65112 (58)	75748 (23)	77850 (8)	75368 (12)
Ir(77)	64895.6 (100)	63286.7 (58)	73560.8 (23)	75575 (8)	73202.7 (12)
Au(79)	68803.7(100)	66989.5 (59)	77984 (23)	80150 (8)	77580 (12)
Bi(83)	77107.9 (100)	74814.8 (60)	87343 (23)	89830 (9)	86834 (12)

Figure 7.3 – Elements with the main K fluorescence line energies in eV and relative intensities. The strongest line intensity, $K_{\alpha 1}$, is normalized to 100. Data taken from the X-ray Data Booklet [113].

devices were installed later on. As such the flux needed to be estimated by fluorescence targets, here a 0.1 mm thick Au foil. Samples were prepared in small Eppendorf tubes, and arranged by a 3D printed mount in a row of 6 tubes in an angle of 45 deg° to the incident beam and detector. By that scanning most samples without changing the setup is possible. Each of the slots experiences a slightly different background behavior as positioning arms and step motors change. To compensate for that a zero measurement with a water filled Eppendorf tube in each slot was performed. Thereby each position can be corrected individually.

Heavy Metal Salty Solutions

This experiment was performed in cooperation with the group of Prof. Dr. Wolfgang Parak (Uni Hamburg). Sample preparation and post XFI ICP-MS analysis was done by members of his group, mostly Yang Liu. Elements of choice to be examined were platinum (Pt), gold

(Au), bismuth (Bi) and iridium (Ir).

The high energetic K-shell fluorescence, shown in table 7.3, as well as usability in medicine [170] were the reasons to chose these elements. Examined were Eppendorf tubes with different concentrations of above mentioned elements in form of salty solutions. Weight concentrations ranged from 0.019 mg/mL to 5 mg/mL, all listed in table 7.4. Further a probe set of mixtures containing all four elements was analyzed similarly to the individual samples. These probes are referred to in the following as T followed by the concentration of the corresponding probe. Here the concentration is the concentration of the individual element. T11 for instance contains 0.039 mg/mL gold, platinum, bismuth and iridium each. Such the gold peak height of a fluorescence peak in a T11 probe should be similar to the peak of the Au11 sample when cross section differences are corrected for. Deviations due to increased absorption in the T samples and overlapping peaks need to be taken into account.

sample No.	con mg/mL
10	0.019
11	0.039
12	0.079
13	0.16
14	0.31
16	1.25
17	2.5
18	5

Figure 7.4 – Elemental concentrations used in salt solutions

Nano Particle Loaded HeLa Cells

Additionally HeLa cells [171](diameter 20 um) were exposed to Pt and Au nano particle, 100 nm in diameter, solutions of 100 ug/mL, 25 ug/mL and 10 ug/mL, for 48 h. Probes with exposed concentration and particle cell uptake found by ICP-MS are listed in table 7.6. Harvested cells were formed to a compact cell pellet by centrifugation and placed in Eppendorf tubes on agarose to fixate it at medium height as shown if figure 7.5. After fixation the cells are dead. Consisting mainly of water, cells are not compressible thus a single cell volume is V_{Cell}=4.19e-9 cm^3. At cell height Eppendorf tubes show an outer diameter of 0.6 cm and an inner diameter of 0.54 cm. Assuming the beam to hit the probe centrally the active beam-cell-pellet intersection includes a volume of 5.4e-3 cm^3. A close packing of equal

Figure 7.5 – Eppendorf tube containing agarose (transparent bottom part) and HeLa cell pellet (milky middle part) with a height of 3 to 5 mm. Foto by Yang Liu.

Probe No.	X2	X3	X4	X8	X9	X10	X16	X17	X22
Con [ug/mL]	100	100	100	25	25	25	10	10	0
Loading	Pt	Au	Pt+Au	Pt	Au	Pt+Au	Pt	Au	-
Au [pg/Cell]	0	40.67	50.4	0	6.44	4.4	0	1.62	<2e-6
Pt [pg/Cell]	118.98	0	122.57	18.34	0	15.9	6.58	0	<2e-6

Figure 7.6 – HeLa cell probes with corresponding specific nano particle loading and post XFI mass uptake determined by ICP-MS analysis.

spheres would yield a $9.5e5$ irradiated cells. Lacking cell walls and rigid structure the approach of close packing shows a lower limit of cells expected in the beam volume. If no free space was left by cells, the number expected is $1.29e6$ cells in the beam-cell-pellet intersection volume. This is the cell number that was assumed to be irradiated. Later elemental cell uptake estimations use this number.

7.2 Flux Estimation

For flux estimations, the beamline, since newly set up, could provide only rough estimates of the incident flux. Therefore fluorescence targets were used to estimate it, as described in section 3.5.1. Absorber variations with two different CdTe Amptek detectors were performed, results are shown in figure 7.7. The incident flux was estimated thereby to $1.56\text{e}10\,\text{s}^{-1}$, the mean of the two individual measurements, which yielded $1.94\text{e}10\,\text{s}^{-1}$ and $1.18\text{e}10\,\text{s}^{-1}$. Relative uncertainty is estimated to 33 % which includes both individual measurements. This uncertainty will be dominating all further analysis of this experiment. The flux target was a 0.1 mm thick Au foil.

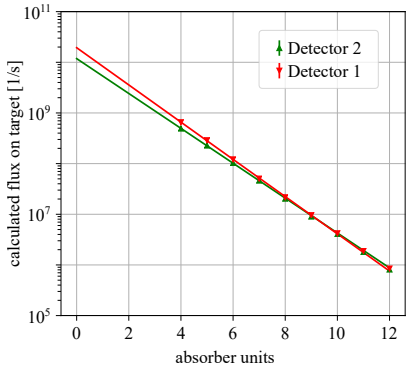

Figure 7.7 – Two absorber scans with two different Amptek CdTe detectors using a similar setup.

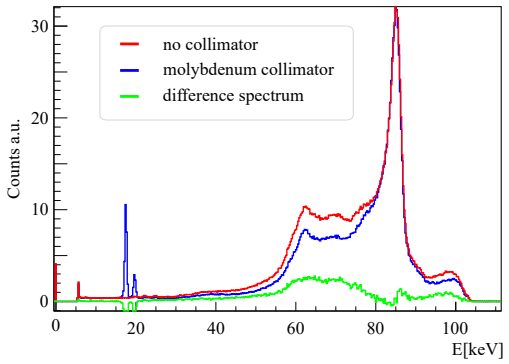

Figure 7.8 – Comparison of detected spectra using a molybdenum collimator (blue) or none (red).

7.3 Background, Background Subtraction and Collimator

7.3.1 Air Filter - Molybdenum Collimator

To reduce scattering from outside target objects a molybdenum collimator ring with wall thickness of 0.1 mm and diameter of 1.5 cm was positioned in front of the detector, shown in figure 7.1. This collimator extends 14 mm towards the probes. The collimator effect is displayed in figure 7.8, here spectra emerging from irradiated Eppendorf tubes are shown with collimation applied (blue) and without (red). The difference is shown in green. Collimation mainly effects higher Compton orders as expected.

7.3.2 Background Subtraction

Background subtraction is possible if a similar target without tracer is examined, the noise then is enhanced by a factor of $\sqrt{2}$. If background behavior in fluorescence energy region displays edges or kinks such subtraction might yield better results compared to speculative background fits. Here different slots were used for Eppendorf tube measurements, as shown in figure 7.2, slot one to seven. For each slot Eppendorf tubes filled with water were irradiated yielding spectra which later can be subtracted as background, these are shown in figure 7.9, a subtraction example is given in figure 7.10. Here a spectrum of an Au14

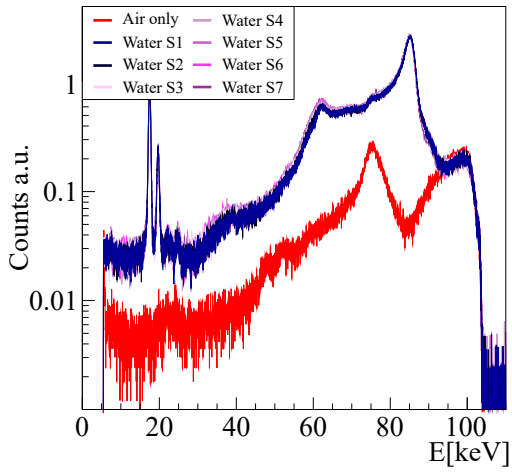

Figure 7.9 – CdTe Amptek background measurements, no target in beam (red) compared to water filled Eppendorf tubes at different positions, slot positions according to sketch 7.2.

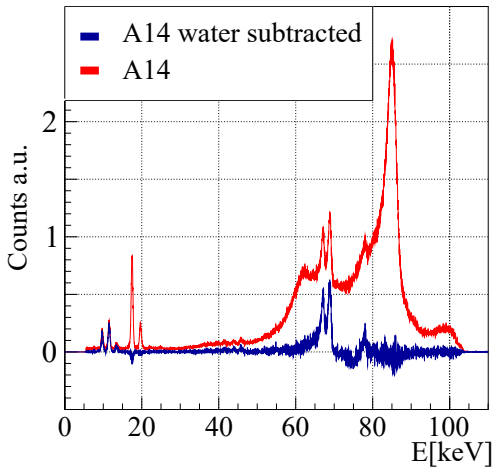

Figure 7.10 – Spectrum of gold loaded Eppendorf tube, red, and same spectrum with subtracted background.

measurement and the same spectrum with corresponding water spectrum subtracted is shown. Additionally a measurement without any object in the beam was performed, shown in figure 7.9 in red. Water spectra for different slots are mostly similar. Higher slot numbers seem to yield a bit higher number of multiple Compton photons in the range from 50 to 70 keV. Those differences might be explained by changes in motor and mount position influencing multiple Compton scattering which was aimed to be reduced by the collimator. All subtracted measured single element spectra are shown in figures 7.11 (Au), 7.12 (Ir), 7.13 (Bi) and 7.14 (Pt). Each figure has two panels of which the upper left one zooms to low concentration samples which yielded only minor peaks, logarithmic plots were not an option due to negative entries caused by spectral subtraction. Spectra from T probes, containing all four elements, are given in figure 7.15. Cell probe spectra containing gold are shown in figure 7.18, platinum in 7.16 and both in figure 7.17. All spectra are corrected as described in 3.4.2 to ensure comparability despite different experimental conditions as measurement time and numbers of applied absorber units.

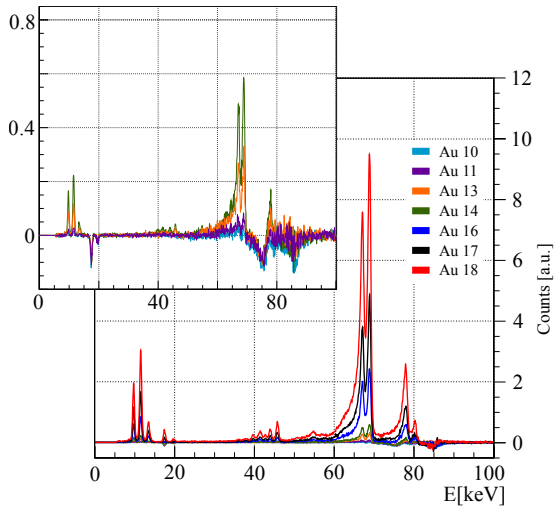

Figure 7.11 – Gold sample spectra with water measurements subtracted.

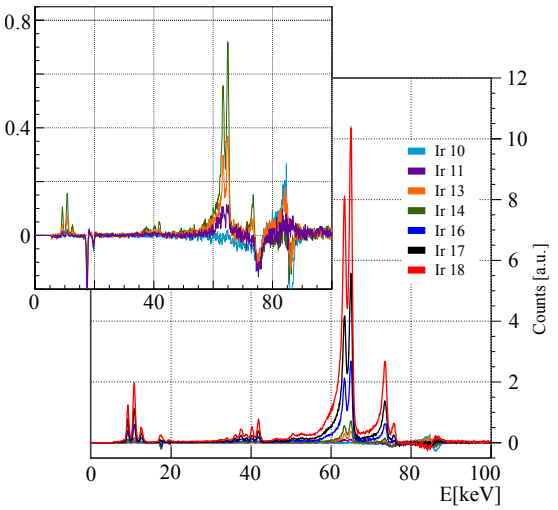

Figure 7.12 – Iridium sample spectra with water measurements subtracted.

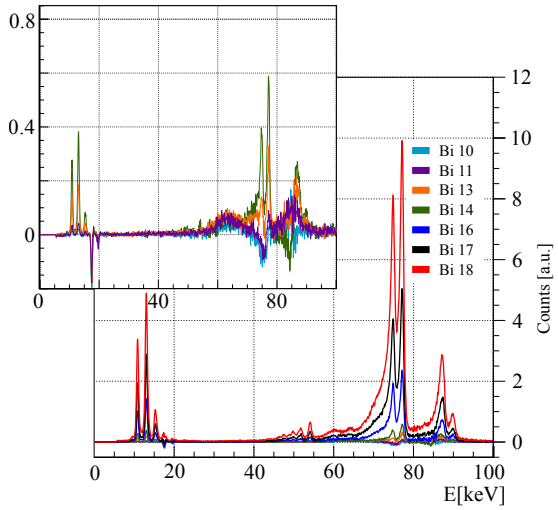

Figure 7.13 – Bismuth sample spectra with water measurements subtracted.

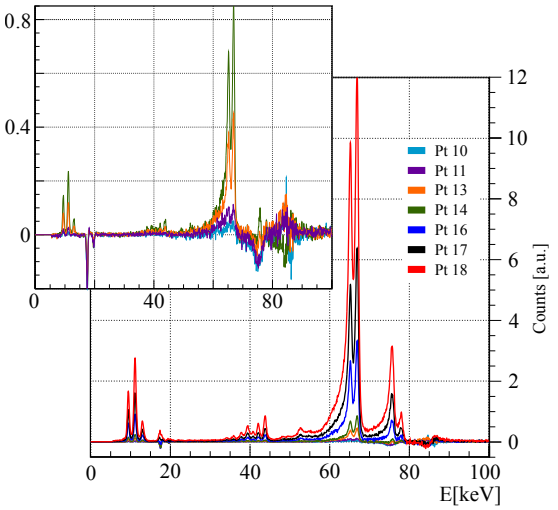

Figure 7.14 – Platinum sample spectra with water measurements subtracted.

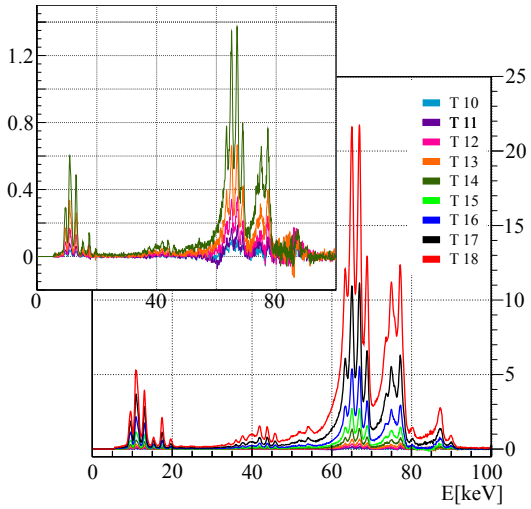

Figure 7.15 – Spectra of T probe sample with all four elements with water measurement subtracted.

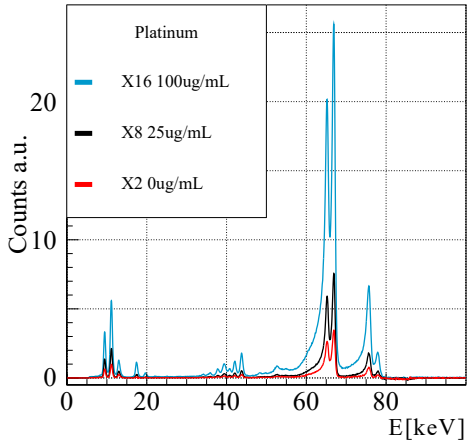

Figure 7.16 – Spectra of cells exposed to 100 nm Pt particles with water measurement subtracted.

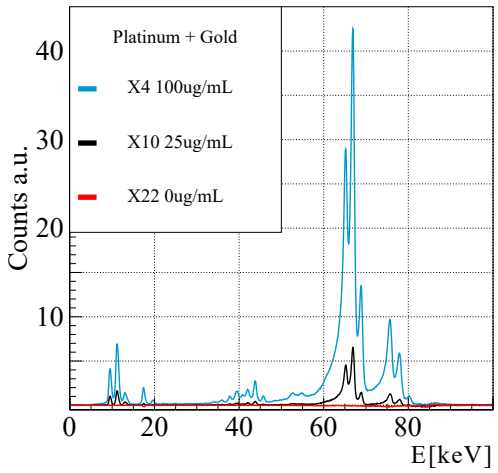

Figure 7.17 – Spectra of cells exposed to 100 nm Pt and Au (3:1) particles with water measurement subtracted.

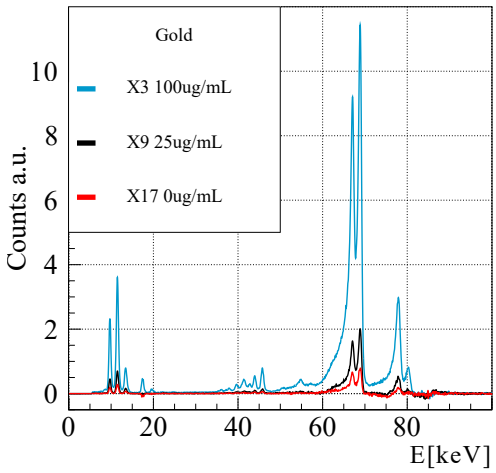

Figure 7.18 – Spectra of cells exposed to 100 nm Au particles with water measurement subtracted.

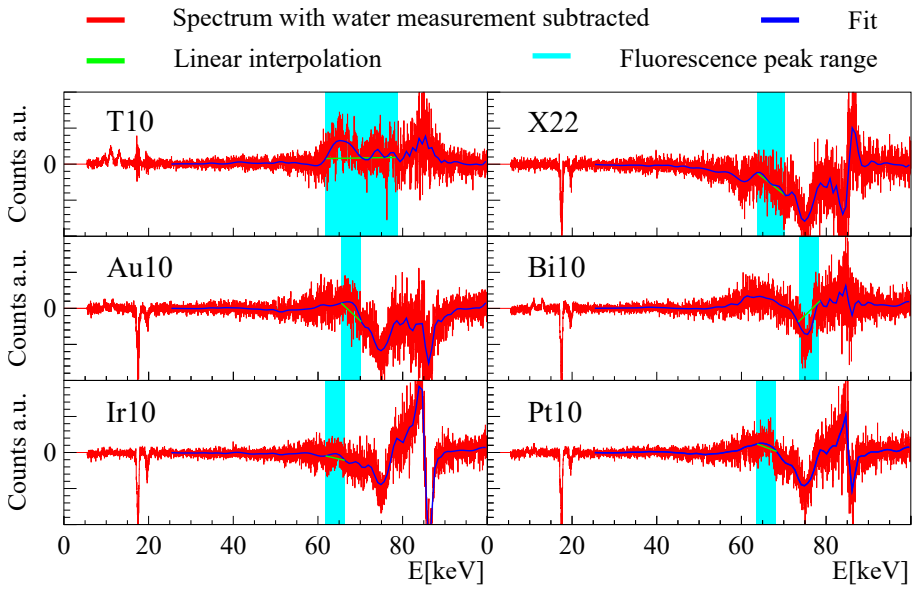

Figure 7.19 – Measurements of the smallest salt concentrations of each element, gold (Au), bismuth (Bi), iridium (Ir) and platinum (Pt) with water measurements subtracted (red), as described above. Ideally here shown spectra should display noise fluctuation around zero with small fluorescence peaks. This is not the case, deviations between 50 and 100 keV, especially in the fluorescence region, are visible. Spectra are fitted with multiple Gaussian functions (cyan) to derive an analytical form (blue). In fluorescence regions a linear interpolation of the two fit endpoints of that region is applied (green).

7.3.3 Lowest Concentration Samples - Deviations From Zero and Residuals

Spectra with water subtraction applied (figures 7.11 7.12 7.13, 7.14, 7.15, 7.16, 7.17, 7.18) ideally only show fluorescence lines and otherwise fluctuation around zero. This is not the case as lowest concentration spectra display in figure 7.19. Above 60 keV a bulge, a dip below zero from 70 to 80 keV and a bulge above 80 keV with a magnitude of 0.2 shows problems with subtraction of water measurements, especially at low elemental concentrations where such fluctuations outgrow fluorescence peaks. The features below 80 keV seem to be consistent in its quality throughout the single element probes. Positioning inconsistencies from probe to probe lead to small Compton peak fluctuations causing inconsistent fluctuations from probe to probe at the Compton peak maximum at 85 keV. For the later applied fits the energy region above 80 keV can mostly be ignored, as only bismuth K_β peaks occur in this region which are not necessary for later mass reconstruction, but the 60 to 80 keV

range is essential. Therefore for each probe type shown in figure 7.19 a residual function is determined by fitting the lowest concentration sample each with 40 Gaussian functions to derive the residual shape, shown in figure 7.19 in dark blue. This function will be used to correct all corresponding probe spectra. The fit in the relevant fluorescence line range is not used for later subtraction but this region is assumed to be described by a linear function between the fitted function values of $K_{\alpha 2}$-1 keV and $K_{\alpha 1}$+1 keV since fluorescence photons in the lowest concentration samples should not be subtracted. Anyway the residual spectra seem to display only very small or no fluorescence lines.

7.4 Fits and Mass Reconstruction

Tailing behavior needs to be addressed in more detail here as CdTe detectors in this energy range are prone to hole tailing. In high concentration samples five lines per element need to be fitted, three K_β and two K_α lines. Each line contributes to entries below its energy in the spectra through hole tailing. Therefore overestimating fluorescence lines on tails needs to be avoided. Therefore fit functions described in 3.4.1 were slightly modified. The peak fit function P(x) can be separated in three parts:

$$P(x) = G(x) + D(x) + H(x) \tag{7.1}$$

The main gauss peak G(x), a tail D(x) shaped by an exponential function multiplied by two error functions, marking its right end at the center of the Gaussian peak and its low energy end at 89.5% main peaks energy, and a minor plateau H(x) reaching from the peak down into low energy regions. This plateau of a mono energetic peak should be three magnitudes less intense than its main peak, compare [69, p. 19]. This is not the case here, as the plateau is mainly not caused by detector effects, but in target Compton scattering. Therefore H(x) is more prominent than expected by pure detector effects, its lower cut off is defined by the maximum scattering energy loss of a fluorescence photon, which is 180° scattering. The fit is defined as follows, similar to the definition in 3.4.1 with mentioned

modifications:

$$G(x) = \exp\left(-\frac{(x-E_p)^2}{2(\sigma)^2}\right) \tag{7.2}$$

$$D(x) = C\ \exp\left(\frac{x-E_p}{\beta}\right)\frac{1}{2}\,\mathrm{erfc}\left(\frac{x-E_p}{\sqrt{2}\sigma}+\frac{\sigma}{\sqrt{2}\beta}\right)\frac{1}{2}\mathrm{erfc}\left(-\frac{x-0.895\,E_P}{\sqrt{2}\sigma}\right) \tag{7.3}$$

$$H(x) = D\ \mathrm{erfc}\left(\frac{x-\frac{1}{1/E_p+2/(m_e c^2)}}{\sqrt{2}\sigma}\right)\frac{1}{2}\mathrm{erfc}\left(\frac{x-E_p}{\sqrt{2}\sigma}\right) \tag{7.4}$$

Per element k, five peaks were fitted, each obtaining the relative intensity a_p from the X-ray Data Booklet [113]. Absolute elemental abundance scales with I_k. Free parameters left then are: C, D and β. E_p and $\sigma = 250 \pm 50\,eV$ are determined by element and detector. As only a narrow energetic range is covered by the K-shell fluorescence of iridium, platinum and gold, D, C and β are assumed to be similar for all those peaks. The values found by fitting highest concentration samples are: $\beta = 2105 \pm 10\,\mathrm{eV}$, D=4e-3±0.5e-3 and C=$0.5 \pm 0.05$. The bismuth peaks showed slightly different behavior, β here was set to $\beta = 2705 \pm 10\,\mathrm{eV}$. This might be caused by the higher mean energies of bismuth lines and thus different detector response or in background falsely corrected by the procedure described in section 7.3.3. There higher energies are prone to high background variability due to Compton peak influence. Fit parameters were found by fitting highest concentrations spectra of the four element probes Au18, Pt18, Ir18 and Bi18.
Additional background B(x) is minor but estimated to be constant throughout the fit range: B(x) =B. This value B is an average of 30 bin entries below the plateau end of the lowest energy peak in the spectrum. The total fit function F(x) then is given as:

$$F(x) = B + \sum_{k=0}^{k_{max}} I_k \left(\sum_{p=1}^{5} a_p P_p(x)\right). \tag{7.5}$$

Fits from highest to lowest concentration samples are shown in figure 7.20. These spectra are not normalized by time or absorber units. Towards lower concentrations noise seems to rise which is caused by elongated measurement time t, given in the upper right corner of each panel. Below time the number of applied absorber units is given. χ^2 values are not given as some energy ranges, especially the range between the K_α and K_β lines, are not perfectly described by the fit in high concentration samples, which is visible especially in the platinum and the iridium case in figure 7.20. Despite that the K_α lines, which will later be used for mass reconstruction, are fitted well.

Salt probe spectra containing only one element were fitted only with the corresponding element. In T probes all four elements were fitted and the cell probe spectra were always

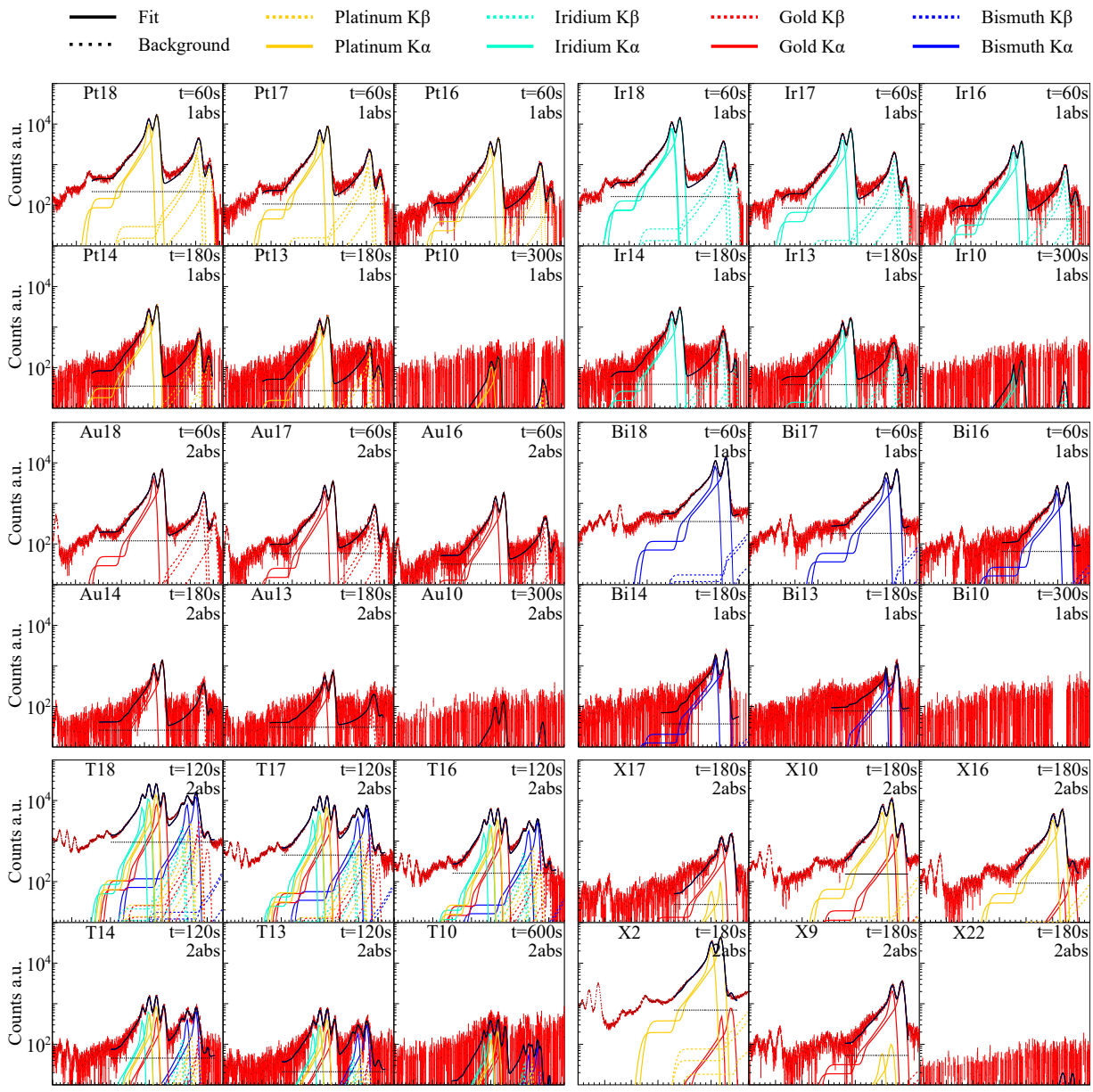

Figure 7.20 – Fits of the water subtracted spectra from highest to lowest concentrations for all examined probe types. These figures are given to give an impression of the fits, their flaws and the signal vanishing in noise as concentrations decline. The measurement time t is increasing as the concentration decreases and some measurements were taken with different numbers of absorber units changing the on target flux.

fitted with the possibility of both elements, gold and platinum, being present. But not all cell probes contained both elements. The noisy spectra and the high energy background above the K_α peaks often lead to false positive detection of one element in the cell probes. The mass reconstruction was performed according to section 3.5.2 with I_0 determined as shown in 7.2. Cell uptake estimations use the number of cells in beam-probe intersection volume described in 7.1.
Only K_α lines were used for mass reconstruction to avoid problems caused by imprecision of the high energy K_β lines mentioned above. Elemental cross sections were taken from the X-ray Data Booklet [113]. Significances are calculated in a 3σ interval. Signal counts C_S are integrated from fits, in the limits from $E_p - 3\sigma$ to $E_p + 3\sigma$, with the signal peak energy E_p. Background counts are derived from the original spectra without water subtraction. All counts in the same 3σ energy region are integrated, signal counts then are subtracted. Therefore all other fluorescence lines are considered as background in the $\pm 3\sigma$ interval.

7.5 Results

Three different kinds of probes were examined, first: the simple salt solutions with only on element present in diluted form. Second: the T probe samples which contained all four salts with comparable concentrations each. And third: cell probes prepared with Au and Pt nano particles. The gold to platinum ratio per probe highly fluctuated from probe to probe.

7.5.1 XFI Mass Reconstruction Compared to ICP-MS

To validate the applied mass reconstruction method and the XFI method in general, results in this chapter are compared to ICP-MS results. Sample analysis by ICP-MS was performed after the XFI procedure. Both analysis methods used the same sample. Hence XFI and ICP-MS results can be compared here, shown in figure 7.21(single salt solutions), 7.22 (T probes) and 7.23(Cell probes)

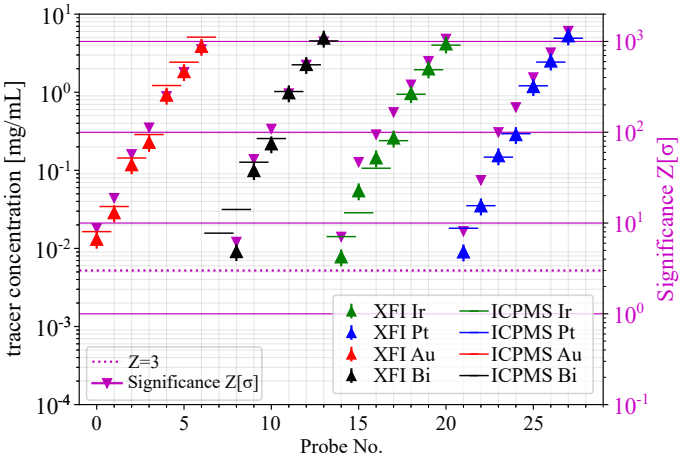

Figure 7.21 – Reconstructed tracer concentration of salt probes each containing only one tracer element. XFI values are compared to ICP-MS results. Significances of the $K_{\alpha 1}$ signals are given on the right axis in magenta.

Single Salt Probe Concentration Reconstruction

The reconstructed masses of single element salt probes are shown in figure 7.21 for the element gold, probes 0 to 6 (red), bismuth 7 to 13 (black), iridium from probe No. 14 to 20 (green) and platinum from 21 to 27 (blue). Reconstructed concentrations are shown in [mg/mL] on the left y-Axis, the according $K_{\alpha 1}$ significance in the right axis. Significance related markers and lines are shown in magenta. Concentration error bars are mostly due to the flux uncertainty described in 7.2. In general gold shows less concentration compared to ICP-MS and other tracers. Here the ICP-MS values are above or close to the upper uncertainty limit of the XFI values even for highest tracer concentration. XFI reconstructed values of bismuth, platinum and iridium on the other hand match the ICP-MS values in the high concentration samples. With decreasing concentration XFI values deviate more. The two lowest concentrations, which are wrong by more than on error bar margin, are unreliably in this measurement as noise overgrows the signals, visible in figure 7.20. The second lowest platinum sample is here the exception. The lowest bismuth concentration sample did not detect any signal, which probably is caused by the different background situation of bismuth compared to the other elements, see figure 7.19 and section 7.3.3.

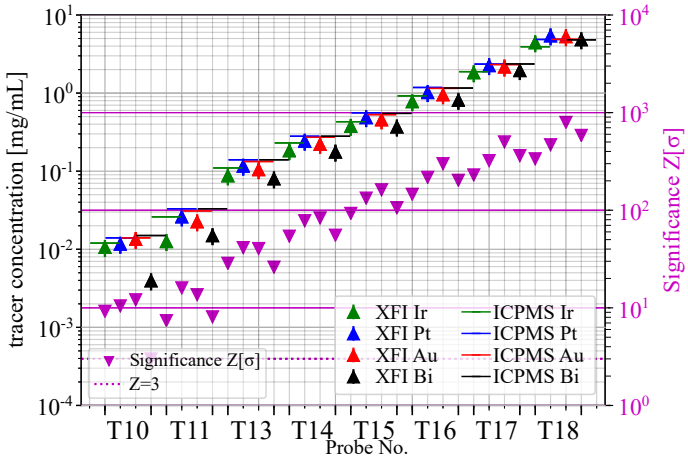

Figure 7.22 – Reconstructed tracer concentration of T probes containing all four tracer elements, Ir, Pt, Au and Bi. Results are compared to the ICP-MS results. Significance of the $K_{\alpha 1}$ peaks are given on the right axis.

T Probe Concentration Reconstruction

A similar behavior can be observed in reconstructed masses of T probes shown in figure 7.22. Probes are listed here from lowest to highest concentration from left (T10) to right (T18). Significance values of the individual $K_{\alpha 1}$ peaks are given on the right y-axis in magenta, elemental concentrations on the left axis in [mg/mL]. Expect for the two highest concentration probes, XFI reconstructed concentrations are lower compared to the ICP-MS evaluation. While XFI iridium, platinum and gold concentration measurements overlap with ICP-MS values in the margin of uncertainty, XFI bismuth concentrations are constantly measured to low, except for the highest concentration sample. Bismuth $K_{\alpha 1}$ and $K_{\alpha 2}$ lines share an energy region with the nine K_{β} lines of the other three elements, as shown in figure 7.20. This and an overestimation of the constant background in this high energy region might cause the underestimation of the bismuth concentrations. These samples offered similar concentrations of each element in one probe, which allows for a mostly constant fit shape which can be scaled to fit the individual concentrations.
This also leads to differences in the significances of individual elements, as fluorescence lines, especially the K_{α} lines of iridium, platinum and gold, do overlap. Shared energy regions can be estimated by table 7.3 and seen in figure 7.20, bottom left. The iridium $K_{\alpha 2}$ and gold $K_{\alpha 1}$ lines are not overshadowed by another fluorescence line. Others are: gold

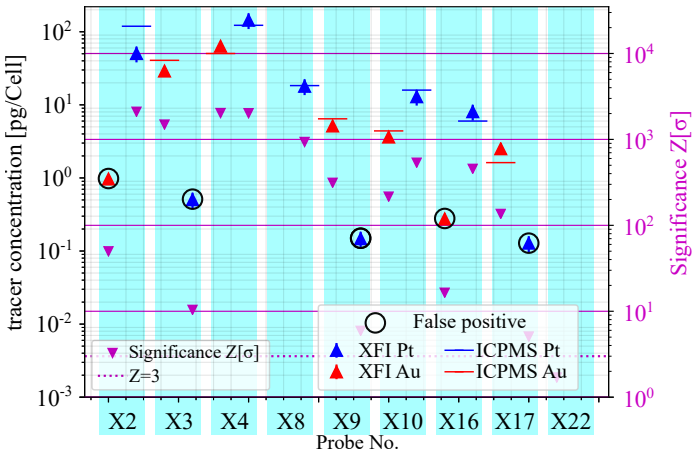

Figure 7.23 – Cellular tracer mass uptake estimated with XFI compared to ICP-MS measurements. Mass per cell is displayed on the left y-axis in pg/cell, the $K_{\alpha 1}$ signal significance on the right one in σ. Each cell probe was analyzed for platinum and gold, one probe is shown on one blue background. False positive detections are marked by a black circle.

$K_{\alpha 2}$ overlaps with platinum $K_{\alpha 1}$ and platinum $K_{\alpha 2}$ with iridium $K_{\alpha 1}$. Bismuth generally experiences K_{β} background from all three other elements. This is why gold $K_{\alpha 1}$ fluorescence performs best in terms of significance, in each probe gold yields the highest Z values, followed by platinum and bismuth with the lowest significance yielding iridium. The low iridium Z values might also be caused by a generally lower iridium concentration compared to the other metals.

Cell Probe Concentration Reconstruction

Concentrations of gold and platinum in the same cell probe differ more compared to internal concentration differences in T probes. Also only one of the two elements might be present, see table 7.6, still fluorescence lines of both elements were fitted, with the possibility of each element intensity to be zero. Therefore false positive peak detection might occur.
XFI reconstructed cellular elemental uptake is shown in pg/cell in figure 7.23 on the left y-axis, according K_{α} significance are displayed in magenta on the right y-axis. One individual cell probe is shaded blue, each showing one cellular uptake of gold (red) and one of platinum (blue). XFI measurements (triangles) are compared to ICP-MS results (horizontal lines). Probes displaying large deviations from ICP-MS values compared to XFI uptake uncertainty are: X2, X3 and X17. While XFI assumes larger gold concentration

in X17 than ICP-MS, the elemental uptake is underestimated in the probes X2, platinum, and X3, gold. Otherwise XFI and ICP-MS do match in the range of XFI uncertainty. Most probes containing only one element show false positives of the other, those are marked by black circles. These are: X2, X3, X9, X16 and X17. Those falsely assumed peaks are a magnitude or less in cellular uptake compared to the corresponding detected mass uptake which was present in the probe. This is caused by not ideal background description of the applied fit above the K_α fluorescence lines. The background there is higher than assumed, see figure 7.20, which leads to false positive peak detection.

7.5.2 Limits and Extrapolations

As the individual measurements were performed with different number of absorber units and measurement times, it is necessary to correct for those, therefore in the following all data of this chapter will be shown as described in 3.5.3. Thereby extrapolations of detectability and comparison to other experiments becomes possible.
The relation of significance Z over detected tracer mass M against the square root of effective number of photons $\sqrt{I_{eff}}$ is shown for all three probe types in figure 7.24. Salt probes results are shown on top, T probes in the middle and cell probes at the bottom. Significances of the $K_{\alpha 1}$ lines are used for the left panels, $K_{\alpha 2}$ for the right ones. Each element is shown, iridium in green, platinum in blue, gold in red and bismuth in black. The large uncertainties are caused by the flux uncertainty described in 7.2. A linear relation is fitted following $Z/M = A\sqrt{I_{eff}}$ for each element data set, a small rising slope A indicates less sensitivity, while a fast rising linear fit shows better sensitivity. Then less photons are needed to generate a detectable signal with 3σ applying the same tracer mass. In figure 7.24 each fit is shown with a filled uncertainty area marked by dotted lines. These lines are derived from fitting the extreme cases of the error bars. Slopes and uncertainties of each fit are given in table 7.25.

In general $K_{\alpha 2}$ shows less sensitive behavior compared to $K_{\alpha 1}$ lines. This is caused mostly by the difference in cross section. Salt probes, using elements individually, show the highest sensibility of all probes. Gold platinum and iridium show a similar performance, iridium and platinum are close to be indistinguishable in the $K_{\alpha 1}$ plot. Bismuth performs worse compared to the other metals.
In T probe samples lower energy fluorescence significance from iridium, platinum and gold suffer from other elements being present due to overlapping fluorescence lines. Compared to

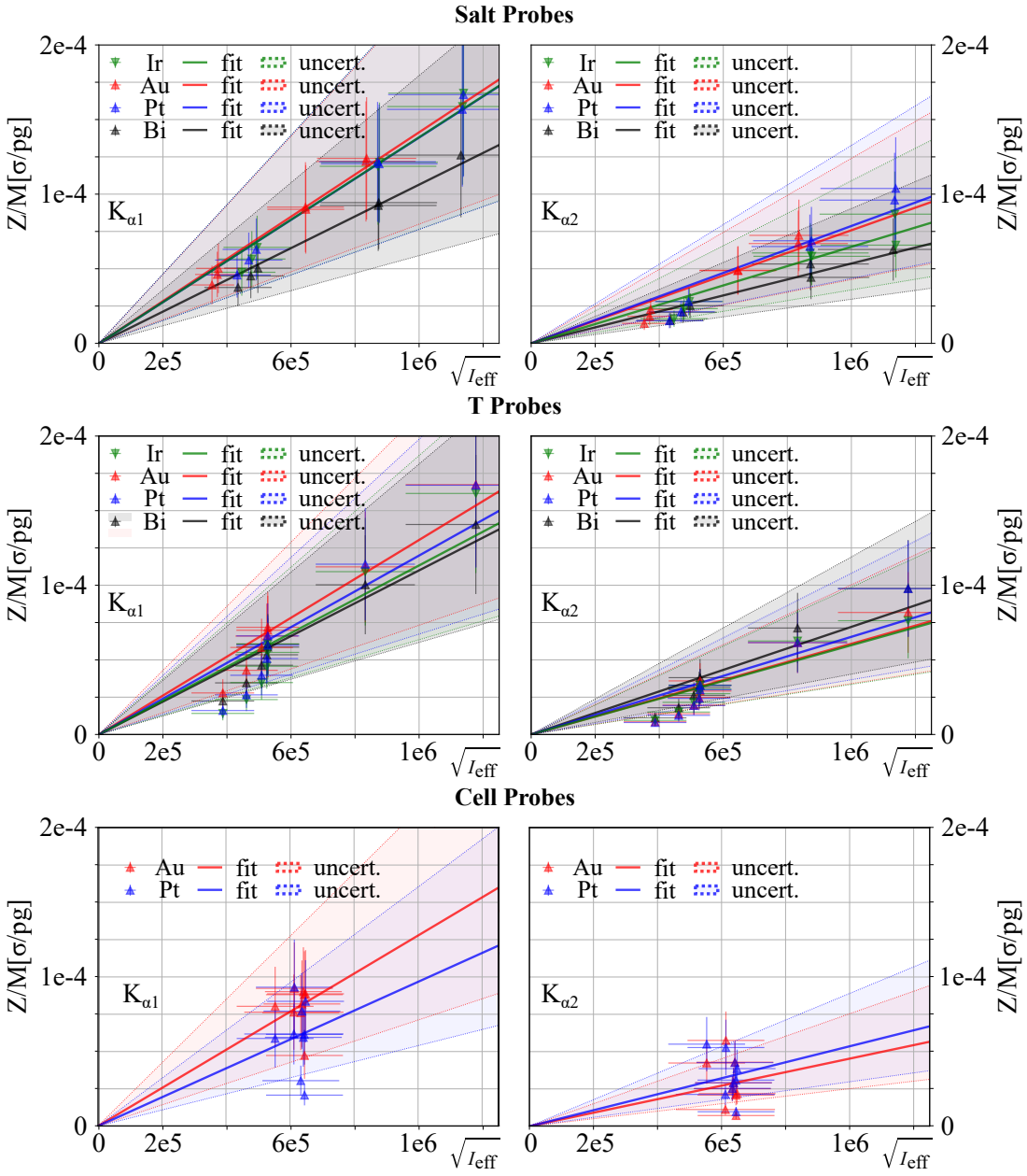

Figure 7.24 – Experimentally determined relations between in probe tracer mass M[pg], detected signal significance Z[σ] and $\sqrt{(I_{eff})}$, the effective number of photons the probe had been irradiated with. A linear relation is fitted for each data set. Error bars here are dominated by the incident flux uncertainty assumed in 7.2. Each linear fit is enclosed by a shaded area between the most extreme uncertainty cases. The $K_{\alpha 1}$ lines are outperforming $K_{\alpha 2}$ lines which is expected and due to cross section differences. Slopes of fits are given in table 7.25

single element salt probes their significance is slightly reduced. The gold $K_{\alpha 1}$ line performs best here as it experiences no direct overlap with other lines. But the fluorescence lines sensitivity approach the level of bismuth, in the $K_{\alpha 2}$ case bismuth shows a slight sensitivity advantage. The effect of overlapping is increasing with tracer concentration. Highest concentration T samples were measured with a short measurement time of t=120 s leading to a lower I_{eff}, while lowest concentration samples were measured for 600 s. The high concentration measurements do show systematically less sensitivity compared to the low concentration samples. The effect of overlapping fluorescence lines increases as the lines grow, especially since hole tailing is a significant effect here. Cell probe samples do perform comparable to the other probes but suffer from falsely positive fits, see 7.4, making these fits less predictable.

Element	Line	Salts [σ/pg]	T [σ/pg]	Cells [σ/pg]
Ir	$K_{\alpha 1}$	1.38e-10$\pm^{9.43e-11}_{6.16e-11}$	1.13e-10$\pm^{7.37e-11}_{4.98e-11}$	-
Ir	$K_{\alpha 2}$	6.47e-11$\pm^{4.42e-11}_{2.89e-11}$	5.98e-11$\pm^{3.89e-11}_{2.62e-11}$	-
Pt	$K_{\alpha 1}$	1.38e-10$\pm^{9.44e-11}_{6.16e-11}$	1.20e-10$\pm^{7.80e-11}_{5.26e-11}$	9.67e-11$\pm^{6.36e-11}_{4.28e-11}$
Pt	$K_{\alpha 2}$	7.87e-11$\pm^{5.40e-11}_{3.52e-11}$	6.54e-11$\pm^{4.26e-11}_{2.87e-11}$	5.36e-11$\pm^{3.54e-11}_{2.38e-11}$
Au	$K_{\alpha 1}$	1.41e-10$\pm^{8.98e-11}_{6.16e-11}$	1.30e-10$\pm^{8.44e-11}_{5.75e-11}$	1.28e-10$\pm^{8.43e-11}_{5.67e-11}$
Au	$K_{\alpha 2}$	7.58e-11$\pm^{4.82e-11}_{3.30e-11}$	6.08e-11$\pm^{3.95e-11}_{2.67e-11}$	4.53e-11$\pm^{3.01e-11}_{2.01e-11}$
Bi	$K_{\alpha 1}$	1.06e-10$\pm^{7.31e-11}_{4.76e-11}$	1.10e-10$\pm^{7.13e-11}_{4.83e-11}$	-
Bi	$K_{\alpha 2}$	5.35e-11$\pm^{3.68e-11}_{2.39e-11}$	7.21e-11$\pm^{4.69e-11}_{3.17e-11}$	-

Figure 7.25 – Fit slopes A in [σ/pg] for fits shown in figure 7.24. Values are distinct by probe type. For each element the $K_{\alpha 1}$ and $K_{\alpha 2}$ values are given.

7.5.3 Simulation Comparison

To estimate plausibility of the above shown results, GEANT4 simulations were performed for a single element tracer concentration of 0.5 mg/mL. Eppendorf tube, detector and molybdenum collimator were built in the simulation and irradiated with a photon beam with round cross section and a radius of 0.5 mm. Simulated were 100 runs with each 1e8 horizontally polarized photons with an energy of 102.7 keV.
A comparison of simulated and experimental spectra is given in figure 7.26 for each element, iridium in the upper left, platinum in the upper right, gold un the bottom left and bismuth in the bottom right. The general shape of the spectra does match, especially the energy

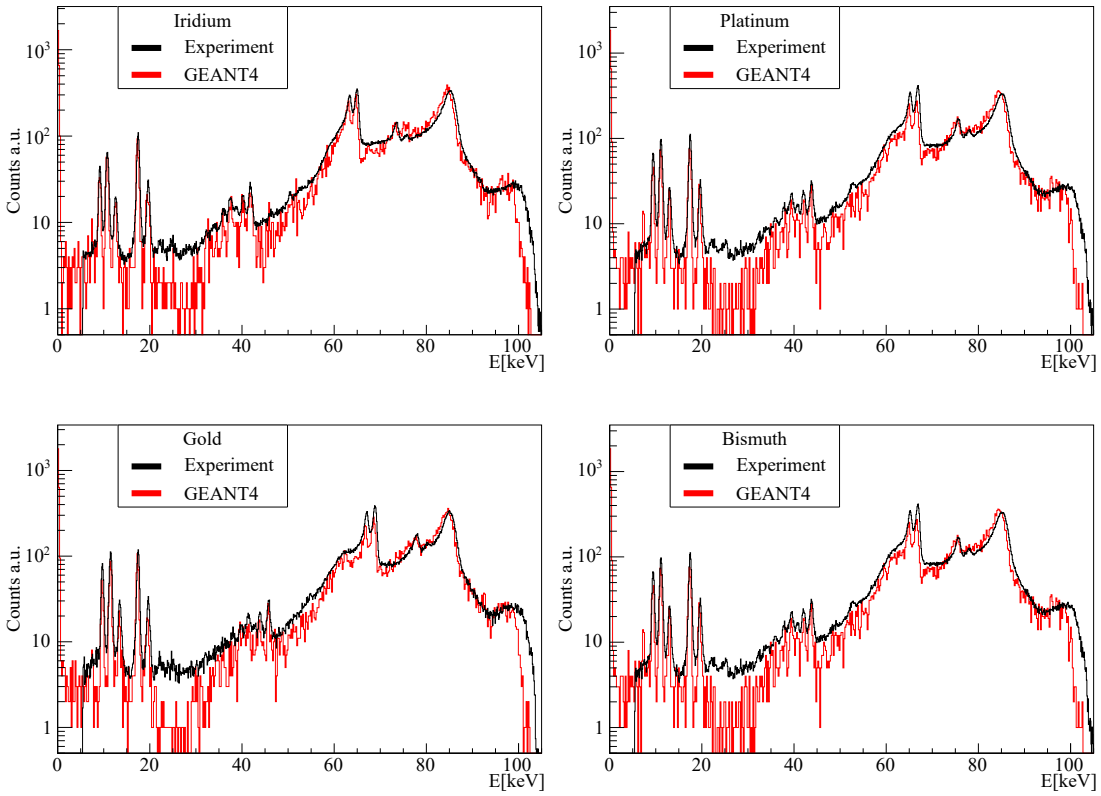

Figure 7.26 – Comparison of single element experimental spectra with GEANT4 simulation. Upper left shows iridium, upper right platinum, bottom left gold and bottom right bismuth. Simulations were performed with a tracer concentration 0.5 mg/mL, experimental salt target concentrations deviated. This causes the signal peaks to be different in height even though the general peak and spectral shape match. Further does the first order Compton peak deviate slightly which indicates small positioning uncertainties in the experiment. Slopes are given in table 7.28.

region of the first order Compton peak. It is notable that experimental spectra do seem to range to a higher energy compared to the simulations. A slight offset of the Compton peak can be explained by small misalignment of the Eppendorf tubes. The experimental concentration do deviate from 0.5 mg/mL which causes the fluorescence peaks to vary in hight. But still the shape of the tailing behavior is similar in experiment and simulation. At 40 keV the detector escape peaks are visible which are also matched by the simulation as well as the molybdenum fluorescence lines below 20 keV similar to the low energy L-shell tracer fluorescence lines close to 10 keV. A deviation from experiment is the decline in background above the K_α signals in the simulated spectra. This might be caused by missing experimental installations in the simulation. For example the experimental stage was

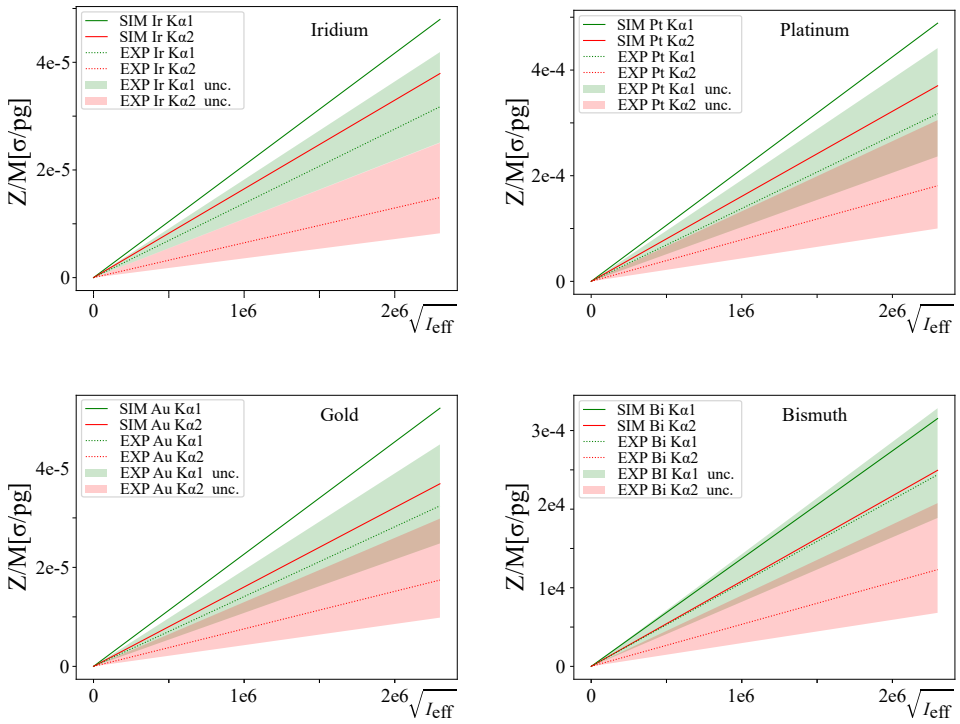

Figure 7.27 – Comparison of experimental and simulated sensitivities as shown in figure 7.24. Only single element salt probes are compared here. Simulated values are shown as continuous, experimental values as dotted lines. Uncertainties of experimental fits are given as shaded areas. In general simulations seem to indicate a higher sensitivity compared to the experiment.

not simulated as well as other Eppendorf tubes, shown in figure 7.2. Thereby additional environmental background might be missing in the simulations making them more sensitive.

Line	iridium a[σ/pg]	platinum a[σ/pg]	gold a[σ/pg]	bismuth a[σ/pg]
$K_{\alpha 1}$	2.09e-10	02.12e-10	2.27e-10	1.37e-10
$K_{\alpha 2}$	1.65e-10	1.61e-10	1.60e-10	1.08e-10

Figure 7.28 – Slope sensitivities of the simulated data given in figure 7.27.

The K_α peaks were evaluated similarly to the procedure above. The thereby retrieved slope sensitivity values are compared in figure 7.27 with experimental data and their uncertainties. As expected by spectra above, the simulated scenarios are more sensitive. All simulated values lie above and outside the experimental uncertainty, except for the bismuth $K_{\alpha 1}$ signal. Still the general values are comparable and the discrepancy can be explained by simplified simulations that miss out the general complexity of the experimental setup.Simulated sensitivity slope values are given in table 7.28.

8 Gadolinium Retention - Adaptable Spatial Resolution of XFI

Gadolinium based MRI contrast agents are widely used, but studies showed them to remain trapped in bone and brain tissue after treatment, linking those residuals to gadolinium retention diseases [19][20][172]. Here the probe of interest was a thigh bone of a rat treated with the MRI contrast agent Gadovist [173] in a study by the Bayer corporation, under supervision of Dr. Hubertus Pietsch. For the here shown experiment no additional animals were harmed, but a probe from previously performed studies was lend for testing the resolution capabilities of XFI.

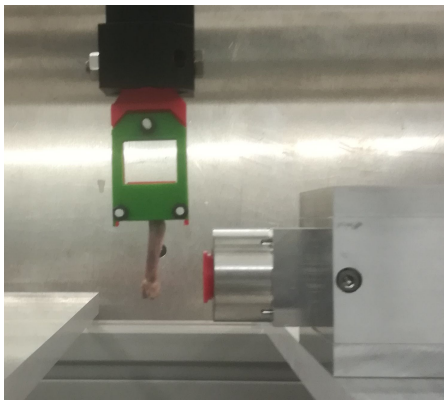

Figure 8.1 – Experimental setup with rat thigh bone in 3D printed mount and detector at the right.

This compound has the molecular formula $C_{18}H_{31}GdN_4O_9$, a molar mass of 604.25 g and a mass percent gadolinium of 26%. With the determination of in thigh bone gadolinium locality and quantity advantages of adaptable spacial resolution of synchrotron based XFI scanning are demonstrated in the following.

8.1 Setup

This experiment took place at the P07 at PETRA III. Finding gadolinium distributions in the rat thigh bone and quantitative estimations of the local concentration with XFI were

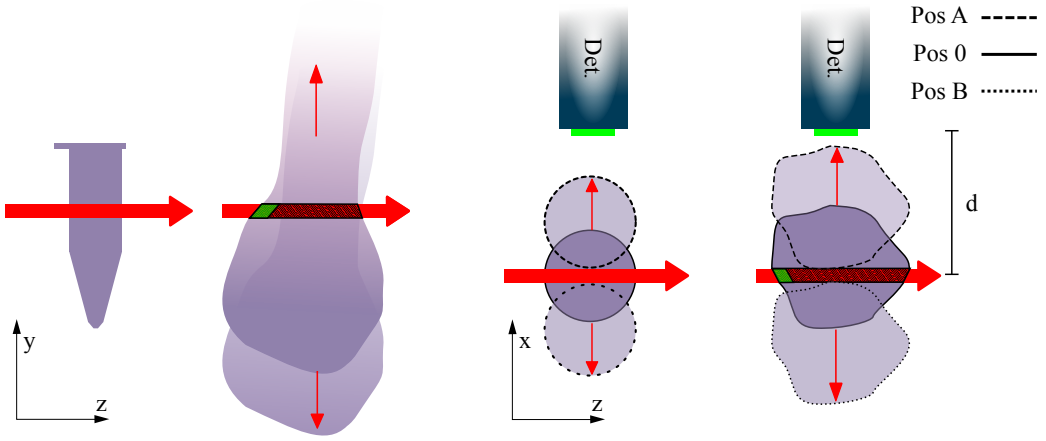

Figure 8.2 – Schematic visualization of detailed scan procedures. Left: x-y plane of Eppendorf tube (left) and bone (right) measurement. Bone movement along y axis was performed, tube movement not. Right: x-z plane movements were performed with bone and Eppendorf tubes. Each scanned from position A (closest to the detector, no beam intersection) to position B (farthest from detector, no beam intersection). Beam and detector position stayed fixed with a distance d.

the primary aim of this experiment. Beam cross sections are adjusted to allow for finer spatial resolution of high concentration areas.

An incident energy of 64.2 keV was chosen to avoid gadolinium K_α signals being superposed by Compton scattering of first or second degree without losing efficiency. Thereby fluorescence lines should be located below significant Compton background and above the CdTe detector escape peaks, compare figure 4.2. Photon flux was determined by beamline staff using a diode: $5.2e10 \pm 0.1e10 \frac{1}{s}$ for a 1x1mm^2 beam and $6.1e8 \pm 0.1e8\, 1/s$ for a 0.1x0.1mm^2 beam was measured. Small deviation of the factor 100 is expected as beam profile is not a box flat but flattened at fringes. For normalization purposes Eppendorf tubes with the relevant contrast agent in concentrations of: 3000 1000 300 and 0 µmol/L were used. Gadolinium, Z=64, emits the following fluorescence lines: $K_{\alpha 1}$ at 42.309 keV, relative intensity: 100, $K_{\alpha 2}$ at 42.996 keV, relative intensity: 56, and K_β at 48 keV if excited above the K edge of 50.239 keV [113].

With a 3D printed mount, the bone was fixated to two linear axis in the y-x plane enabling a movement perpendicular to the incident beam. Translation along beam direction z was not possible, compare figure 8.2 and figure 8.1. The Amptek XR-100T-CdTe detector was placed with chip at beam hight and at a distance from the beam of 3 cm for Eppendorf tube measurements and 2.8 cm for bone measurements. The tubes contained a volume of 1.5 ml

and were conical in their lower half. Tubes were irradiated at hight of constant diameter, being, including wall thickness, 10.5 mm, with an inner diameter of 9 mm.

Tubes with different concentrations were each scanned horizontally at one fixed y position with a 1x1 mm^2 beam at 10 different x positions, thereby the whole Eppendorf tube traverses the beam during one scan. The joint of the bone was scanned fully with a 1x1 mm^2 beam cross section with gadolinium hot spots scanned again with increased spatial resolution of 0.2x0.2 mm^2 and 0.1x0.1 mm^2. Measurement duration per pixel ranged between 150 and 200 seconds. Scans included the epiphysis with parts of the metaphysis. A line scan of the diaphysis, the middle bone part, was also performed.

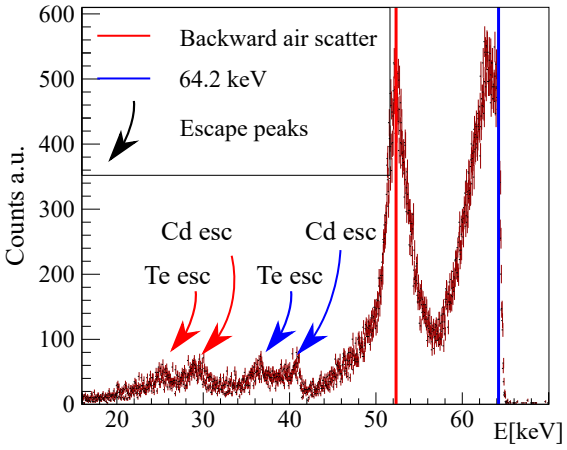

Figure 8.3 – Spectrum measured without probe. Air scatter peaks are visible, near incident energy 64.2 keV forward scattering and lower energy backward air scattering. Each peak creates escape events by chip material cadmium (Cd) and tellurium (Te) at lower energies.

8.1.1 Fit Function

To fit gadolinium signals the applied fit is divided in background function B(x) and signal function. The general signal magnitude A, relative peak intensities of $K_{\alpha 1}$ and $K_{\alpha 2}$ peaks, a_1 and a_2 and the peak shape function $P_P(x)$ describe the spectral shape in the signal region:

$$F(x) = B(x) + A\sum_{p=1}^{2} a_p P_p(x). \tag{8.1}$$

Fluorescence energy of 42 to 43 keV is significantly higher compared to L-shell gold fluorescence with 8 to 11.5 keV. This is why the Gaussian peaks here shows tailing behavior. Not as expressed as in heavy element K-shell fluorescence e.g. gold at 69 keV, but still hole tailing influences signal peak shape here. Therefore it is still not necessary to implement a full Hypermet function, as described in 3.4.1, but adding a tail towards lower energies is sufficient. Here the signals were fitted with the peak shape:

$$P(x) = \left[\exp\left(-\frac{(x-E_p)^2}{2\sigma_p^2}\right) + \exp\left(\frac{x-E_p}{\beta}\right)\frac{1}{2}\mathrm{erfc}\left(\frac{x-E_p}{\sqrt{2}\sigma_p} + \frac{\sigma_p}{\sqrt{2}\beta}\right)\right], \tag{8.2}$$

with the fluorescence line energy E_p, the detector resolution (RMS) σ and a free parameter β to model tailing behavior. Signal region background behaves mostly smoothly. The signal is located on the left flank of the Compton bulge which is fitted with a fourth degree polynomial and an exponential function. One further background feature is significant: escape events begin close below the gadolinium signal, clearly visible in an air spectrum, shown in figure 8.3. Here this step is not related to scatter events in the phantom but small angle scattering in the air in advance. Thus energy loss is marginal and this first air scattered Compton peak causes an escape plateau like feature below 41 keV. This is even more relevant in cases when the target is irradiated, as Rayleigh scattering increases detected events close to primary incident energy as displayed in figure 8.4. Then the forward air scatter peak vanishes and becomes a plateau like feature below 62 keV which is reflected in an escape plateau below 41 keV. This is modeled in the background fit B(x) by E(x):

$$B(x) = E(x) + \exp\left(e(x-38)\right) + \sum_{i=0}^{4} p_i (x-38)^i, \tag{8.3}$$

$$E(x) = \frac{h(x-38)}{\exp((x-41)/g) + 1}. \tag{8.4}$$

Besides the free parameter of the polynomial, e is describing the exponential function, h and g do characterize the escape plateau. These parameters are to be derived from fits. A fit example is given in figure 8.4, displaying the two K_α gadolinium lines with the background described above. From this spectrum data for the pixel (8 mm,6 mm) was derived in the following 2D bone color maps, e.g. figure 8.8.

Determination of signal viability with significance calculations as described in section 2.5.1 was conducted using both K_α peaks with the energy range for photon counting from $K_{\alpha 1}$-3σ to $K_{\alpha 2}$+3σ. With σ being the mean detector resolution of the fitted peaks.

8.1.2 Eppendorf Tube Normalization Probes

Eppendorf tube measurements with known gadolinium concentration (0, 300, 1000 and 3000 µmol/L) are utilized to determine unknown concentrations in bone material. Each tube was scanned horizontally with ten scan positions, such that the tube fully traverses the beam during one scan. The detector beam distance did not change as only the tube was moved. Each scan position offers different amount of material for photons to interact with, influencing not only fluorescence but also Compton scatter counts. Both count numbers are

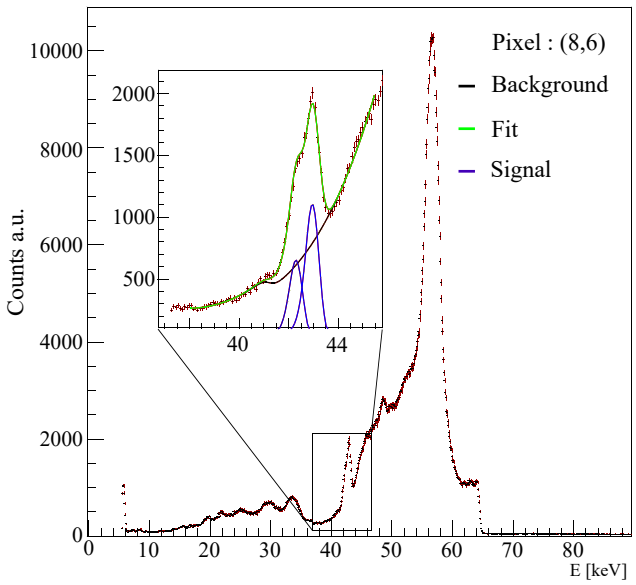

Figure 8.4 – Example bone spectrum with fit region zoomed in. Two gadolinium signal peaks P(x) shown in blue, background B(x). This spectrum equals data point (8 mm,6 mm) in following 2D maps.

additionally affected by the phantom material between detector and beam which changes during scanning and thereby influences in tube absorption, compare figure 8.2.

Absolute gadolinium counts detected are shown in figure 8.5 in the left panel for all scan positions of all four different concentrations. As the Eppendorf tubes are round in their profile, different gadolinium fluorescence count numbers are expected when scanning one tube. Marginal hits, irradiating mainly the hull will yield only few or no fluorescence at all. This can be seen at positions x=0, 1 or 7 and x=8 mm. Irradiating its center should yield the highest number of gadolinium fluorescence photons, here the positions x=3 to x=5. The tubes were placed by hand and thus small positioning uncertainties should be considered in the range of 1 mm. Nevertheless the gadolinium concentration should remain constant for all scan position of one tube.
Normalizing the total number of gadolinium fluorescence photon counts C_{Gd} per measurement by the number of detected photons in the whole spectrum C_T, with gadolinium fluorescence photons subtracted, returns a relative measure for the gadolinium concentration con_{Gd} in the irradiated material. Here a homogeneous density is assumed which is

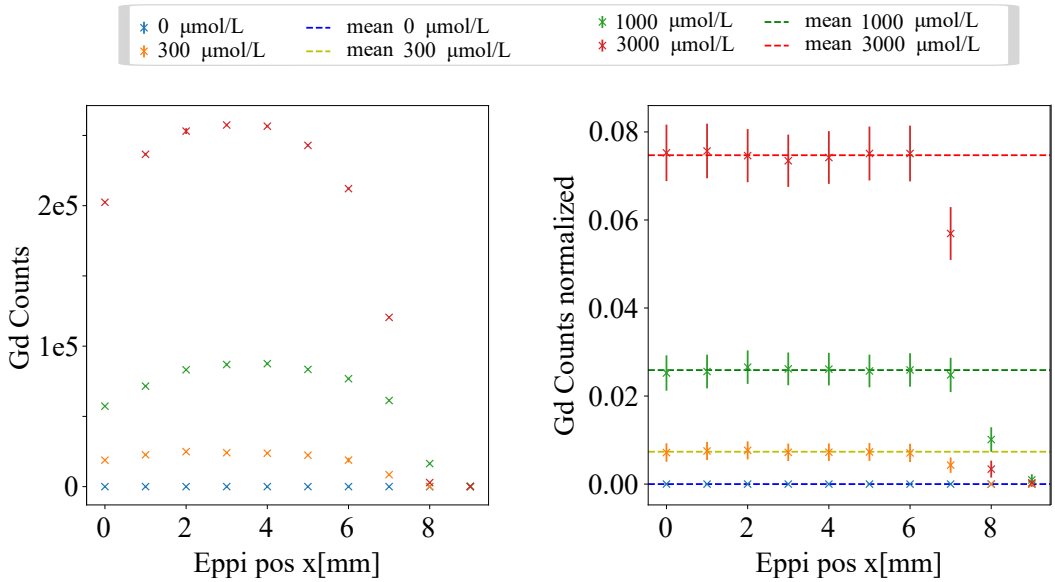

Figure 8.5 – Eppendorf tube measurements for all concentrations of 0, 300, 1000 and 3000 µmol/L. Scan positions along x are given on the x axis. In the left panel the total number of detected gadolinium fluorescence photons is shown. The right panel shows normalized gadolinium counts. They are normalized by the total number of counts in the detected spectrum with gadolinium fluorescence previously subtracted. Mean values are shown as dotted lines, measurements with X=7, 8 and 9 are excluded from mean value, as those did only partially irradiate the Eppendorf tube.

valid for the normalization probes. The concentration relates to the photon counts as:

$$C_{Gd}/(C_T - C_{Gd}) = a\,\mathrm{con}_{Gd}[\mu\mathrm{mol/L}], \tag{8.5}$$

with the proportional constant a. This normalization was performed on the Eppendorf tube scans and results are shown in figure 8.5, right panel. While the spherical cross section of the Eppendorf tubes was clearly visible in the left panel, indicating the total gadolinium mass irradiated, this is not the case in the right figure. Here the normalized gadolinium fluorescence counts are displayed for all scan positions, including the mean value for each concentration, these values are given in table 8.6. Measurements outside the Eppendorf tube, or only partial hits, like position x=7, 8 and 9 are excluded from the mean value which are given in table 8.6. With a linear fit a in equation 8.5 is determined to be a=2.5e-5.

	0 µmol/L	300 µmol/L	1000 µmol/L	3000 µmol/L
Mean	0	0.0073	0.026	0.075

Figure 8.6 – Mean values of normalized gadolinium fluorescence photon counts of all Eppendorf tube measurements shown in figure 8.5, right panel.

Bone densities range from 1 to 2 g/cm^3 for the following a mean density of 1.5 g/cm^3 was assumed, further was the bone material assumed to be homogeneous as well [174]. Thereby a concentration of 1µmol gadolinium per liter equates an in bone concentration of 0.105 µg gadolinium per g bone. With equation 8.5 then in bone gadolinium concentrations are reconstructed. Thereby the simplified assumption of photons behaving similarly in bone and water was made. This can be justified as the main uncertainty is the bone density in possible inhomogeneity therefore differences in interaction cross section are comparatively small.

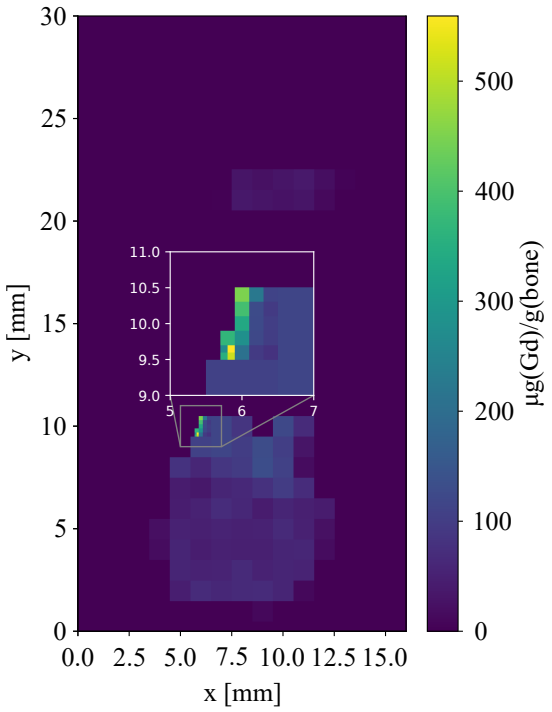

Figure 8.7 – Mean gadolinium concentration reconstructed with Eppendorf tube normalization. Areas with higher resolution are zoomed in.

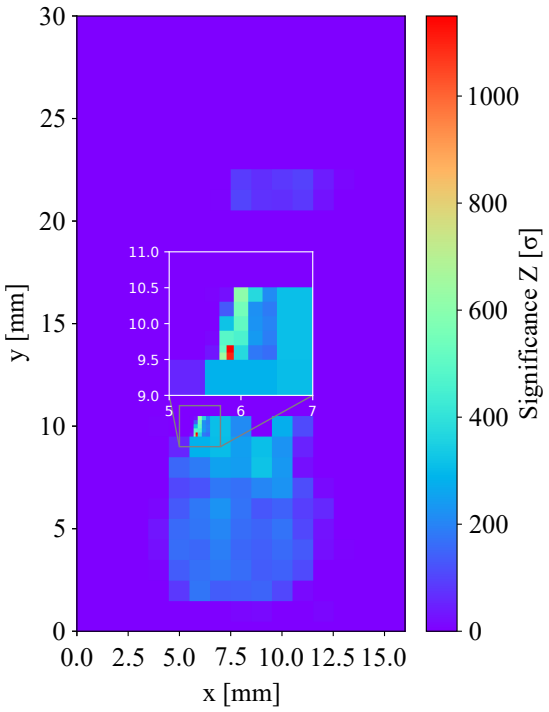

Figure 8.8 – Significance Z[σ] for each scanned position. Areas with higher resolution are zoomed in.

8.1.3 Results

The here following scan maps show the bone in the same coordinate system as in figure 8.2. Scanning the bone revealed an overall present gadolinium signal, shown in figure 8.8. In bone material significances generally ranged from 100 to 400 σ in the 1x1 mm^2 pixels with an increase in significance at a height of y=6 to y=10 mm. The 1x1 mm pixel (6,10) was investigated further with 0.2x0.2 mm^2 resolution. Which again partly yielded higher significances from 400 to 800 σ. Then again pixel (5.75, 9.55) was scanned with a 0.1x0.1 mm^2 resolution. Here two pixels yielded Z$>$1000 σ.

Significances do not directly translate in gadolinium concentrations as some pixel were irradiated for 150 s and others for 200 s. Further is the incident photon flux reduced, if the resolution is increased by shrinking the photon beam cross section. The mean gadolinium concentration per pixel is determined by normalization targets as shown above in section 8.1.2. The mean concentrations per g bone material range from below 100 µg to over 500 µg in the region with higher resolution. Strong local accumulation of gadolinium is shown here. The distribution of high concentration pixels hints that the gadolinium is mainly retained in the fringe layers of the bone material.

9 Conclusion

The here performed exploration of different application possibilities of synchrotron based XFI demonstrated not only sensitivity limits or suggests best parameter choices for experimental planing, but also demonstrated hurdles which need to be overcome. Not only experiments at different PETRA III beamlines were performed, but also an experimental stage, suiting the XFI requirements, usable at beamline end stations was designed and build.

The problems of underlying background were shown experimentally in chapter 6, which dealt with cellular uptake measurements of functionalized gold nano particles, and chapter 7, where the high energy multi mode approach was demonstrated. This background was either caused by elements in the probes themselves, as in the cell uptake experiment, or by significant Compton scattering as in the multi mode experiment. Probe contamination with other elements is mostly not avoidable but should as best as possible be controlled. For avoiding substantial Compton or detector related background, chapter 4 describes which incident energy and tracer choice is best to chose for phantom sizes of 1 mm to 1 cm. Best tracer choice for K shell fluorescence lies between Z=25 to Z=60 with moderate incident energy between 15 and 50 keV. This range is not bothered by Compton scattering nor by detector escape peaks, those become relevant if the incident energy is increased to above 60 keV. L-shell fluorescence on the other hand demands heaviest elements possible with incident energies at the corresponding edge. Neither Compton nor detector escape peaks do influence the measurement here significantly. Comparatively low energies allow the use of a Si detector without loss of efficiency.

Expected Compton background behavior was analyzed with GEANT4 simulations in chapter 5. Here Compton spectra emitted in 4π from irradiated water spheres are shown for energies between 20 and 100 keV and sphere radii of 1, 10 and 50 mm. The magnitude of background differences in angular positioning also is shown. These angular maps show where the lowest count rate from non fluorescence processes can be expected depending on phantom size and incident energy. Generally positioning the detector at 90° towards the

incident beam and in the polarization plane, is recommended. Still this positioning effect is most efficient in small sample sizes of 1 mm radius where the lowest count rate expected in 1e-4 4π per incident photon is below 1e-5 for 100 keV incident photons. A phantom with 50 mm radius yields 100 times more expected counts for otherwise similar parameters at the position of lowest expected count rate. Spectral background estimations for distinct detector positions ranging from θ=20° to 160° for positions relative to the incident beam polarization of 0, 45 an 90° were also given. This allows for phantom size adjusted tracer choice.

The experimental part showed two biologically relevant experiments and a further technical study of multi mode XFI and its impact on sensitivity of individual element detection.
At the P11 beamline a study with functionalized gold nano particle loaded PC3 cells demonstrated the high sensitivity of XFI using the gold L-shell and an incident energy of 15 keV. Here samples of only a few hundred irradiated cells yielded significant signals. Here a in $Z/M[\sigma/pg] = a\sqrt{I_{eff}}$ was experimentally determined to range between 1.46e-7 σ/pg to 1.95e-7 σ/pg. Under optimal detector positioning, which was not possible at that beamline, GEANT4 simulations showed a best value of a=1.06e-6σ/pg. The cellular gold uptake was determined to range between 0.3 and 0.4 pg for PSMAi+ and MUA functionalized nano particles and 1 to 1.5 pg for PSMAi+ without MUA. Irradiated number of cells were 311 and 622, the retrieved gold uptake was not influenced by cell sample size.
The heavy element K-shell experiment performed at the P21 beamline did investigate the simultaneous application of multiple tracer elements, this is called multi mode. Those elements were iridium, platinum, gold an bismuth. Probes were irradiated with 102.7 keV photons. Due to overlapping of fluorescence lines of iridium, platinum and gold, high concentration samples with all elements present are expected to show less sensitivity for the individual elements. Here a in $Z/M[\sigma/pg] = a\sqrt{I_{eff}}$ ranged for single element probes from 5.35e-11 σ/pg (bismuth $K_{\alpha 2}$) to 1.41e-11 σ/pg (gold, $K_{\alpha 1}$). In samples with all four elements simultaneously present, the fitted mean value of a did not drop drastically with a lowest value of 5.98e-11 σ/pg (iridium $K_{\alpha 2}$) to the highest 1.3e-11 σ/pg (gold, $K_{\alpha 1}$). Still samples with high concentrations performed consistently worse than the fitted mean. Multi modal analysis therefore can be seen as a viable option without significant loss of sensitivity, if tracer concentration are expected to be moderate, which was in this case below 0.16 mg/mL. The gold L-shell sensitivity found in the cell uptake study outgrows these numbers by magnitudes. This is caused by general higher L-shell cross section, smaller target size

and difference in Compton background.
The here reconstructed XFI masses of each tracer in the probe was compared to ICP-MS analysis performed after XFI measurement. It was shown that the with XFI reconstructed masses match the ICP-MS values in general, demonstrating this modality to be a viable option for element mass and concentration analysis in medium sized objects.
Imaging was demonstrated using the MRI contrast agent Gadovist, containing gadolinium, which was retained in a rat thigh bone. This target was scanned at the P07 beamline with beam diameters of 1x1 mm^2, 0.2x0.2 mm^2 and 0.1x0.1 mm^2 which demonstrated the advantage of adaptable spatial resolution of XFI. The found gadolinum concentrations ranged from low 10 to over 500 µg/g(Bone). With fine resolution the hot-spot-like gadolinium distribution on the outer bone layer was shown.

Here a the range of parameters of synchrotron based XFI was explored in three different experiments and supported by GEANT4 simulations and estimations. Low energy gold L-shell, medium energy gadolinium K-shell as well as high energy K-shell fluorescence of iridium, platinum, gold and bismuth was utilized and analyzed, covering an energy range from 9 to over 80 keV. It was shown to be sensitive enough to analyze biological questions on cellular levels without large sample sizes and to match reconstructed concentrations of conventional techniques as ICP-MS. Thereby making synchrotron based XFI a multi purpose tool allowing insight in otherwise opaque objects.

Glossary

CdTe	cadmium telluride
CdZnTe	cadmium zinc telluride
CT	computed tomography
DESY	deutsche elektronen-synchrotron
EPR	enhanced permeability and retention
FDA	food and drug administration
fMRI	functional magnetic resonance imaging
FWHM	full width half maximum
GaAs	gallium arsenide
GEANT4	geaometry and tracking 4
ICP-MS	inductively coupled plasma mass spectrometry
MRI	magnetic resonance imaging
MS	mass spectroscopy
NIST	national institute of standards and technology
NP	nano particle
PEGMUA	polyethyleneglycolmercaptoundecanoic
PET	positron emission tomography

PETRA III	positron-elektron-tandem-ring-anlage III
PIXE	particle-induced X-ray fluorescence
PSMAi	prostate specific membrane antigen inhibitor
RMS	root mean square
SNR	signal to noise ratio
SPECT	single photon emission computed tomography
XFI	X-ray fluorescence imaging
XRF	X-ray fluorescence spectroscopy

Bibliography

[1] Frank R Lichtenberg. The quality of medical care, behavioral risk factors, and longevity growth. Working Paper 15068, National Bureau of Economic Research, June 2009.

[2] J. J. Thomson M.A. F.R.S. Xl. cathode rays. *The London, Edinburgh, and Dublin Philosophical Magazine and Journal of Science*, 44(269):293–316, 1897.

[3] William Crookes. I. on the illumination of lines of molecular pressure, and the trajectory of molecules. *Proceedings of the Royal Society of London*, 28(190-195):102–111, 1879.

[4] W. C. Röntgen. Ueber eine neue art von strahlen. *Annalen der Physik*, 300(1):12–17, 1898.

[5] P.C. Seynaeve and J.I. Broos. The history of tomography. *Journal of the Belgian Society of Radiology*, 78(5):284 – 8, 1995.

[6] GN Hounsfield. Computerized transverse axial scanning (tomography). 1. description of system. *The British journal of radiology*, 46(552):1016–1022, December 1973.

[7] Stephen Gardner, Joshua Kim, and Indrin Chetty. Modern radiation therapy planning and delivery. *Hematology/Oncology Clinics of North America*, 33, 10 2019.

[8] Dale Miles. Cone beam ct: Applications for the cosmetic dentist. *Journal of Cosmetic Dentistry*, Cone Beam CT: Applications for the Cosmetic Dentist:110–118, 07 2013.

[9] Peter Dawson. Functional imaging in ct. *European Journal of Radiology*, 60(3):331 – 340, 2006. Contrast Media and Modern Imaging.

[10] Edwin J.R. van Beek and Eric A. Hoffman. Functional imaging: Ct and mri. *Clinics in Chest Medicine*, 29(1):195 – 216, 2008. Contemporary Chest Imaging.

[11] OECD (2019) Computed tomography (CT) exams (indicator). doi: 10.1787/3c994537 en, (Accessed on 24 September 2019).

[12] Raymond Damadian. Tumor detection by nuclear magnetic resonance. *Science*, 171(3976):1151–1153, 1971.

[13] P. C. Lauterbur. Image Formation by Induced Local Interactions: Examples Employing Nuclear Magnetic Resonance. *Nature*, 242:190–191, March 1973.

[14] Robert R. Edelman. The history of mr imaging as seen through the pages of radiology. *Radiology*, 273(2S):S181–S200, 2014. PMID: 25340436.

[15] F. Bloch, W. W. Hansen, and Martin Packard. Nuclear induction. *Phys. Rev.*, 69:127–127, Feb 1946.

[16] P.C. Lauterbur, D.M.H. Mendonca, and A.M. Rudin. Augmentation of tissue water proton spin-lattice relaxation rates by in vivo addition of paramagnetic ions. *Frontiers of Biological Energetics*, 1978.

[17] Leyla Loued-Khenissi, Olivia DÃČÂűll, and Kerstin Preuschoff. An overview of functional magnetic resonance imaging techniques for organizational research. *Organizational Research Methods*, 22:109442811880263, 09 2018.

[18] Yu-Dong Xiao, Ramchandra Paudel, Jun Liu, Ma Cong, Zi-Shu Zhang, and Shun-Ke Zhou. Mri contrast agents: Classification and application (review). *International Journal of Molecular Medicine*, 38, 09 2016.

[19] Joel Garcia, Stephen Liu, and Angelique Louie. Biological effects of mri contrast agents: gadolinium retention, potential mechanisms and a role for phosphorus. *Philosophical Transactions of The Royal Society A Mathematical Physical and Engineering Sciences*, 375:20170180, 11 2017.

[20] Mariane Le Fur and Peter Caravan. The biological fate of gadolinium-based mri contrast agents: a call to action for bioinorganic chemists. *Metallomics*, 11, 11 2018.

[21] Magnetic resonance imaging (MRI) exams (indicator). doi: 10.1787/1d89353f-en OECD (2019), (Accessed on 24 September 2019).

[22] Henry N. Wagner. A brief history of positron emission tomography (pet). *Seminars in Nuclear Medicine*, 28(3):213 – 220, 1998. The Coming Age of Pet (Part 1).

[23] William Blahd. Benedict cassen the father of body organ imaging. *Cancer biotherapy & radiopharmaceuticals*, 15:423–9, 11 2000.

[24] Leah H. Portnow, David E. Vaillancourt, and Michael S. Okun. The history of cerebral pet scanning. *Neurology*, 80(10):952–956, 2013.

[25] Christine Tang and Vincenzo Militano. *PET Tracers for Brain Imaging*, pages 15–21. 01 2019.

[26] T Hara. 18f-fluorocholine: a new oncologic pet tracer. *Journal of nuclear medicine : official publication, Society of Nuclear Medicine*, 42:1815–7, 01 2002.

[27] David Schlyer. Pet tracers and radiochemistry. *Annals of the Academy of Medicine, Singapore*, 33:146–54, 04 2004.

[28] Jamal Zweit. *Medium Half-Life Inorganic Radionuclides for Pet Imaging*, pages 47–61. 01 1996.

[29] Paul McQuade, Deborah W. McCarthy, and Michael J. Welch. *Metal Radionuclides for PET Imaging*, pages 237–250. Springer London, London, 2005.

[30] William Moses. Fundamental limits of spatial resolution in pet. *Nuclear instruments & methods in physics research. Section A, Accelerators, spectrometers, detectors and associated equipment*, 648 Supplement 1:S236–S240, 08 2011.

[31] Izumi Umeda, Kotaro Tani, Keisuke Tsuda, Masamitsu Kobayashi, Mayumi Ogata, Sadaaki Kimura, Mitsuyoshi Yoshimoto, Shuji Kojima, Kunikazu Moribe, Keiji Yamamoto, Noriyuki Moriyama, and Hirofumi Fujii. High resolution spect imaging for visualization of intratumoral heterogeneity using a spect/ct scanner dedicated for small animal imaging. *Annals of nuclear medicine*, 26:67–76, 01 2012.

[32] Jai P. Agrawal, Bradley James Erickson, and Charles E. Kahn. Imaging informatics: 25 years of progress. *Yearbook of medical informatics*, Suppl 1:S23–31, 2016.

[33] Alan Alexander, Megan McGill, Anna Tarasova, Cara Ferreira, and Delphine Zurkiya. Scanning the future of medical imaging. *Journal of the American College of Radiology*, 16(4, Part A):501 – 507, 2019.

[34] Life expectancy at birth (indicator). doi: 10.1787/27e0fc9d-en OECD (2019), OECD (2019), (Accessed on 30 September 2019).

[35] George A. Mensah, Gregory A. Roth, and Valentin Fuster. The global burden of cardiovascular diseases and risk factors. *Journal of the American College of Cardiology*, 74(20):2529–2532, 2019.

[36] Freddie Bray, Jacques Ferlay, Isabelle Soerjomataram, Rebecca Siegel, Lindsey Torre, and Ahmedin Jemal. Global cancer statistics 2018: Globocan estimates of incidence and mortality worldwide for 36 cancers in 185 countries: Global cancer statistics 2018. *CA: A Cancer Journal for Clinicians*, 68, 09 2018.

[37] Hannah Weir, Trevor Thompson, Ashwini Soman, Bjorn Moller, Steven Leadbetter, and Mary White. Meeting the healthy people 2020 objectives to reduce cancer mortality. *Preventing chronic disease*, 12:E104, 07 2015.

[38] Deaths from cancer (indicator). doi: 10.1787/8ea65c4b-en OECD (2019), (Accessed on 24 September 2019).

[39] Vincent T. DeVita and Edward Chu. A history of cancer chemotherapy. *Cancer Research*, 68(21):8643–8653, 2008.

[40] Jared Robbins, John Longo, and Michael Straza. *Radiation Therapy*, pages 461–479. 01 2020.

[41] Paula Asprino, Fabiana Bettoni, and Fernanda Koyama. The era of individualized medicine in cancer. *Journal of Cancer Clinical Trials*, 1, 10 2015.

[42] Heerak Chugh, Damini Sood, Ishita Chandra, Vartika Tomar, Gagan Dhawan, and Ramesh Chandra. Role of gold and silver nanoparticles in cancer nano-medicine. *Artificial Cells, Nanomedicine, and Biotechnology*, 46:1–11, 03 2018.

[43] Shannon Westin and Robert Coleman. Individualized medicine in ovarian cancer: Are we there yet? *Gynecologic Oncology*, 144:229–231, 02 2017.

[44] Selvan Ravindran, Jitendra Suthar, Rutuja Rokade, Pooja Deshpande, Pooja Singh, Ashutosh Pratinidhi, Rajeshree Kambadkar, and Srushti Utekar. Pharmacokinetics, metabolism, distribution and permeability of nanomedicine. *Current Drug Metabolism*, 19, 03 2018.

[45] C Lee Ventola. The nanomedicine revolution: part 1: emerging concepts. *P & T : a peer-reviewed journal for formulary management*, 37(9):512–525, September 2012.

[46] Young Hee Choi and Hyo-Kyung Han. Nanomedicines: current status and future perspectives in aspect of drug delivery and pharmacokinetics. *Journal of Pharmaceutical Investigation*, 48(1):43–60, Jan 2018.

[47] C Ventola. The nanomedicine revolution: Part 2: Current and future clinical applications. *P & T : a peer-reviewed journal for formulary management*, 37:582–91, 10 2012.

[48] Xueping Xie, Jinfeng Liao, Xiaoru Shao, Qianshun Li, and Yunfeng Lin. The effect of shape on cellular uptake of gold nanoparticles in the forms of stars, rods, and triangles. *Scientific Reports*, 7, 06 2017.

[49] Yosuke Koyama, Yasuto Matsui, Yoko Shimada, and Minoru Yoneda. Biodistribution of gold nanoparticles in mice and investigation of their possible translocation by nerve uptake around the alveolus. *The Journal of toxicological sciences*, 40:243–9, 03 2015.

[50] Takuya Ishizaka, Kazuya Nagano, Ikkei Tasaki, Hong Tao, Jian-Qing Gao, Kazuo Harada, Kazumasa Hirata, Shigeru Saito, Hirofumi Tsujino, Kazuma Higashisaka, and Yasuo Tsutsumi. Optimization and evaluation of pretreatment method for sp-icp-ms to reveal the distribution of silver nanoparticles in the body. *Nanoscale Research Letters*, 14, 12 2019.

[51] Desam Reddy, Abdul Jabbar Al-Rajab, and Ramachandra Reddy Gowkanapalli. *Biomedical and Pharmaceutical Applications of Inductively Coupled Plasma-Mass Spectrometry (ICP-MS)*. 09 2018.

[52] ICPMS. `https://www.thermofisher.com/de/de/home/industrial/environmental/environmental-learning-center/contaminant-analysis-information/metal-analysis/comparison-icp-oes-icp-ms-trace-element-analysis.html`, viewed 23 Sep 2019.

[53] Ling-Han Jia, Yi Li, and Yu-Zhen Li. Determination of wholesome elements and heavy metals in safflower (carthamus tinctorius l.) from xinjiang and henan by icp-ms/icp-aes. *Journal of Pharmaceutical Analysis*, 1(2):100 – 103, 2011.

[54] Valderi L Dressler, Dirce Pozebon, and Adilson J Curtius. Determination of heavy metals by inductively coupled plasma mass spectrometry after on-line separation and

preconcentration. *Spectrochimica Acta Part B: Atomic Spectroscopy*, 53(11):1527 – 1539, 1998.

[55] Jacob Weinrich Arianne Bazilio. The easy guide to: Inductively coupled plasma-mass spectrometry (icp-ms). Technical report, umass, 2012.

[56] John Watson. Fast, simple method of powder pellet preparation for xray fluorescence analysis. *X-ray Spectrometry - X-RAY SPECTROM*, 25:173–174, 01 1996.

[57] A. Finkelshtein and V. Afonin. Analytical approximation for calculating secondary fluorescence in xray fluorescence analysis of powdered materials. *X-ray Spectrometry - X-RAY SPECTROM*, 25:210–214, 09 1996.

[58] Harris L. Byers, Lindsay J. McHenry, and Timothy J. Grundl. Xrf techniques to quantify heavy metals in vegetables at low detection limits. *Food Chemistry: X*, 1:100001, 2019.

[59] Ahmed N. Kadachi and Mohammad A. Al-Eshaikh. Limits of detection in xrf spectroscopy. *X-Ray Spectrometry*, 41(5):350–354, 2012.

[60] J. Knoth and H. Schwenke. A new totally reflecting x-ray fluorescence spectrometer with detection limits below 10Ã¢ÂĹÂŠ11 g. *Fresenius' Zeitschrift für analytische Chemie*, 301(1):7–9, Jan 1980.

[61] R Glocker and H. Schreiber. Quantitative röntgenspektralanalyse mit kalterregung des spektrums. *Annalen der Physik 85, 1089-1102, (1928)*, 1928.

[62] H.G.J. Moseley M.A. Xciii. the high-frequency spectra of the elements. *The London, Edinburgh, and Dublin Philosophical Magazine and Journal of Science*, 26(156):1024–1034, 1913.

[63] Ishii. Pixe and its applications to elemental analysis. *Quantum Beam Science*, 3:12, 06 2019.

[64] Mattsson S. and Börjesson J. X-ray fluorescence in medicine. *Spectroscopy Europe 20(3):13-17*, 2008.

[65] Christopher L. Gordon, Colin E. Webber, and David R. Chettle. The reproducibility of 109cd-based x-ray fluorescence measurements of bone lead. *Environmental Health Perspectives*, 102:690 – 694, 1994.

[66] T.G. Dzubay, B.V. Jarrett, and J.M. Jaklevic. Background reduction in x-ray fluorescence spectra using polarization. *Nuclear Instruments and Methods*, 115(1):297 – 299, 1974.

[67] J.D. Ryon, R.W.; Zahrt. Improved x-ray fluorescence capabilities by excitation with high intensity polarized x-rays. *Adv. X-Ray Analysis 22 453-60*, 1978.

[68] Peter M. Kopittke, Tracy Punshon, David J. Paterson, Ryan V. Tappero, Peng Wang, F. Pax C. Blamey, Antony van der Ent, and Enzo Lombi. Synchrotron-based x-ray fluorescence microscopy as a technique for imaging of elements in plants. *Plant Physiology*, 178(2):507–523, 2018.

[69] Florian Blumendorf. *Background Reduction for XFI with Human-Sized Phantoms.* PhD thesis, UniversitaÌĹt Hamburg, 2019.

[70] Prinessa Chellan and Peter Sadler. The elements of life and medicines. *Philosophical Transactions of The Royal Society A Mathematical Physical and Engineering Sciences*, 373, 03 2015.

[71] Jimmy Börjesson and Sören Mattsson. Medical applications of x-ray fluorescence for trace element research. *Powder Diffraction - POWDER DIFFR*, 22, 06 2007.

[72] J. Börjesson and S. Mattsson. Toxicology; in vivo x-ray fluorescence for the assessment of heavy metal concentrations in man. *Applied Radiation and Isotopes*, 46(6):571 – 576, 1995.

[73] Jimmy Börjesson, Tom Bellander, L Järup, C G Elinder, and Sören Mattsson. In vivo analysis of cadmium in battery workers versus measurements of blood, urine, and workplace air. *Occupational and environmental medicine*, 54:424–31, 07 1997.

[74] J.M. O'Meara, Jimmy Börjesson, David Chettle, and F.E. McNeill. Optimization of an in vivo x-ray fluorescence mercury measurement system. *Nuclear Instruments and Methods in Physics Research Section B: Beam Interactions with Materials and Atoms*, 213:560–563, 01 2004.

[75] Michelle Lord, F McNeill, J.L. Gräfe, Michael Noseworthy, and David Chettle. A phantom-based feasibility study for detection of gadolinium in bone in-vivo using x-ray fluorescence. *Applied Radiation and Isotopes*, 112, 03 2016.

[76] Michelle Lord, F.E. McNeill, J.L. Gräfe, A.L. Galusha, P.J. Parsons, Michael Noseworthy, L. Howard, and David Chettle. Confirming improved detection of gadolinium in bone using in vivo xrf. *Applied Radiation and Isotopes*, 120, 12 2016.

[77] M. Pushie, Ingrid Pickering, Malgorzata Korbas, Mark Hackett, and Graham George. Elemental and chemically specific x-ray fluorescence imaging of biological systems. *Chemical reviews*, 114, 08 2014.

[78] Run Zhang, Li Li, Yasmina Sultanbawa, and Zhi Xu. X-ray fluorescence imaging of metals and metalloids in biological systems. *American journal of nuclear medicine and molecular imaging*, 8:169–188, 06 2018.

[79] Chad Thompson, Jeffrey Wolf, Reem Elbekai, Madhav Paranjpe, Jennifer Seiter, Mark Chappell, Ryan Tappero, Mina Suh, Deborah Proctor, Anne Bichteler, Laurie Haws, and Mark Harris. Duodenal crypt health following exposure to cr(vi): Micronucleus scoring, Îş-h2ax immunostaining, and synchrotron x-ray fluorescence microscopy. *Mutation Research/Genetic Toxicology and Environmental Mutagenesis*, 117, 05 2015.

[80] Siyuan Zhang, Liang Li, Jiayou Chen, Zhiqiang Chen, Wenli Zhang, and Hongbing Lu. Quantitative imaging of gd nanoparticles in mice using benchtop cone-beam x-ray fluorescence computed tomography system. *International Journal of Molecular Sciences*, 20:2315, 05 2019.

[81] Nivedh Manohar, Francisco Reynoso, Parmeswaran Diagaradjane, Sunil Krishnan, and Sang Cho. Quantitative imaging of gold nanoparticle distribution in a tumor-bearing mouse using benchtop x-ray fluorescence computed tomography. *Scientific Reports*, 6:22079, 02 2016.

[82] Liang Li, Siyuan Zhang, Ruizhe Li, and Zhiqiang Chen. Full-field fan-beam x-ray fluorescence computed tomography with a conventional x-ray tube and photon-counting detectors for fast nanoparticle bioimaging. *Optical Engineering*, 56:043106, 04 2017.

[83] S. Zhang, L. Li, Z. Chen, W. Zhang, and H. Lu. In-vivo imaging of gadolinium nanoparticles using benchtop xfct system. In *2018 IEEE Nuclear Science Symposium and Medical Imaging Conference Proceedings (NSS/MIC)*, pages 1–3, Nov 2018.

[84] Michael Faraday Esq. D.C.L. F.R.S. Lix. experimental relations of gold (and other metals) to light.the bakerian lecture. *The London, Edinburgh, and Dublin Philosophical Magazine and Journal of Science*, 14(96):512–539, 1857.

[85] Samer Bayda, Muhammad Adeel, Tiziano Tuccinardi, Marco Cordani, and Flavio Rizzolio. The history of nanoscience and nanotechnology: From chemicalâĂŞphysical applications to nanomedicine. *Molecules*, 25:112, 01 2020.

[86] Marek Grzelczak, Jorge Pérez-Juste, Paul Mulvaney, and Luis Liz-Marzán. Shape control in gold nanoparticle synthesis. *Chemical Society reviews*, 37:1783–91, 10 2008.

[87] F. Pacheco-Torgal, S. Miraldo, Y. Ding, and J.A. Labrincha. 3 - nanoparticles for high performance concrete (hpc). In F. Pacheco-Torgal, M.V. Diamanti, A. Nazari, and C-G. Granqvist, editors, *Nanotechnology in Eco-Efficient Construction*, Woodhead Publishing Series in Civil and Structural Engineering, pages 38 – 52. Woodhead Publishing, 2013.

[88] Ralph Sperling, Pilar Rivera Gil, Feng Zhang, Marco Zanella, and Wolfgang Parak. Biological applications of gold nanoparticles. chem soc rev 37:1896. *Chemical Society reviews*, 37:1896–908, 10 2008.

[89] Syed A. A. Rizvi and Ayman M. Saleh. Applications of nanoparticle systems in drug delivery technology. *Saudi pharmaceutical journal : SPJ : the official publication of the Saudi Pharmaceutical Society*, 26(1):64–70, January 2018.

[90] Nandish Pathak, Pratim Pathak, and Shivam Upadhyay. Nanoparticles and target drug delivery for cancer treatment: A comprehensive review. *International Journal of Drug Regulatory Affairs 7(1):53-58*, 7:53–58, March 2019.

[91] Volodymyr Salata. Applications of nanoparticles in biology and medicine. *Journal of nanobiotechnology*, 2:3, 05 2004.

[92] Georg Hildenbrand, Philipp Metzler, Goetz Pilarczyk, Vladimir Bobu, Wilhelm Kriz, Hiltraud Hosser, Jens Fleckenstein, Matthias Krufczik, Felix Bestvater, Frederik Wenz, and Michael Hausmann. Dose enhancement effects of gold nanoparticles specifically targeting rna in breast cancer cells. *PLOS ONE*, 13:e0190183, 01 2018.

[93] Leonard E. Gerlowski and Rakesh K. Jain. Microvascular permeability of normal and neoplastic tissues. *Microvascular Research*, 31(3):288 – 305, 1986.

[94] Jun Fang, Hideaki Nakamura, and Hiroshi Maeda. The epr effect: Unique features of tumor blood vessels for drug delivery, factors involved, and limitations and augmentation of the effect. *Advanced Drug Delivery Reviews*, 63(3):136 – 151, 2011. EPR Effect Based Drug Design and Clinical Outlook for Enhanced Cancer Chemotherapy.

[95] Hiroshi Maeda, Kenji Tsukigawa, and Jun Fang. A retrospective 30 years after discovery of the enhanced permeability and retention effect of solid tumors: Next-generation chemotherapeutics and photodynamic therapy-problems, solutions, and prospects. *Microcirculation*, 23(3):173–182, 2016.

[96] F. Danhier. To exploit the tumor microenvironment: Since the epr effect fails in the clinic, what is the future of nanomedicine? *Journal of Controlled Release*, 244:108 – 121, 2016.

[97] Rakesh K. Jain and Triantafyllos Stylianopoulos. Delivering nanomedicine to solid tumors. *Nature Reviews Clinical Oncology*, 7:653, September 2010.

[98] Olga Kutova, Evgenii Guryev, Evgeniya Sokolova, Razan Alzeibak, and Irina Balalaeva. Targeted delivery to tumors: Multidirectional strategies to improve treatment efficiency. *Cancers*, 11:68, 01 2019.

[99] Nazanin Hoshyar, Samantha Gray, Hongbin Han, and Gang Bao. The effect of nanoparticle size on in vivo pharmacokinetics and cellular interaction. *Nanomedicine (London, England)*, 11(6):673–692, March 2016.

[100] Ganeshchandra Sonavane, Keishiro Tomoda, and Kimiko Makino. Biodistribution of colloidal gold nanoparticles after intravenous administration: Effect of particle size. *Colloids and Surfaces B: Biointerfaces*, 66(2):274 – 280, 2008.

[101] James Hainfeld, Sharif M. Ridwan, Yaroslav Stanishevskiy, Nathaniel Smilowitz, James Davis, and Henry Smilowitz. Small, long blood half-life iodine nanoparticle for vascular and tumor imaging. *Scientific Reports*, 8, 12 2018.

[102] S. Agostinelli, J. Allison, K. Amako, J. Apostolakis, H. Araujo, P. Arce, M. Asai, D. Axen, S. Banerjee, G. Barrand, F. Behner, L. Bellagamba, J. Boudreau, L. Broglia, A. Brunengo, H. Burkhardt, S. Chauvie, J. Chuma, R. Chytracek, G. Cooperman,

G. Cosmo, P. Degtyarenko, A. Dell'Acqua, G. Depaola, D. Dietrich, R. Enami, A. Feliciello, C. Ferguson, H. Fesefeldt, G. Folger, F. Foppiano, A. Forti, S. Garelli, S. Giani, R. Giannitrapani, D. Gibin, J.J. [GÃşmez Cadenas], I. GonzÃąlez, G. [Gracia Abril], G. Greeniaus, W. Greiner, V. Grichine, A. Grossheim, S. Guatelli, P. Gumplinger, R. Hamatsu, K. Hashimoto, H. Hasui, A. Heikkinen, A. Howard, V. Ivanchenko, A. Johnson, F.W. Jones, J. Kallenbach, N. Kanaya, M. Kawabata, Y. Kawabata, M. Kawaguti, S. Kelner, P. Kent, A. Kimura, T. Kodama, R. Kokoulin, M. Kossov, H. Kurashige, E. Lamanna, T. LampÃľn, V. Lara, V. Lefebure, F. Lei, M. Liendl, W. Lockman, F. Longo, S. Magni, M. Maire, E. Medernach, K. Minamimoto, P. [Mora de Freitas], Y. Morita, K. Murakami, M. Nagamatu, R. Nartallo, P. Nieminen, T. Nishimura, K. Ohtsubo, M. Okamura, S. O'Neale, Y. Oohata, K. Paech, J. Perl, A. Pfeiffer, M.G. Pia, F. Ranjard, A. Rybin, S. Sadilov, E. [Di Salvo], G. Santin, T. Sasaki, N. Savvas, Y. Sawada, S. Scherer, S. Sei, V. Sirotenko, D. Smith, N. Starkov, H. Stoecker, J. Sulkimo, M. Takahata, S. Tanaka, E. Tcherniaev, E. [Safai Tehrani], M. Tropeano, P. Truscott, H. Uno, L. Urban, P. Urban, M. Verderi, A. Walkden, W. Wander, H. Weber, J.P. Wellisch, T. Wenaus, D.C. Williams, D. Wright, T. Yamada, H. Yoshida, and D. Zschiesche. Geant4âĂŤa simulation toolkit. *Nuclear Instruments and Methods in Physics Research Section A: Accelerators, Spectrometers, Detectors and Associated Equipment*, 506(3):250 – 303, 2003.

[103] J. Allison, K. Amako, J. Apostolakis, H. Araujo, P. Arce Dubois, M. Asai, G. Barrand, R. Capra, S. Chauvie, R. Chytracek, G. A. P. Cirrone, G. Cooperman, G. Cosmo, G. Cuttone, G. G. Daquino, M. Donszelmann, M. Dressel, G. Folger, F. Foppiano, J. Generowicz, V. Grichine, S. Guatelli, P. Gumplinger, A. Heikkinen, I. Hrivnacova, A. Howard, S. Incerti, V. Ivanchenko, T. Johnson, F. Jones, T. Koi, R. Kokoulin, M. Kossov, H. Kurashige, V. Lara, S. Larsson, F. Lei, O. Link, F. Longo, M. Maire, A. Mantero, B. Mascialino, I. McLaren, P. Mendez Lorenzo, K. Minamimoto, K. Murakami, P. Nieminen, L. Pandola, S. Parlati, L. Peralta, J. Perl, A. Pfeiffer, M. G. Pia, A. Ribon, P. Rodrigues, G. Russo, S. Sadilov, G. Santin, T. Sasaki, D. Smith, N. Starkov, S. Tanaka, E. Tcherniaev, B. Tome, A. Trindade, P. Truscott, L. Urban, M. Verderi, A. Walkden, J. P. Wellisch, D. C. Williams, D. Wright, and H. Yoshida. Geant4 developments and applications. *IEEE Transactions on Nuclear Science*, 53(1):270–278, 2006.

[104] J. Allison, K. Amako, J. Apostolakis, P. Arce, M. Asai, T. Aso, E. Bagli, A. Bag-

ulya, S. Banerjee, G. Barrand, B.R. Beck, A.G. Bogdanov, D. Brandt, J.M.C. Brown, H. Burkhardt, Ph. Canal, D. Cano-Ott, S. Chauvie, K. Cho, G.A.P. Cirrone, G. Cooperman, M.A. CortÃĺs-Giraldo, G. Cosmo, G. Cuttone, G. Depaola, L. Desorgher, X. Dong, A. Dotti, V.D. Elvira, G. Folger, Z. Francis, A. Galoyan, L. Garnier, M. Gayer, K.L. Genser, V.M. Grichine, S. Guatelli, P. GuÃĺye, P. Gumplinger, A.S. Howard, I. HÅŹivnÃąÄIJovÃą, S. Hwang, S. Incerti, A. Ivanchenko, V.N. Ivanchenko, F.W. Jones, S.Y. Jun, P. Kaitaniemi, N. Karakatsanis, M. Karamitros, M. Kelsey, A. Kimura, T. Koi, H. Kurashige, A. Lechner, S.B. Lee, F. Longo, M. Maire, D. Mancusi, A. Mantero, E. Mendoza, B. Morgan, K. Murakami, T. Nikitina, L. Pandola, P. Paprocki, J. Perl, I. PetroviÄĞ, M.G. Pia, W. Pokorski, J.M. Quesada, M. Raine, M.A. Reis, A. Ribon, A. [RistiÄĞ Fira], F. Romano, G. Russo, G. Santin, T. Sasaki, D. Sawkey, J.I. Shin, I.I. Strakovsky, A. Taborda, S. Tanaka, B. TomÃľ, T. Toshito, H.N. Tran, P.R. Truscott, L. Urban, V. Uzhinsky, J.M. Verbeke, M. Verderi, B.L. Wendt, H. Wenzel, D.H. Wright, D.M. Wright, T. Yamashita, J. Yarba, and H. Yoshida. Recent developments in geant4. *Nuclear Instruments and Methods in Physics Research Section A: Accelerators, Spectrometers, Detectors and Associated Equipment*, 835:186 – 225, 2016.

[105] J.C. Maxwell. On physical lines of force. *Philosophical Magazine*, 90:11–23, 02 2010.

[106] A. Einstein. über einen die erzeugung und verwandlung des lichtes betreffenden heuristischen gesichtspunkt. *Annalen der Physik*, 322(6):132–148, 1905.

[107] John David Jackson. *Classical electrodynamics*. Wiley, New York, NY, 3rd ed. edition, 1999.

[108] Milton Orchin, Roger Macomber, Allan Pinhas, and R. Wilson. *Atomic Orbital Theory*, pages 1 – 24. 01 2005.

[109] C. F. V. Weizsäcker. Zur Theorie der Kernmassen. *Zeitschrift fur Physik*, 96(7-8):431–458, July 1935.

[110] K. Bethge, G. Walter, and B. Wiedemann. *Kernphysik: Eine Einfuhrung*. Springer-Lehrbuch. Springer, 2001.

[111] Eric Scerri. A review of research on the history and philosophy of the periodic table. *Journal of Science Education*, 12:4 – 7, 01 2011.

[112] W. Pauli. über den zusammenhang des abschlusses der elektronengruppen im atom mit der komplexstruktur der spektren. *Zeitschrift für Physik*, 31(1):765–783, 1925. cited By 317.

[113] A.C. Thompson. *X-ray Data Booklet*. Lawrence Berkeley National Laboratory, University of California, 2009.

[114] Tom Schoonjans, Antonio Brunetti, Bruno Golosio, Manuel Sanchez del Rio, Vicente Armando Solé, Claudio Ferrero, and Laszlo Vincze. The xraylib library for x-rayâĂŞmatter interactions. recent developments. *Spectrochimica Acta Part B: Atomic Spectroscopy*, 66(11):776 – 784, 2011.

[115] M.J. Berger, J.H. Hubbell, S.M. Seltzer, J. Chang, J.S. Coursey, R. Sukumar, D.S. Zucker, and K Olsen. Xcom: Photon cross section database (version 1.5). [Online] Available: http://physics.nist.gov/xcom [2019, July 30]. National Institute of Standards and Technology, Gaithersburg, MD.

[116] H. Hertz. Ueber einen einfluss des ultravioletten lichtes auf die electrische entladung. *Annalen der Physik*, 267(8):983–1000, 1887.

[117] Ilya Obodovskiy. Chapter 6 - interaction of gamma quanta with matter. In Ilya Obodovskiy, editor, *Radiation*, pages 137 – 150. Elsevier, 2019.

[118] J. A. BEARDEN and A. F. BURR. Reevaluation of x-ray atomic energy levels. *Rev. Mod. Phys.*, 39:125–142, Jan 1967.

[119] Manne Siegbahn. Relations between the k and l series of the high-frequency spectra. *Nature*, 96:676–676.

[120] H.G.J. Moseley M.A. Lxxx. the high-frequency spectra of the elements. part ii. *The London, Edinburgh, and Dublin Philosophical Magazine and Journal of Science*, 27(160):703–713, 1914.

[121] Michael F. L'Annunziata. 5 - atomic electron radiation. In Michael F. L'Annunziata, editor, *Radioactivity*, pages 341 – 346. Elsevier Science B.V., Amsterdam, 2007.

[122] Arthur H. Compton. A quantum theory of the scattering of x-rays by light elements. *Phys. Rev. 21, 483*, 1923.

[123] Andrew T. Young. Rayleigh scattering. *Appl. Opt.*, 20(4):533–535, Feb 1981.

[124] Oskar Klein and Yuichiro Nishina. Über die streuung von strahlung durch freie elektronen nach der neuen relativistischen quantendynamik von dirac. *Zeitschrift für Physik*, 52:853–868.

[125] K.A. Olive et al. Review of Particle Physics. *Chin. Phys. C*, 38:090001, 2014.

[126] D. V. Rao, T. Takeda, Y. Itai, T. Akatsuka, R. Cesareo, A. Brunetti, and G. E. Gigante. Doppler Broadening and its Contribution to Compton Energy-Absorption Cross Sections: An Analysis of the Compton Component in Terms of Mass-Energy Absorption Coefficient. *Journal of Physical and Chemical Reference Data*, 31(3):769–818, September 2002.

[127] Giorgio Matt, Marco Feroci, Massimo Rapisarda, and Enrico Costa. Treatment of compton scattering of linearly polarized photons in monte carlo codes. *Radiation Physics and Chemistry*, 48(4):403 – 411, 1996.

[128] Beer. Bestimmung der Absorption des rothen Lichts in farbigen Flssigkeiten, January 1852.

[129] W. Fang, L. Li, and S. Zhang. Fan-beam x-ray fluorescence computed tomography (xfct) with gold nanoparticles. In *2017 IEEE Nuclear Science Symposium and Medical Imaging Conference (NSS/MIC)*, pages 1–4, 2017.

[130] Bernard Jones, Nivedh Manohar, Francisco Reynoso, Andrew Karellas, and Sang Cho. Experimental demonstration of benchtop x-ray fluorescence computed tomography (xfct) of gold nanoparticle-loaded objects using lead- and tin-filtered polychromatic cone-beams. *Physics in medicine and biology*, 57:N457–N467, 11 2012.

[131] James Seibert. X-ray imaging physics for nuclear medicine technologists. part 1: Basic principles of x-ray production. *Journal of nuclear medicine technology*, 32:139–47, 10 2004.

[132] Utz Kramar. X-ray fluorescence spectrometers. In John C. Lindon, editor, *Encyclopedia of Spectroscopy and Spectrometry*, pages 2467 – 2477. Elsevier, Oxford, 1999.

[133] Jakob Larsson, Carmen Vogt, William TwengstrÃűm, Muhammet Toprak, Johanna Dzieran, Marie Henriksson, and Hans Hertz. High-spatial-resolution x-ray fluorescence tomography with spectrally matched nanoparticles. *Physics in Medicine and Biology*, 63, 07 2018.

[134] excillum. `https://www.excillum.com/products/metaljet/metaljet-d2-70-kv/`, viewed 20 Mar 2020.

[135] F. R. Elder, A. M. Gurewitsch, R. V. Langmuir, and H. C. Pollock. Radiation from electrons in a synchrotron. *Phys. Rev.*, 71:829–830, Jun 1947.

[136] Gavin Fox. Generation x-ray - a coming of age. *Arbor*, 191, 08 2015.

[137] Herman Winick, George Brown, Klaus Halbach, and John Harris. Wiggler and undulator magnets. *Physics Today - PHYS TODAY*, 34:50–63, 01 1981.

[138] G. Brown, K. Halbach, J. Harris, and H. Winick. Wiggler and undulator magnets - a review. *Nuclear Instruments and Methods in Physics Research*, 208(1):65 – 77, 1983.

[139] Malcolm R. Howells and B. M. Kincaid. The properties of undulator radiation. 1994.

[140] K Balewski, W Brefeld, W Decking, H Franz, Ralf Röhlsberger, and E Weckert. Petra iii: A low emittance synchrotron radiation source. 01 2004.

[141] A. Schöps, Pavel Vagin, and M. Tischer. Properties of the insertion devices for petra iii and its extension. volume 1741, page 020019, 07 2016.

[142] Norbert Schell, Andrew King, Felix Beckmann, Torben Fischer, Martin Müller, and Andreas Schreyer. The high energy materials science beamline (hems) at petra iii. In *Mechanical Stress Evaluation by Neutrons and Synchrotron Radiation VI*, volume 772 of *Materials Science Forum*, pages 57–61. Trans Tech Publications Ltd, 2 2014.

[143] David Pennicard, Benoît Pirard, Oleg Tolbanov, and Krzysztof Iniewski. Semiconductor materials for x-ray detectors. *MRS Bulletin*, 42(6):445âĂŞ450, 2017.

[144] Stefano Sordo, Leonardo Abbene, Ezio Caroli, A.M. Mancini, Andrea Zappettini, and Pietro Ubertini. Progress in the development of cdte and cdznte semiconductor radiation detectors for astrophysical and medical applications. *Sensors (Basel, Switzerland)*, 9:3491–526, 05 2009.

[145] Robert Redus, John Pantazis, Thanos Pantazis, Alan Huber, and Brian Cross. Characterization of cdte detectors for quantitative x-ray spectroscopy. *Nuclear Science, IEEE Transactions on*, 56:2524 – 2532, 09 2009.

[146] L. Abbene and S. Del Sordo. 8.18 - cdte detectors. In Anders Brahme, editor, *Comprehensive Biomedical Physics*, pages 285 – 314. Elsevier, Oxford, 2014.

[147] W. van Roosbroeck. Theory of the yield and fano factor of electron-hole pairs generated in semiconductors by high-energy particles. *Phys. Rev.*, 139:A1702–A1716, Aug 1965.

[148] F. Perotti and C. Fiorini. Observed energy dependence of fano factor in silicon at hard x-ray energies. *Nuclear Instruments and Methods in Physics Research Section A: Accelerators, Spectrometers, Detectors and Associated Equipment*, 423(2):356 – 363, 1999.

[149] A. Niemelä. Low-noise electronics for high-resolution cdznte and cdte x-ray detection systems. 1996.

[150] F. Scholze and M. Procop. Modelling the response function of energy dispersive x-ray spectrometers with silicon detectors. *X-Ray Spectrometry*, 38(4):312–321, 2009.

[151] T. Papp. On the response function of solid-state detectors, based on energetic electron transport processes. *X-Ray Spectrometry*, 32:458–469, nov 2003.

[152] Karl Hecht. Zum Mechanismus des lichtelektrischen Primärstromes in isolierenden Kristallen. *Zeitschrift fur Physik*, 77(3-4):235–245, March 1932.

[153] AMPTEK. `https://www.amptek.com/products/cdte-x-ray-and-gamma-ray-detectors/xr-100cdte-x-ray-and-gamma-ray-detector`, viewed 02 Aug 2019.

[154] Albert Rose. *Vision Human and Electronic*. Springer (17. Januar 2013), 1973.

[155] Arthur E. Burgess. The rose model, revisited. *J. Opt. Soc. Am. A*, 16(3):633–646, Mar 1999.

[156] Alke Meents, Bernd Reime, Nicolas Stuebe, Pontus Fischer, Martin Warmer, Dennis Goeries, Jan Roever, Jan Meyer, Janine Fischer, Anja Burkhardt, Ismo Vartiainen, Petri Karvinen, and Christian David. Development of an in-vacuum x-ray microscope with cryogenic sample cooling for beamline P11 at PETRA III. In Barry Lai, editor, *X-Ray Nanoimaging: Instruments and Methods*, volume 8851, pages 77 – 83. International Society for Optics and Photonics, SPIE, 2013.

[157] Anja Burkhardt, Tim Pakendorf, Bernd Reime, Jan Meyer, Pontus Fischer, Nicolas Stübe, Saravanan Panneerselvam, Olga Lorbeer, Karolina Stachnik, Martin Warmer,

Philip Rödig, Dennis Göries, and Alke Meents. Status of the crystallography beamlines at PETRA III. *The European physical journal / Plus*, 131(3):56, 2016. (c) Societa Italiana di Fisica / Springer-Verlag.

[158] HITACHI. `https://www.hitachi-hightech.com/hhs-us/product_detail/?pn=ana-vortex-em`, viewed 20 March 2020.

[159] H Reichert, V Honkimäki, A Snigirev, S Engemann, and H Dosch. A new x-ray transmission-reflection scheme for the study of deeply buried interfaces using high-energy microbeams. *Physica B: Condensed Matter*, 336(1):46 – 55, 2003. Proceedings of the Seventh International Conference on Surface X-ray and Neutron Scattering.

[160] Ulrich Lienert. Conceptual design report of the swedish materials science beamline at petra iii. Technical report, DESY, 2012.

[161] Willem Rischau. Characterization of the x-ray eye. Technical report, Friedrich Schiller University Jena, Germany, 2009.

[162] Robin Owen, James Holton, Clemens Schulze-Briese, and Elspeth Garman. Determination of x-ray flux using silicon pin diodes. *Journal of synchrotron radiation*, 16:143–51, 04 2009.

[163] Florian Schulz, Johannes Möller, Felix Lehmkühler, Andrew Smith, Tobias Vossmeyer, Holger Lange, Gerhard Grübel, and Martin Schroer. Structure and stability of peg- and mixed peg-layer-coated nanoparticles at high particle concentrations studied in situ by small-angle x-ray scattering. *Particle & Particle Systems Characterization*, 35:1700319, 12 2017.

[164] Eline Ruigrok, Wytske Weerden, Julie Nonnekens, and Marion de Jong. The future of psma-targeted radionuclide therapy: An overview of recent preclinical research. *Pharmaceutics*, 11:560, 10 2019.

[165] Louise Emmett, Kathy Willowson, John A Violet, Jane Shin, Ashley Blanksby, and Jonathan Lee. Lutetium 177 psma radionuclide therapy for men with prostate cancer: a review of the current literature and discussion of practical aspects of therapy. *Journal of Medical Radiation Sciences*, 64:52 – 60, 2017.

[166] Hyun Goo and Jin Mo Goo. Dual-energy ct: New horizon in medical imaging. *Korean Journal of Radiology*, 18:555, 07 2017.

[167] Juergen Fornaro, Sebastian Leschka, Dennis Hibbeln, Philip Butler, Nigel Anderson, Gregor Pache, Hans Scheffel, Simon Wildermuth, Hatem Alkadhi, and Paul Stolzmann. Dual- and multi-energy ct: approach to functional imaging. *Insights into imaging*, 2:149–159, 04 2011.

[168] Liqiang Ren, Cynthia H. McCollough, and Lifeng Yu. Multi-energy CT with triple x-ray beams and photon-counting-detector CT for simultaneous imaging of two contrast agents: an experimental comparison. In Taly Gilat Schmidt, Guang-Hong Chen, and Hilde Bosmans, editors, *Medical Imaging 2019: Physics of Medical Imaging*, volume 10948, pages 318 – 323. International Society for Optics and Photonics, SPIE, 2019.

[169] Md Ahmed, Selcuk Yasar, and Sang Cho. Development of an attenuation correction method for direct x-ray fluorescence (xrf) imaging utilizing gold l-shell xrf photons. *Medical Physics*, 45, 10 2018.

[170] Timothy Johnstone, Ga Park, and Stephen Lippard. Understanding and improving platinum anticancer drugs - phenanthriplatin. *Anticancer research*, 34:471–476, 01 2014.

[171] I. Lyapun, B. Andrukov, and M. Bynina. Hela cell culture: Immortal heritage of henrietta lacks. *Molecular Genetics, Microbiology and Virology*, 34:195–200, 10 2019.

[172] Bang Guo, Zhen Yang, and Long Zhang. Gadolinium deposition in brain: Current scientific evidence and future perspectives. *Frontiers in Molecular Neuroscience*, 11, 09 2018.

[173] Bayer Vital. `https://www.patienteninfo-service.de/a-z-liste/g/gadovistR-10-mmolml-injektionsloesung/`, viewed 20 May 2020.

[174] Kim L. Beaucage, Steven I. Pollmann, Stephen M. Sims, S. Jeffrey Dixon, and David W. Holdsworth. Quantitative in vivo micro-computed tomography for assessment of age-dependent changes in murine whole-body composition. *Bone Reports*, 5:70 – 80, 2016.

List of Figures

10 Acknowledgments

First I would like to thank my PhD supervisor Prof. Dr. Grüner who always holds teamwork in high regard, supervised me and everyone else in our group closely and impressively pushed projects successfully into existence against doubts and resistance. And I would like to thank my reviewer Prof. Dr. Wolfgang Hillert for evaluation this thesis.
Then I would like to thank PIER for funding me and this work and for the interesting workshops and meetings organized by the PIER graduate school.
I deeply want to thank everyone whom I worked with and who made work fun and enjoyable. Be it during long night shifts at PETRA III beamlines with fast food or in the short, sometimes less short, coffee breaks with inspiring discussions. The cooperative atmosphere in the team needs to be highlighted. I want to thank Florian Blumendorf, with whom the first steps of the XFI project were done, for his critical thinking and relaxed coffee and ice cream breaks, and for an interesting stay at the ELBE accelerator in Dresden.
I want to thank Christan Gabriel Koernig without whom the automation of experiments would have taken much more time. Especially the ability to debug code at 3 am with sleep deprivation and time pressure would surely have made him an excellent engineer at ESA. I am glad he did not take that road to work with satellites and orbital mechanics.
And I want to thank Theresa Staufer who reminded me to clean my coffee mugs and always was ready to lend a helping hand despite a though time schedule.
Finally I want to thank my dad for efficient support during the final phase of this work.

Eidesstattliche Versicherung / Declaration on oath

Hiermit versichere ich an Eides statt, die vorliegende Dissertationsschrift selbst verfasst und keine anderen als die angegebenen Hilfsmittel und Quellen benutzt zu haben.

Die eingereichte schriftliche Fassung entspricht der auf dem elektronischen Speichermedium.

Die Dissertation wurde in der vorgelegten oder einer ähnlichen Form nicht schon einmal ineinem früheren Promotionsverfahren angenommen oder als ungenügend beurteilt.

Hamburg, den 22.09.2020 _____

Unterschrift des Doktoranden